# Testing and Inverse Modelling for Solder Joint Reliability Assessment

by

**Elisha Tingha Kamara**

Centre for Numerical Modelling and Process Analysis

School of Computing and Mathematical Sciences, University of Greenwich
London, UK

A thesis submitted in partial fulfilment of the requirements of the University of Greenwich for the Degree of Doctor of Philosophy

February 2013

# Declaration

I certify that this work has not been accepted in substance for any degree, and is not concurrently being submitted for any degree other than that of Doctor of Philosophy (Ph.D) being studied at the University of Greenwich. I also declare that this work is the result of my own investigations except where otherwise identified by references and that I have not plagiarised the work of others.

…………………………………………………………………….

Elisha Tingha Kamara

…………………………………………………………………….

Dr. Hua Lu

(Supervisor)

……………………………………………………………………..

Prof.  Chris Bailey

(Second Supervisor)

# Acknowledgement

There are a number of individuals without whose invaluable support this work would not have been completed. I would like to express my profound gratitude to my supervisors, Dr. Hua Lu and Prof. Chris Bailey, who provided all the necessary support, knowledge, guidance, motivation and always been available for discussion

I will also like to express my thanks to the staff at NPL especially Dr. Chris Hunt, Dr. Owen Thomas and Dr. Davide Di Maio for their invaluable assistance and support for the experimental work.

I will also acknowledge the financial support of the University of Greenwich, IeMRC DTA and NPL for funding this research.

Finally I wish to acknowledge the support and affection from my family that were patient during at time trying times during this work.

# Abstract

As the trends in green manufacturing, miniaturization, and enhanced functionality of electronics devices continue without any sign of slowing down, the reliability of lead free solder joints with diminishing size has become more and more a challenge to the design engineers and the electronics manufacturing industry. In order to predict the reliability of solder joints accurately, it is necessary to develop test techniques to test solder joints efficiently under conditions that are comparable to those in application environment. In this day and age when computer simulation has become an indispensable tool in many areas, it is also very important that suitable material models are available for solder materials so that virtual design tools can be used to predict device reliability performance accurately.

In this work, the aim was to develop vibration and cyclic shear test methods and equipment, and to use computer modelling techniques in the analysis of lead free solder joints in microelectronics devices, and to develop an inverse Finite Element technique and experimental data to obtain constitutive laws for lead-free solder alloys. In the development of the vibration test machine, a prototype test machine that uses piezoelectric cell as actuators for the loading was modelled using the Finite Element Analysis method, and the behaviours of the test specimen which is similar to a BGA solder joint in dimensions was analysed. The static and dynamic response of the equipment was modelled and compared with experimental results. A novel multi-joint test specimen in which the solder deformation is similar to that in solder joints of BGAs that are under thermal loading was analysed so that test results can be interpreted and the specimens and loading conditions can be improved. The response of the joints reinforced the understanding that the interface of the solder and the copper or printed circuit board is the mostly likely region for crack growth and hence failure of the package. In the inverse Finite Element Analysis of solder joints, cyclic shear test data and Finite Element Analysis methods were used to improve the Anand's visco-plastic constitutive law for the SAC solder specimens under the test conditions. To reduce the possibility of spurious experimental data skewing the entire analysis, a technique was employed that uses limited experimental datasets in determining the material parameters. Simulation results using the new constitutive law showed significant improvement in accuracy.

The main contribution of this research work to the manufacturing, testing and virtual design of solder joints can be summarised as follows: (1) A unique dedicated high cycle fatigue test equipment that is especially suited for testing very small solder joints and other surface mounted technologies under vibration conditions has been successfully designed, and manufactured. This is expected to enhance the capability of the industry in solder joint tests. (2) The behaviours of individual solder joints in a BGA-like multi-joint test specimen under isothermal cyclic loading condition have been characterised making the prediction of solder properties more accurate and efficient. (3) A novel procedure that is based on inverse Finite Element Analysis to obtain nonlinear creep parameters of, for example, Anand's model, has been proposed and demonstrated. This method reduces the effect of spurious dataset, the high reliance of the skill of the individuals who perform the analysis and makes it possible for small institutions with limited resources to obtain the necessary model parameters for virtual product design and reliability analysis.

# Table of Content

# Table of Figures

# Glossary

| | |
|---|---|
| BGA | Ball grid array |
| CBGA | Ceramic Ball Grid Array |
| CCGA | Ceramic Column Grid Array Attachments |
| COB | Chip On-Board |
| CSED | Constant Strain Energy Density |
| CSP | Chip Scale Package |
| CTE | Coefficient Of Thermal Expansion |
| DBGA | Dimple Ball Grid Array |
| DIPs | Dual-in-line Packages |
| DOE | Design Of Experiment |
| DOF | Degree of Freedom |
| DTB | Dynamic Test Board |
| ENIG | Electroless Nickel Immersion Gold |
| EPA | Environmental Protection Agency |
| FCBGA | Flip Chip Ball Array Package |
| FCOB | Flip-Chip-On-Board |
| FEA | Finite Element Analysis |
| FEM | Finite Element Method |
| HALT | Highly Accelerated Life Test |
| IC | Integrated circuit |
| IMC | Intermetallic compound |
| IPC/JEDEC | Institute for Printed Circuits/Joint Electronic Device Engineering Council |
| IPTM | Interconnect Properties Testing Machine |
| ITRS | International Technology Roadmap for Semiconductors |
| LCC | Lead Chip Carrier |
| LCP | Liquid Crystal Polymer |
| LSI | Large Scale Integration |
| LVDT | Linear Variable Displacement Transformer |
| MBGA | Metal Ball Grid Array |
| MCM | Multi-Chip Modules |
| MCP | Multi-Chip Packaging |
| MSI | Medium Scale Integration |
| NPL | National Physical Laboratory |
| ODE | Ordinary Differential Equation |
| OSP | Organic Solder Preservative |
| Pb | Lead |
| PBGA | Plastic Ball Grid Array |
| PCB | Printed Circuit Board |
| PDE | Partial Differential Equation |
| PEN | Polyethylene Naphthalate |
| PGA | Pin-Grid_Array |
| PLCC | Plastic Lead Chip Carrier |
| PTH | Pin-Through-Hole |

| | |
|---|---|
| PWB | Printed Wiring Board |
| PZT | Piezoelectric Transducer |
| QFN | Quad Flat Pack No-Lead |
| QFP | Quad Flat Package |
| SAC305 | 96.5Sn-3.0Ag-0.5Cu |
| SAC405 | 95.5Sn-4.0Ag-0.5Cu |
| SH-DIP | Shrink DIP |
| SIP | Single In-Line Package |
| SiP | System-in Package |
| SJR | Solder Joint Reliability |
| SK-DIP | Skinny DIP |
| SnPb | Tin-lead |
| SO | Small Outline |
| SoP | System-on–Package |
| SSI | Small scale Integration |
| TAB | Tape-Automated Bonding |
| TBGA | Tape-Automated Ball Grid Array |
| Tm | Melting Point Temperature |
| ULSI | Ultra-Large Scale Integration |
| UTS | Ultimate tensile strength |
| VSLI | Very Large Scale Integration |
| WLP | Wafer-Level Packaging |
| ZIP | Zig-Zag In-Line Package |

# Chapter 1 Introduction

Electronics devices reside in almost all modern equipment and machinery and their reliability has always been a major issue for design and manufacturing engineers. The use of new materials, new manufacturing processes, and new trends in consumer products, new performance requirements, and new applications are all great challenges for the engineers and researchers in their pursuit for the best and most reliable design in electronics devices. One of the greatest challenges is to achieve high reliability for the manufacturing of interconnects, which are often the most vulnerable parts of electronics devices. In most applications, and in particular in applications that are used in harsh environments interconnects are often highly stressed because of the extreme temperature, pressure, acceleration, vibration etc. and may fail earlier than expected. Traditionally, one of the interconnect technologies of choice is soldering. The behaviour and response of solder to loading conditions has a direct impact on the reliability of interconnects and therefore electronics devices.

Electronic packages need interconnect materials to provide electrical connection and mechanical support for the components. Soldering technology has been used extensively in the electronics packaging industry for decades and the lead based alloys have been used for this purpose most of the time. The most popular solder alloy was the eutectic tin-lead (SnPb) due partly to its outstanding thermal, electrical and mechanical properties and partly due to the large body of accumulated work dealing with different loading and process conditions. Due to this large body of work, researchers can predict relatively accurately the behaviour of SnPb solders in most application environments. Unfortunately a major constituent in SnPb solder, lead, is a heavy metal that carries significant health risk for humans especially to children and pregnant women and has devastating long term effect on the environment. Lead poses its greatest risk not during the production of the appliance but in its disposal where the lead will leach from landfills and contaminate groundwater supply. The amount of solder contained in electronics components is not as large as in some other manufactured components, say in batteries and it is therefore neither easy nor cost effective to recycle. The introduction of RoHS [1] and WEEE [2] directives by the European Union has effectively banned lead and other hazardous substances from use and made the producers of electronics and electrical components responsible for their safe disposal and has driven the research into finding worthy lead-free replacement compounds. The interconnect materials that do not contain the hazardous lead are generally referred to as lead-free materials.

The definition of lead-free material though, doesn’t mean a material that is totally devoid of lead. The amount of lead defined as lead-free is dependent on the standard or directive used in the definition. The RoHS directive defines lead-free as a material containing less than 0.1 wt. % of lead. The ASTM B32-96 has two definition for lead-free; less than 0.1% generally and 0.2% for special cases. Whilst ISO 9453 defines lead-free as 0.05 – 0.1% lead [3].

The main lead-free alternative used in the industry is the ternary combination of tin, silver and copper (SAC). The switch from lead to lead free solder necessitates a change in materials, engineering processes, process techniques and soldering techniques. The new material combinations have different material properties and long term reliability is of serious concern. Unfortunately, the replacement combinations that are being touted do not have the same body of work that researchers and analysts can access when compared to SnPb. The limited availability of data for lead free solder is not the only problem. The available data are often not fit for purpose. For example, most of the material data available for lead-free solder alloys are the bulk material data whose response is different from solder joints that are used in microelectronics manufacturing. This lack of material and reliability data for lead-free solder is a major concern for many manufacturers of electronic equipment. It is this need to gather test data and determine material properties for lead-free solder in order to accurately predict the behaviour of the lead-free replacement that has motivated the research work in this project.

## 1.1 Electronics Packaging Overview

Electronic packaging is a manufacturing process which enables electronics products to perform their intended functions in a reliable manner. It is a combination of engineering and manufacturing technologies that are required to convert electronic circuits into a manufactured assembly. The engineering technologies may involve electrical, mechanical, thermal, and chemical processes, as well as materials, component and other. Electronics packaging also forms the portion of an electronics structure that protects and shields the electronics/electrical element and its environment from each other [4-6]. As summarised in Figure. 1-1, there are four main functions of electronics packages: signal distribution, protection, heat dissipation and power distribution. For the chip to perform the task for which it was designed it needs to be powered by an external source and supplied with time varying signal. Packaging is therefore considered as the bridge that interconnects the ICs and other components into a system-level board to form electronic products. As electronics devices have become ever more complicated with an increasing number of transistors on semiconductor chips, the packaging of these chips to provide suitable and effective environment for the electronics package is becoming more and more challenging.

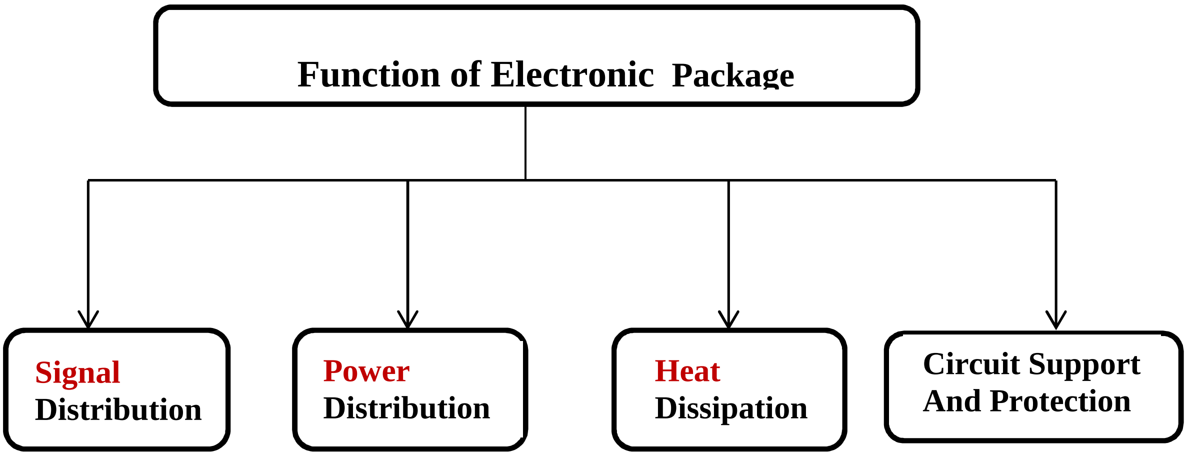

Figure 1-1 Basic Electronic Packaging function

## 1.2 Electronics Packaging and Interconnects

Depending on the functionality and manufacturing process, electronic packaging technologies can be classified into different levels and at each level there are specific connection devices associated with that level (Figure 1-2). The levels are divided as follows:

- Level 0: Gate-to-gate interconnections on a monolithic silicon chip
- Level 1: Single-chip package, MCM, chips. Packaging of silicon chips into dual-in-line packages (DIPs), small outline (SO) ICs, chip carriers, multichip packages, ball grid array (BGA) and the chip level interconnects that join the chip to the lead frames. Instead

of lead frames, tape-automated bonding (TAB) or chip on-board (COB) technologies can be utilized.

- Level 2: Printed wiring board (PWB) or Printed Circuit Board (PCB). Printed conductor paths connect the leads of components to PCBs and to the electrical edge connectors for off-the-board interconnection
- Level 3: Backplane (Equipment Drawer) connections between PCBs. PCB-to-PCB interconnections or card-to-motherboard interconnections
- Level 4: Equipment rack connections between two subassemblies. A rack or frame hold several shelves of subassemblies that must be connected together to make up a complete system.
- Level 5: Connections between physically separate systems such as host computer to terminals, computer to printer, and so on. [7]

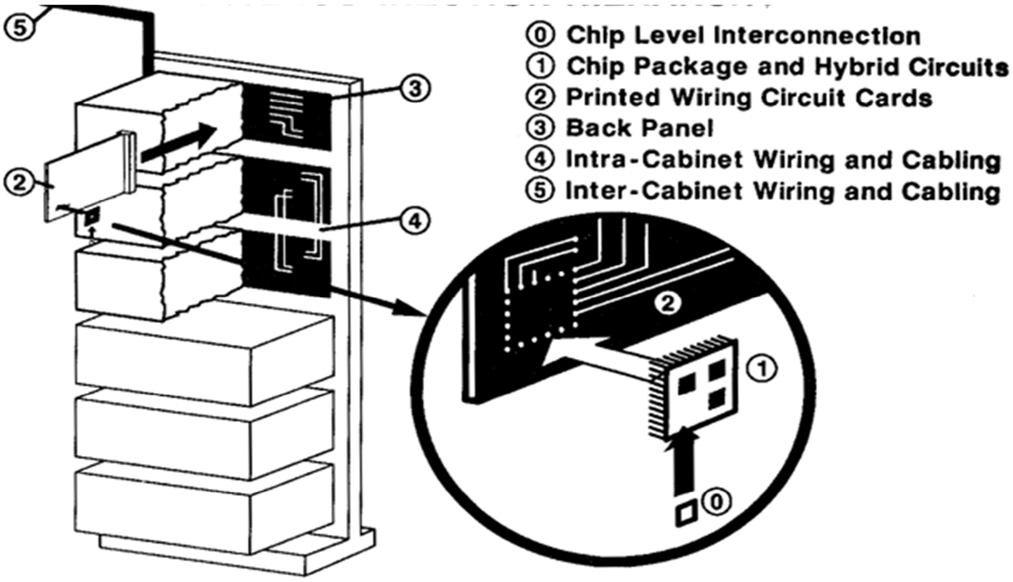

Figure 1-2 Packing Hierarchy [7]

This work focuses on modelling and analysing solder interconnect using solder balls that are used in the second level packaging but the results may also be useful for other second level solder interconnect and flip-chip which is a first level interconnect technology because the solder’s response to vibration loading will be true for both levels. In the following more details about these two levels of interconnect are described [8, 9].

### 1.2.1 First Level Interconnection

In the first level packaging, the chip communicates electrically with the substrate using I/O connections using either wire bonding or flip chip bonding technologies.

Wire bonding is a primary method of making interconnections between IC and printed circuit board during semiconductor fabrication. It is generally considered a cost effective and flexible interconnection technology, and is used to assemble the vast majority of semiconductor packages. Generally fine metal wire of copper, aluminium or gold with diameter of 20-25 μm is used to bond each chip to the substrate pad. The wire is welded to the pads at each end by thermosonic or ultrasonic bonding. Figure1-3 shows schematics of wire bonding interconnections. The use of wire bonding interconnection technology has a number of drawbacks and of particular concern is that the bonding process is time-consuming, since individual connection between chip and board are made sequentially. For chips containing many I/Os, the process time for each chip can become unacceptably long. Another concern is the degradation of performance at high frequencies due to parasitic effects. The main parasitic effect is the bond wire inductance, which increases in proportion to the interconnect length [10]. Flip-chip is an interconnect technology [11]. It solves some of the issues in wire bonding [12]. In this interconnect method, tiny solder balls are used to connect chips to the substrate. This method can achieve low profile, high IO counts, and low parasitic effect.

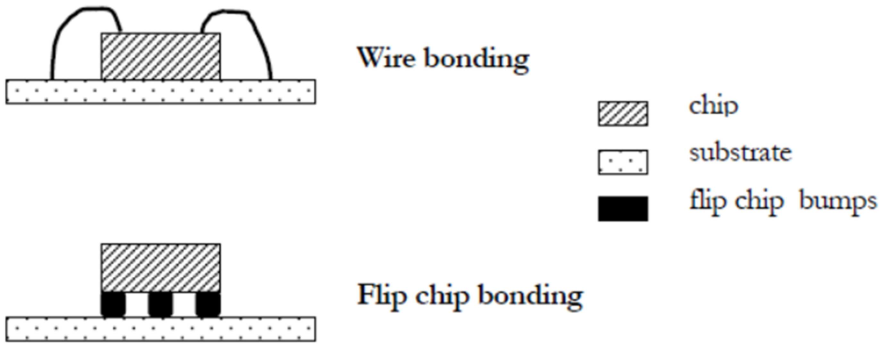

Figure 1-3 I/O connection structure [10]

### 1.2.2 Second-level (package-to-board) interconnections

In second-level packaging, IC packages and other components are mounted on a circuit board. The terminals of each first-level package, i.e. pins, leads or solder balls, are electrically connected with the metal tracks on the circuit board. These connections are generally performed by one of three basic technologies, all based on soldering: pin-through-hole connection, surface mounting or ball-grid-array (BGA) attachment [11]. All of the single IC packages and MCMs are classified into one of these categories.

#### *1.2.2.1 Pin-through-hole (PTH) connection*

This is the oldest connection approach, for components with pin terminals e.g. IC packages using DIP (dual in-line package) or PGA (pin-grid-array) forms. The mounting technology uses precision holes, drilled through the circuit board, with pads top and bottom to which the pins may be soldered. To make connection to internal wiring layers within the board, the walls of the through-holes may be plated by copper.

#### *1.2.2.2 Surface mounting*

This technology was developed in the mid-1980s for mounting packages with peripheral leads, such as QFP (quad flat package). In this technology, a chip carrier is soldered to the pads on the surface of a board without requiring any through holes. This assembly technology paved the way for BGA (ball grid array) area-array connections in the late 1990s.

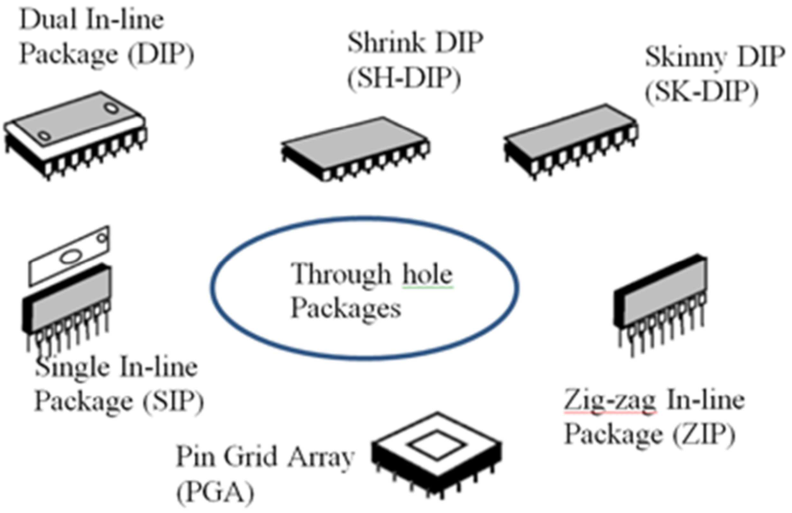

Figure 1-4 Examples of Through Hole Packages

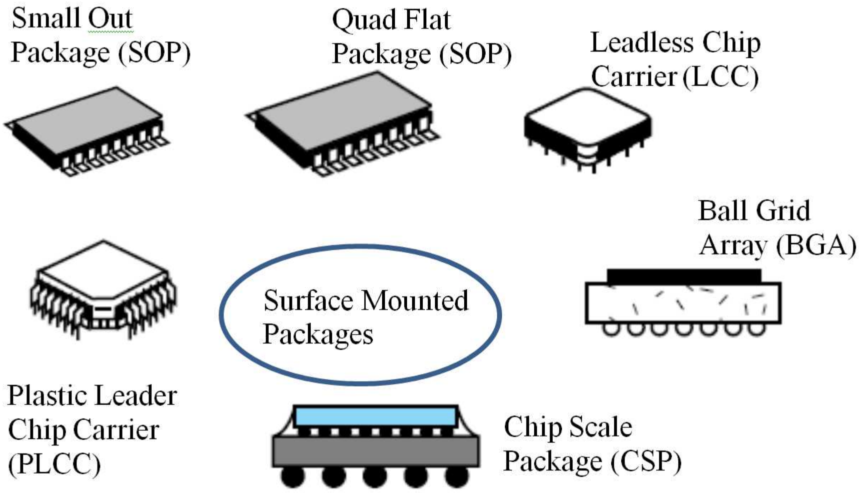

Figure 1-5 Examples of Surface mounted package

### *1.2.2.3 Ball grid array (BGA)*

BGA is a low cost, leadless package that can be soldered directly to the substrate. This is the fastest growing method in recent years. It accounts for the main connection method for current high performance IC components, from PBGAs to state-of-the-art CSPs (chip scale packages). This type of package ensures high number of I/Os and offers maximum space efficiency in the board with excellent thermal and electrical performance. The main disadvantage is that it is difficult to inspect the solder joints as they are kept hidden [12]. Depending on the substrate type, BGA packages can be classified as Plastic BGA (PBGA), Ceramic BGA (CGBA), Tape-automated bonding Ball Grid Array (TBGA), Metal Ball Grid Array (MBGA), Dimple Ball Grid Array (DBGA), etc. [13]

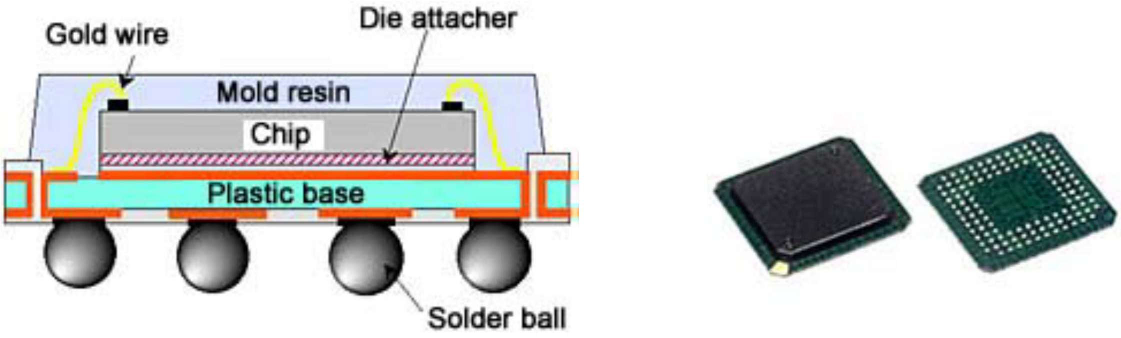

Figure 1-6 Plastic Ball Grid Array (PBGA)

### 1.2.3 Chip-on-board Interconnection

With the ever-growing demands on low cost and small size packaging, the distinctions between conventional packaging levels are blurring. Direct chip-on-board (COB), which has been mainly used in advanced IC packages such as MCMs, is nowadays finding widespread use in system-level packaging. Wire bonding and flip-chip bonding have both been used as interconnection methods for chip-on-board assembly. However, the trend is towards flip-chip-on-board (FCOB) due to its advantages of small footprint and enhanced electrical performance.

Low-cost FCOB generally uses organic FR-4 circuit boards. A disadvantage of this board material is the large coefficient of thermal expansion (CTE) mismatch relative to silicon-based IC chips. If the assembly is subject to high temperatures at subsequent process steps, or undergoes temperature cycling in use as the device is powered on and off, stresses are created in the interfaces of the bump joints due to the CTE mismatch. These stresses, if sufficiently large, can lead to mechanical failure of one or more of the interconnects. This effect has been cited as the most common cause of failure in solder flip chip assemblies.

To alleviate the problem of CTE mismatch in FCOB, underfill encapsulant that has a CTE close to the flip chip joint is generally filled into the gap between chip and organic circuit board. The underfill is dispensed along one or more edges of the chip; it flows under the chip via capillary action (Figure. 1-7). Upon curing, the hard underfill serves to compensate for the thermal expansion difference between the chip and the board and mechanically bonds the chip and board together. As such, underfill significantly enhances the fatigue life (reliability) of FCOB packages [13].

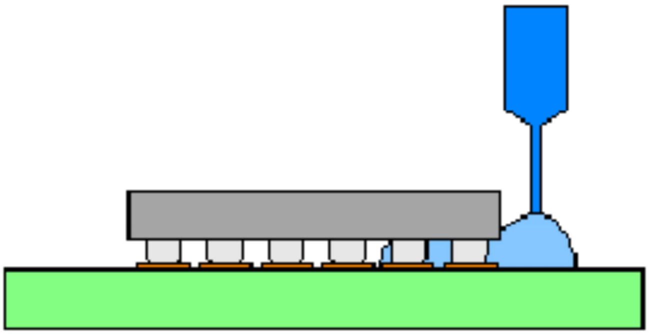

Figure 1-7 Dispensing the underfill encapsulant for flip chip assembly [13].

## 1.3 Trends in Electronics Manufacturing

Traditional electronic packaging presents significant problems. The IC packaging which provides I/O connections from the chip to the rest of the system was typically bulky and costly, limiting both the performance and the reliability of the IC. In addition, system packaging that provides the interconnection of components on a circuit board is similarly bulky and costly and limits the electrical and mechanical performance. To address these concerns, a number of technologies have been implemented whilst others are still in their infancy. Following is a discussion of some of these trends.

- *wafer-level packaging* (WLP) that involves creating the package while chips are still in wafer form and then separating them by dicing, is gaining popularity. Wafer-level packaging of stacked wafers has the stacked chips interconnected by vias formed through the material used to physically separate the wafers. Thus, system packaging at the wafer level is possible and will permit the mixing of different technologies in a single package.
- *multi-chip packaging* (MCP), integrates an electronic system by interconnecting a number of ICs in a single packaging structure. MCP technology is done either by multi-chip modules (MCMs) in the planar fashion or by 3D stacked-chip packaging referred to as system-in-package (SiP) which incorporates ICs stacked vertically. Chip stacking can be accomplished by either stacking single-chip packages or by stacking a number of chips in a single package, or a combination of these approaches.
- *system-on-package* (SoP) addresses the shortcomings of both SoC and SiP in two ways. SoP uses CMOS-based transistor integration and RF, optical and digital integration by means of IC-package-system co-design. System-on-package (SoP) helps to overcome both the computing limitations and integration limitations of SoC, SiP, MCM and traditional system packaging. SoP includes both active and passive components including embedded digital, RF and optical components and functions in a microminiaturized package or board.
- The ITRS in its report in 2005 were indicating that the way forward for electronics packaging is through *System on Chip* (SoC) and *System in* Package (SiP) technologies

that provide a path for continued improvement in performance, power, cost and size at the system level [10]. A SiP is a number of integrated circuits enclosed in a single module (package) whilst a system on chip (SoC) is an integrated circuit (IC) that integrates all components of a computer or other electronic system into a single chip.

- The broadest adoption of SiP to date has been for stacked memory/logic devices and small modules (used to integrate mixed signal devices and passives) for mobile phone applications.

## 1.4 Challenges and Motivation

The ever growing demands for high density packaging in electronics have been driving the industry's push for more and more miniaturization and concerns for the environment and changes in government regulations that regulate electronics equipment production have made the use of new lead-free solder alloys impossible to avoid for most products. These factors have forced changes in manufacturing technologies and materials use, and caused serious reliability concerns for solder interconnect in electronics packaging. In order to address the concerns for product reliability, there are three important issues that must be addressed. 1) Efficient test equipment for the collection of reliable material property data, 2) understanding test specimen behaviours so that test results can be explained correctly and used in applications, and 3) efficiently extracting data for computer simulation.

To generate reliable experimental data for solder joints, it is important to note that the behaviour of bulk solder is different from that of solder balls in situ used in electronics packaging, and for different application environment different tests have to be carried out to obtain data that can be used for the particular application environment. At the moment, many material datasets generated from various mechanical tests, such as tensile test, vibration, fatigue, etc. cannot fully account for the behaviour of solder joints in an environment dissimilar to that of test conditions. These tests are generally done on bulk solder; the material properties so generated are therefore not reliable when dealing with the tiny solder joints that are in use in microelectronics.

Solder joints in applications may experience many different environmental and operational stress conditions such as temperature fluctuation, moisture ingression, corrosion, electro/thermal/stress migration, shock, and vibration. The availability of test equipment for these loading conditions varies. For example, while for thermal mechanical stress there are lots of options in terms of test equipment selection, dedicated vibration test equipment for BGA sized solder joints is limited, especially when  it is required that the behaviours of the solder joints can be monitored closely. Furthermore, for available test equipment, it is not always straight forward to understand the detailed behaviour of the test specimens because solder joints are small and sensors cannot monitor all the physical processes that take place during testing.

Another issue that was mentioned earlier is that the existing material properties that are used for computer simulation of BGA solder joints have large scatter and therefore are not reliable for reliability analysis. Solder alloys' mechanical properties are highly nonlinear. The visco-plastic strain rate, for example, is dependent on temperature, stress, intermetallics, changes in solder joint manufacturing process, and variation in small changes in alloy composition. This inevitably makes it very difficult to obtain accurate material property data.

In order to address the issues highlighted above, this work is focused on three tasks. Task 1 is to help design test equipment that is suitable for testing small solder joints undergoing vibrational mechanical loading. The significance of this task is that there was no suitable off the shelf equipment that can be used for the experimental testing and a dedicated test machine would fill a vacuum in reliability analysis and material data gathering for small solder joints. In this part of the work, the dynamic Finite Element method was used to analyse the behaviours of the test equipment to ensure its stability and to understand the deformation of solder joint to make sure the specimen are suitable for the test.  The outcome of this part of the work has been presented at EUROSIME 2010 and a paper was published in the proceedings of the conference [14].

Task 2 is to understand the behaviours of BGA sized solder joints in micro-mechanical test equipment that has already been developed successfully at NPL [15]. This test equipment tests BGA sized solder joints under isothermal cyclic loading and the specimens resemble a row of BGAs. A detailed analysis of the behaviours of solder joints have been carried out using finite element analysis and they are compared with test data as well as BGA solder joints in packages under cyclic thermal loading conditions. The results of this work were presented at EMPC 2011 conference [16].

Task 3 was to use the Inverse analysis method to address the issue of lack of consistent material properties to use in analysing lead free solder using computer simulation methods. The issue has been a source of major concern by numerous researchers [17-20]. There is a wide scatter of material properties for the same solder combination from different sources. This therefore poses a serious challenge for researchers performing simulations of lead free solder joints because material properties have a serious impact on simulation results. The objective of this work was to develop an efficient way of obtaining nonlinear properties that are suitable for modelling specific solder joints under specific loading conditions. This is a new approach because traditionally, lengthy experiments were not performed on solder specimens in order to obtain the nonlinear properties that are meant to be used for any solder joints under any loading conditions. The new approach that is used in this work deviates from that tradition and is believed to be more practical for the manufacturing industry. This work on the inverse modelling and the determination of creep parameters was presented at ICEPT 2012 conference [21].

## 1.5 Outline of the Thesis

The work carried out in this research is on the development of solder joint test equipment, acquiring material properties for simulation using inverse Finite Element modelling techniques, and the analysis of the behaviour of lead-free solder during test. The particular lead free solder of interest in this work is SAC305 undergoing vibrational or isothermal cyclic mechanical loading conditions. This lead-free solder combination was chosen as it is widely used in the literature and it provides similar result to that of SAC405. It is also widely acknowledged that the industrial partners have extensive experience in using this lead-free solder combination.

In Chapter 2, reviews of the recent activities in the vibration, fatigue and inverse modelling techniques are presented. Different test methods, simulations and reliability predictions will also be presented.

Chapter 3 will discuss the finite element method (FEM) from the viewpoint of the research and its applications. Particular emphasis will be placed on dynamic and nonlinear analysis. The groundwork will be laid for later application of these theories and techniques to modelling both the equipment and for forward and inverse FEM simulation of solder joints.

Chapter 4 details the solder interconnect and vibration test equipment design and simulations. This chapter will review vibration test equipment in the market as well as the various test methods. Static, dynamic and vibration response of the equipment will also be analysed. The effect of creep on the solder interconnect will also be looked at.

Chapter 5 will discuss about the modelling of solder joints under cyclic mechanical loading using FEA and compare the simulation results with experiments. The effect of various different material datasets in the literature will be analysed. The effect of creep and the available creep models will be simulated and compared to experiment. Lifetime prediction using generalised equations will be completed.

Chapter 6 will discuss about the use of inverse FEM modelling techniques and experimental results to generate material viscoplastic constitutive equations.

Finally a summary of the achievements from this work and possible further work will be discussed in Chapter 7.

# Chapter 2 Solder alloy Properties and Test Methods

There are a number of issues unique to the performance of lead-free solders that were never of major concern with SnPb. One of these is that lead-free solder has a tendency to develop tin whiskers as a result of internal stresses on the tin. Under extreme cold conditions, 13°C and below, lead free solders suffer from tin pest, a transformation of pure white tin to grey tin and this affect the material strength of the solder and integrity is lost [22]. Therefore, in order to determine their reliability, there is a need to develop better understanding of its performance and response to a variety of loading conditions. The widespread acceptance of lead-free solders and its numerous applications in the industry therefore makes the determination of their reliability of paramount importance.

The increased complexity of electronic equipment with its dense array of electronics systems has resulted in an urgent need to understand the failure mechanisms of lead-free solder under dynamic and vibratory loads. Solder joints are being exposed to different and at times extreme loading conditions during their lifetime. In order to improve reliability of electronics devices, various test methods have been developed and used in the industry. The most common reliability test method used is thermal cycling. Using this technique the specimen is subjected to cyclic temperature changes; due to the coefficient of thermal expansion (CTE) mismatch between the solder interconnect and the substrate, strains and stresses are generated in the solder joint. Thermomechanical tests are suitable for rooting out low cycle fatigue and manufacturing defects of interconnects.

To this end there have been considerable research performed over the past dozen years to assess the suitability of the lead-free alternatives as replacement of SnPb. Some of these works are reviewed below.

## 2.1 SnAgCu Lead Free Solder Composition and Properties

There have been a number of lead-free solder alloy proposed in the last decade, Sn-Ag-Cu (SAC) series alloys have emerged as the most widely accepted (Figure 2-1) [23, 24]. Tin was the obvious choice for the primary constituent of lead-free solder because of its relatively low melting point and its ability to form intermetallic compounds with all of the metals that the industry needed to solder [25]. The industry came to the realisation quite early that there were no elements in the periodic table that lowers the melting point of tin from 232$^{o}$C to 183$^{o}$C without undesirable effects. These effects include limited availability, reduced recyclability and reduced reliability. A number of element combinations were tested to determine the best that will replicate the desirable properties of SnPb.

When Bismuth is added to tin making 57% of weight of the composition, this lowers the melting point to 139°C but the resulting alloy is difficult to use in any meaningful way [26]. The addition of 9% of weight of Zinc lowers the melting point to 198°C and while there has been some successful commercial application of alloys based on this eutectic, problems arise from the relatively high reactivity of Zinc [27].

The composition with the least complications that produces an alloy with many properties very similar to those of tin-lead was achieved by adding copper and silver to tin. Tin has a melting point of 232°C and the addition of copper can reduce this by only a few degrees to 227°C, which is still 44°C higher than that of eutectic tin-lead solder. The addition of silver to the tin-copper alloy reduces the melting point by a further 10°C to 217°C which is still 34°C higher than that of tin-lead solder. Solder Tec's survey shows that the most popular SAC are the near eutectic SAC alloys [24], which consist of 3.0-4.0% of Ag and 0.5-1.0% of Copper (Figure 2-1).

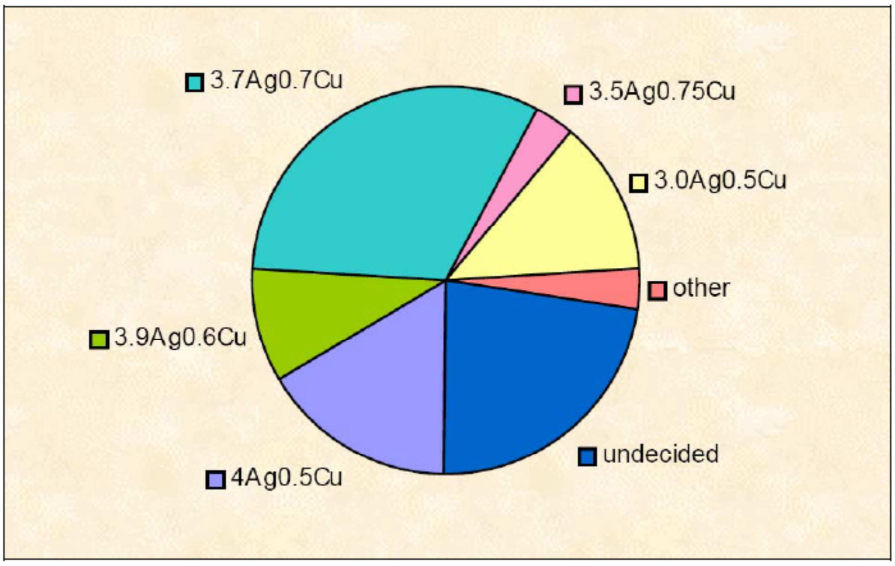

**Figure 2-1 Survey of the market share of different types of SAC alloys [23].**

In SAC alloys, the formation of intermetallic compounds between the primary elements Sn Ag, and Cu affect all the properties of the alloys. There are three possible intermetallic compounds that may be formed: $Ag_3Sn$ forms due to the reaction between Sn and Ag and $Cu_6Sn_5$ forms due to the Sn and Cu reaction, but $Cu_3Sn$ will not form at the eutectic point unless the Cu content is high enough for the formation of $Cu_3Sn$ at higher temperatures, so in bulk specimens $Cu_3Sn$ is not presented. Ag can also react with Cu to form Ag rich α phase and Cu rich β phase. However, there is no reaction between Ag and Cu to form any kind of intermetallic compounds. The particles of intermetallic compounds possess much higher strength than the bulk material [28]. Fine intermetallic particles in the Sn matrix can therefore strengthen the alloys. The intermetallic compounds can also improve the fatigue life of the solders, as SAC alloys are reported to be 3-4 times better in fatigue resistance than the SnPb eutectic solders [29, 30]. The higher fatigue resistance is believed to be contributed by the interspersed $Ag_3Sn$ and $Cu_6Sn_5$ particles, which pin and block the movement of dislocations [22].

## 2.2 A Review of Lead-free Solder Research

Finite element and experimental analysis has been used extensively in analysing the behaviour of solder joint undergoing varying static and dynamic conditions. The power of the finite element method has thus been uniquely demonstrated in a wide array of test conditions simulated and the visualisation power that this method brings to lead-free solder research. The following is a review of published peer reviewed materials from a number of researchers making use of these methods demonstrating the methodology applied following which a summary discussion will be presented. It is not intended as an exhaustive review of solder joints research and the materials are selected to highlight the issues discussed in Chapter 1 of this thesis, and to provide background information for the work that has been carried out in this work.

### 2.2.1 Lead-Free Solder Finite Element Analysis

Finite element analysis have been used extensively in simulating the behaviour of solder joint under varying conditions. Vandevelde et al [31] compared joint reliability of SnPb and SAC joint using non-linear FEA using three packages: silicon CSP, underfilled flip chip and a QFN package. They reported that SAC has lower creep strain rate than SnPb but also that the lead free solder performed worse for extreme loading conditions when using the inelastic dissipated energy density as the damage parameter. This is because the lower creep strain rate results in higher stresses and higher hysteresis loop with more dissipated energy per cycle. Pitarresi, et al. [32] used the finite element method to determine the reliability of flip chip package undergoing thermal cycling. To understand the solder's response and fatigue characteristics, the viscoplastic Anand's creep and Darveaux crack growth models were used. Ng et al [33] also used the finite element method along with Anand's creep model in the study of board level solder joint reliability of BGAs undergoing thermal cycling. Chen et al. [34] modelled the reliability of solder joints in flip chip assemblies with both compliant and rigid substrates using the finite element method and Anand's constitutive model. Their result demonstrated that the flexible substrates have higher reliability than the rigid ones; this improvement was attributed to higher energy dissipation by the flexible substrates. Classe and Sitaraman [35] worked with microBGA assemblies on organic substrates to compare the differences between symmetric and asymmetric accelerated thermal cycles (ATCs) using numerical simulations. The asymmetric ATCs were found to emulate field-use conditions and have the potential to reduce the time for qualification testing. Several finite element models with different solder constitutive models including the viscoplastic Anand's model were applied. The numerical simulations showed little difference between symmetric and asymmetric cycles in predicting solder joint failures. Pang and Low [36] compared the failure life of FCOB solder joints undergoing thermal cycling (TC) and thermal shock (TS) by using finite element modelling. Both the elastic-plastic-creep model and the viscoplastic Anand's model, as well as solder joint fatigue models based on inelastic strain range and inelastic energy density were employed. It was found that solder joints under TC had shorter failure life cycles than in TS testing due to the lower ramp rate. Moreover, compared with the elastic-plastic-creep analysis method, the Anand's viscoplastic method was more effective in modelling the ramp rate effects for both TS and TC conditions.

Rodgers et al [37] performed a comparative evaluation of the leading lead-free solder candidate (95.5Sn3.8Ag0.7Cu) and 63Sn37Pb solder under thermal cycling conditions. A test vehicle consisting of four daisy chained 10x10 array 0.8mm pitch plastic micro ball grid arrays (microBGA) mounted on an 8-layer FR4 printed wiring board was designed. The board finish was organic solder preservative (OSP) for the lead-free devices and hot air solder levelled (HASL) in the case of the eutectic SnPb devices. An event detector was used to monitor the continuity of each daisy chain during accelerated temperature cycling, where the test vehicles were cycled with a ramp rate of approximately 3ºC per minute from –40ºC to 125ºC, with 10-minute dwells and a total cycle time of 2 hours 10 minutes. Results plotted using a Weibull distribution indicated that the SAC solder is more reliable under these conditions. They carried out experiments on large-scale lead-free solder specimens to determine the parameters required for the Anand's viscoplasticity model. The Anand's model was then implemented in finite element analysis using ANSYS®, where the submodelling technique was employed to determine the viscoplastic work per thermal cycle for each solder joint along the package diagonal. Schubert's fatigue life model [38] was used to predict the number of cycles to failure of each joint, although it should be noted that the necessary model parameters may need to be calibrated. Results indicated that the joint under the die edge is likely to fail first and that the SAC solder is more fatigue resistant. The numerical predictions underestimate the fatigue life in both cases. Wang et al [39] used the unified viscoplastic constitutive law, the Anand’s viscoplastic model, to represent the inelastic deformation behaviour for solders used in electronic packaging. The material parameters of the constitutive relations for 62Sn36Pb2Ag, 60Sn40Pb, 96.5Sn3.5Ag, and 97.5Pb2.5Sn solders were determined from separated constitutive relations and experimental results. The achieved unified Anand’s models for solders were tested for constant strain rate testing, steady-state plastic flow, and stress/strain responses under cyclic loading. They concluded that the Anand’s viscoplastic model can be applied for representing the inelastic deformation behaviour of solders at high homologous temperature and can be recommended for finite element simulation of the stress/strain responses of solder joints in service.

### 2.2.2 Lead free solder Experimental Techniques

A wide array of different experimental techniques has been applied in the analysis of lead free solder joints. These techniques range from basic tensile tests to thermal cycling and high strain rate tests. Following is a review of some of this work. Wei et al [40] investigated lead-free solder material 95.5Sn3.9Ag0.6Cu under isothermal fatigue loading. The effects of strain rate on hysteresis loops and fatigue life in SAC solder have been investigated at room temperature. Using damage mechanic theory they characterized the isothermal fatigue behaviour of the material using a fatigue failure criterion that is based on the concept of damage accumulation in solder material. The model was validated using experimental data and it was found that it was capable of predicting the effects of loading rate on fatigue life and cyclic behaviour. The effect of temperature and microstructure was needed to present a complete understanding of the underlying behaviour of the damage mechanics. Zhang et al [41] presented and discussed the results of the investigation on the fatigue fracture behaviours in a series of as-soldered and thermal-aged copper/lead-free solder joints deformed under both monotonic and cyclic loadings. Their observation results showed that fatigue cracks generally initiate around the IMC/solder interface when the loading axis is orthogonal to the interface. The intrinsic deformation behaviours are little different for different solder joints resulting from strain localization induced by the strain mismatch. Fracture surface observations revealed that the crack propagation path and fatigue resistance of the solder joints can be affected by the yield strength and mechanical property of the solder. When the copper/solder interface is parallel to the loading axis, the interfacial IMC layer failed approximately perpendicular to the interface when the cumulative strain exceeded the fracture strain, then the cracks propagated to the IMC/solder interface, leading to the fracture along the interface. The failure mechanisms and factors influencing interfacial fatigue are discussed.

Siviour et al [42] measured the mechanical properties of 63 Sn37Pb and lead-free solders at high strain rates (500 – 3000 $s^{-1}$) using a split Hopkinson pressure bar. The solder specimens were produced by quenching in water from the melt, to give the phase structure associated with rapid cooling. Measurements were made at −40 °C, room temperature and +60 °C. The property of SnPb solder was strongly strain rate and temperature dependent, whereas the lead-free solders' property showed only a weak dependence on these parameters. All of the materials behaved elasto-plastically until a plateau stress of circa 200MPa is reached. They also presented results on the mechanical strength of solder balls, produced to mimic solder joints at high rates of strain. When these balls were aged no change in their properties was observed. This may be because the change could not be resolved in the experiments performed. They also noted that an important cause of weakening in solder joints is the growth of intermetallics between the ball and the substrate. Fei et al [43] investigated the dynamic mechanical behaviours of 63Sn37Pb, 96.5Sn3.5Ag and 96.5Sn3.0Ag0.5Cu solder alloys at high strain rate by using the split Hopkinson pressure/tension bar testing technique. Stress-strain curves of the three materials were obtained at strain rate 600 $s^{-1}$, 1200 $s^{-1}$ and 2200 $s^{-1}$, respectively. The experimental results show that all the three materials are strongly strain rate dependent. Among them 96.5Sn3.5Ag is the most sensitive to strain rate, while 96.5Sn3.0Ag0.5Cu has the greatest yield stress and tensile strength. Relations of the tensile strength, fracture strain and yield stress of the materials with strain rate were proposed by fitting the experimental data.

Zamiri et al [44] showed that the crystal orientation of the tin phase in a Pb-free Sn solder joint has a significant effect on the stress state, and hence on the reliability of the solder joint. A set of crystal plasticity analyses was used to evaluate the stress and strain resulted from a

165°C temperature change in a single-crystal joint using two simplified geometries used in practical solder joints. Phenomenological flow models for ten slip systems were estimated based upon semi-quantitative information available in the literature, along with known anisotropic elastic property information. Their results show that the internal energy of the system is a strong function of the tin crystal orientation and geometry of the solder joint. The internal energy (and presumably the likelihood of damage) is highest when the crystal c-axis lies in the plane of the substrate, leading to significant plastic deformation. When the a-axis is in the plane of the interface, deformation due to a 165°C temperature change is predominantly elastic. The texture of the copper substrate using isotropic Cu elastic properties does not have a significant effect on the stress or strain in the Sn phase of the joint. Geng [45] performed a close examination of creep curves for Sn-based solders and showed that steady-state creep is an ill-defined stage and that primary and tertiary creep are both significant. In order to account for these effects in solder constitutive models, he presented a phenomenological model that predicts entire creep curves for Sn-based solders. His proposed constitutive model is an extension of the Omega method for tertiary creep of steel alloys to primary and tertiary creep of Sn-based solders. The new creep modelling approach is of use for stress/strain and reliability analysis of lead-free solder joints.

### 2.2.3 Drop and Shock Test

Drop test of component boards has been conducted extensively over the past few years by a number of authors [46, 47]. It is used to evaluate the device's resistance to damage caused by impact loading which is most relevant for portable electronics devices and transport applications. Compared to the stresses and strains developed in a temperature cycling test, drop test creates very high stress in a very short period of time. The drop tests are referred to as horizontal drop, vertical drop, in the horizontal plane or vertical plane. The test are all drop tests where the test specimens are dropped from a specified height depending on the test condition, the orientation of the samples is reference in the literature as either horizontal or vertical.

Lim et al. [46] carried out product level and board level drop tests on a mobile phone and its PCB respectively. In these tests, the test vehicle was gripped in various orientations and allowed to strike the impacting surface under gravity forces from desired heights using a drop tower. Results indicated additional levels of deformation of the PCB in case of product level drop due to severe rebound impact. Also, drop impact responses of various mobile phones and personal digital assistants (PDAs) were carried out at various orientations from a drop height of one meter and accelerations, strains and impact forces were measured. Maximum PCB strains and accelerations were recorded in product level drop in the horizontal plane. A similar test was also carried out by Arra et al.[47] on free fall board level and product level drops of area array LGA packages and measured the accelerations at the board and package side. It was found that the accelerations obtained in case of phone drop were much lower than those in the corresponding board level drop. However, FEA results showed higher values for PCB warpage and maximum plastic strain in the solder joints in case of product level drop.

Lall et al. [48] conducted displacement controlled board level bend tests on BGA packages on an electrodynamics shaker at displacement rates corresponding to dynamic loading using a servo-hydraulic mechanical test system. A number of researchers have pursued methods involving different equipment other than shakers for dynamic loading. Using a customized drop tester equipped with a drop control mechanism, Pitarresi [49] and Wu et al. [50] carried out shock testing of test boards on a four–point-bend like shock test fixture at fixed and incremental shock levels and in-situ continuity monitoring of the solder joints was carried out to detect failure. In order to replicate the shock experienced by the PCB inside an actual PC motherboard, experimental modal analysis was carried out on the motherboard and its fundamental frequency was obtained. The test setup was then adjusted to match the fundamental frequencies of the system with the tested motherboard. Complimentary to this is the work from Wang et al. [51], who performed free-fall board drop test analysis in the horizontal direction on FCOB assemblies using a shock test machine providing the half sine pulse for impact excitation. Three-point bending and four-point bending tests [52] were carried out to investigate the fatigue failure of solder interconnects due to excessive cyclic PCB bending and flexure which may occur due to drop impact. The tests were carried out on a servo-hydraulic machine and the daisy-chained packages are continuously monitored to detect failure. To analyse strain rate effect during shock test Tee et al. [53] carried out testing of eutectic solder using Split Hopkinson Pressure Bars (SHPB) to show the effect of higher strain rates on the dynamic properties of solder. Bansal et al. [54] performed high speed four point bend tests with strain rates greater than 5000 microstrains per second in accordance with IPC/JEDEC 9702 [55] to mimic brittle fractures of flip chip BGA packages during PCB assembly operations with both lead and lead-free solder alloys and ENIG pad finishes. Results indicate that the strains to failure decrease with increase in the strain rates. Shear tests at high strain rates similar to those experienced by the solder joint during drop impact were carried out on BGA and LGA packages to determine the package to board interconnection shear strength.

Chong et al. [56] conducted board level drop test in accordance with the JEDEC test standards [2003] by mounting a TFBGA package in the centre of the PCB. Comprehensive dynamic responses of the PCB and the solder joints such as accelerations, strains and resistances were measured and analysed using a multi-channel real-time electrical monitoring system. The study suggested a correlation between the dynamic strains in the PCB caused by the multiple flexing of the PCB and mechanical shock and the resulting solder joint fatigue failure. Lall et al. [57, 58] performed controlled drop tests of BGA and CSP packages from different heights in a direction perpendicular to the floor. Various experimental parameters such as relative displacements, strains, velocities, accelerations etc. were acquired simultaneously. Failure analysis of the failed test specimen showed solder joint failures at the package and board interfaces and copper-trace cracking.  Also, Mishiro et al. [59] showed correlation between the PCB strains and solder bump stresses by performing drop tests of BGA packages mounted on a motherboard. The study also showed the dependence of solder joint stress on package design and structure and stress reduction by including underfills.

### 2.2.4 Vibration testing

Another test method that has become more and more important is the vibration test. Current industry standards for vibration testing rely mainly on pass or fail functional test criterion, with limited knowledge of the factors contributing towards the failure of the components. There is also no measurement metric available that could be effectively used to monitor the fatigue of solder joints under vibratory loading. The work in understanding solder joint reliability in terms of vibratory loading has been gaining momentum in the research community. Test results reported by Osterman and Dagupta [60] of SnPb and Sn-3.0Ag-0.5Cu solder joints under vibration loading conditions, found that for lower stresses Sn-3.0Ag-0.5Cu outperformed SnPb whilst at higher stresses the situation reversed. The crossover point for this change was at "medium stress level" where the number of cycles to failure was between 104 and 105. Due to the similar power law exponents (represented as gradients on an S-N diagram) the absolute values for lifetimes of the soldiers were, however, largely similar. This was confirmed also by Di Maio and Hunt [61] who reported that SnPb highly outperforms Sn-3.0Ag-0.5C at higher frequencies above 100Hz, whilst the difference is smaller at lower frequencies. Stam and Davitt [62] have conducted vibration tests on a range of component and substrate coatings, comparing the reliability of SnPb to that of Sn-3.8Ag-0.7Cu. They found that the difference between the solder types was less significant than the component type or substrate coating (e.g. Cu or Ni).

The lack of adequate testing equipment has led to a number of researchers developing prototypes to perform a set of testing regimes. Matilla [63] investigated a vibration tester and compared it to the JESD22-B111 standard drop tester to overcome the drawbacks related to drop testing. From the testing point of view they concluded that the vibration testing has the following advantages over the drop testing: i) more versatile measurements can be carried out because the component board does not travel large distances during the test, ii) more careful control of the test environment (e.g. temperature) is possible, iii) constant bending and stress amplitudes during vibration testing make mechanical analyses and life predictions easier, and finally, iv) vibration tests can be carried out in much less time and effort as compared to drop testing. They compared stresses produced during the experiments to numerical results using the finite element method. The analyses showed that even if the bending amplitudes are equal in both tests the stress histories are different. The most important difference between the vibration and the drop test is that bending of the component board is constant during the vibration test, while in the drop test the amplitude is reduced after each impact. The vibration test makes use of the resonance phenomenon to generate large constant bending amplitude with a small harmonic force. In the drop tests the higher frequency modes and their interaction with the lower natural frequencies complicate the stress histories in solder interconnections.

Tsai et al [64] developed a loading apparatus and observation technique that allowed ball grid array (BGA) packages to be visually inspected during high cycle vibration testing. Their system provides controls for varying the cycling frequency and magnitude of the applied load. The failures of solder interconnect in BGA specimens were recorded by direct visual monitoring method. Stroboscopic video was employed to freeze the motion of the vibrating solder interconnects while showing the real-time evolution of failure. In all test cases, BGA interconnect failure was observed to be the result of crack initiation and propagation along the nickel/solder interface. A primary crack developed at one edge of the interconnect and progressed stably until a secondary crack initiated from the opposite edge. The crack growth accelerated until these cracks coalesced, resulting in complete separation of the interconnect. The percentages of time spent in crack initiation, stable propagation and accelerated propagation are, on the order of 15%, 60% and 25%, respectively. Vibration tests at frequencies ranging from 50 to 100 Hz were performed and the number of cycles to failure was found to be frequency-independent in this range. Several commonly used damage mechanics and fracture mechanics fatigue life-prediction models were examined based on failure parameters computed from a nonlinear finite element analysis. It was found that while the damage models examined show large discrepancies between predicted and actual cycles-to-failure, the fracture model correlates with the test data within a factor of 1.5. Hin et al [65] developed a dynamic test board (DTB) for shock and vibration (S&V) testing. The test board was used to characterize the solder joint reliability (SJR) of the component corresponding to the specified dynamic test requirement. The dynamic behaviour and properties are investigated in the development of a flip chip ball grid array package (FCBGA). One of the significant findings is that board strain is correlated with the solder joint failure location. Hence, they introduced board strain as a predictor for S&V SJR risk and component strain limit definition in S&V condition.

Perkins et al [66] aimed to develop an experimental and modelling approach that can accurately determine the solder joint behaviour of electronic components under vibration conditions. In particular, they discussed the out-of-plane sinusoidal vibration experiments at

1G. Detailed investigation and characterization involving dye-and-pry analysis, microstructural examination, and numerical modelling enabled the development of a high-cycle stress-based equation for lead-containing CCGA under sinusoidal loading. They applied their developed method to a number of cases including a CCGA package with a heat sink as well as a CCGA package subjected to frequency sweeps. It is seen that the predictions from the developed model agree well with experimental data and that the developed model can map the evolution of solder damage across all solder joints and can also provide important design recommendations in terms of solder joint location as well as heat sink attachment.

Wu et al [67] emphasizes a rapid assessment methodology using the design of experiments (DOE) approach to determine fatigue life of ball grid array (BGA) components in random vibration environment. They reported that the most critical dynamic loading occurs when the dominant frequency approaches the natural frequency of the printed wiring board (PWB) assembly. Their approach involved global (entire PWB) and local (particular component of interest) modelling approach. In the global model approach, the vibration response of the PWB is determined. Their global model gave the response of the PWB at specific component locations of interest. This response is then fed into a local stress analysis for accurate assessment of the critical stresses in the solder joints of interest. The stresses are then fed into a fatigue damage model to predict the life. The solution is achieved by using a combination of finite element analysis (FEA) and physics of failure to BGA damage analysis.

Grieu et al [68] implemented damage calculation of solder joint under random vibration. The essential point of their method relies on the analysis of stresses in the time-domain. Stress histories are thus obtained from calculation and post-treated for damage estimation. The computation procedure establishes time-stress responses from transfer functions obtained by FEM vibration simulation. These time-responses are computed with the rain flow cycle counting method. Then, a damage calculation using Palmgren-Miner’s rule and Basquin’s law is done. The adjustment with experimental results appears to be difficult with a limited number of test data. Selvakumar et al [69] performed random vibration on an electronic package using Joint Electronic Device Engineering Council’s (JEDEC) JESD22-B103B standard. The electronic package mounted at the centre of the printed circuit board was subjected to vibration, variable frequency condition ‘D’ of JEDEC standard for 30 min. After 30 min of random vibration test, the component lead-wires, solder joints, and PCB were thoroughly inspected for failure. From their observations, it was found that no failure occurred during the test period. The fatigue life of the component, estimated using an empirical lifetime model, was found to be 96.48 hours. Eckert et al [70] demonstrated that the interaction of combined loads has to be considered in lifetime estimates of electronic packages. They discuss lifetime prediction for lead-free soldered flip chips under vibration load in different temperature environments in terms of solder joint fatigue. Parameters for lifetime modelling are obtained from non-linear and temperature-dependent finite element analysis and lifetime experiments. They introduced temperature dependent coefficients and exponents for the Coffin-Manson-Basquin relationship considering elastic and plastic fatigue behaviour. Their results indicate that temperature is an important parameter affecting the solder joint vibration fatigue life.

Tu et al [71] looked at the effect of the $Ni_3Sn_4$ and Cu–Sn intermetallic compound (IMC) on the fatigue lifetime of lead free solder. During the vibration fatigue test, in order to identify the failure of BGA solder joint, electrical interruption was monitored continuously through the daisy-chain network. They studied the vibration fatigue failure of μBGA solder-joints reflowed with different temperature profiles, and aging at 120 °C for 1, 4, 9, 16, 25, 36 days. Their results show that the fatigue lifetime of the solder joint firstly increases and then decreases with increasing heating factor, which is defined as the integral of the measured temperature over the dwell time above liquidus (183°C) in the reflow profile. The lifetime of the solder joint decreases almost linearly with the increasing fourth root of the aging time. The SEM/EDX inspection shows that $Ni_3Sn_4$ IMC and $Cu_6Sn_5$/$Cu_3Sn$ IMCs are formed at the interface of the solder/nickel-plated PCB pad, and the no-aging solder/component-metallization, respectively. Also during long term aging, $Ni_3Sn_2$ and NiSn were found at the Ni/Solder interface with X-ray diffraction, except $Ni_3Sn_4$. For non-aged solder joint, the fatigue crack generally initiates at the interface between the $Ni_3Sn_4$ IMC and the bulk solder. Then it propagates mostly near the Ni/solder interface, and occasionally in the IMC layer or along the Ni/solder interface. After aging, the fatigue crack mostly initiates and propagates in the $Cu_6Sn_5$-phase/bulk-solder interface or the $Cu_3Sn$/$Cu_6Sn_5$ interface on component-metallization. Evidently, the intermetallic compounds contribute mainly to the fatigue failure of BGA solder joints. They concluded therefore that the thicker the IMC layer, the shorter the fatigue lifetime of the solder joint. The initial formation of the IMCs at the interface during soldering ensures a good metallurgical bond between the solder and the substrate. However, a thick IMC layer influences the toughness and strength of the solder joint, which results in mechanical failure.

Although vibration test has its advantages, generally they are not reflective of the service conditions that the device will be subjected to. Also most of the vibration tests are single axis, there are very few reported multi-axis vibration test in the literature, this is due in part to complexity in analysing and interpreting the results and also to cost. To address this limitation the industry makes use of the highly accelerated lifetime test (HALT) method.

### 2.2.5 HALT testing Procedure

Electronics product quality and reliability have been determined through traditional testing methods such as vibration tests, thermal cycling, mechanical shock, thermal shock, and a varied combination of these. The core philosophy of this testing method is to define a set of specifications, usually minimum or maximum temperatures and/or vibration levels, and to conduct the tests by changing only one variable at a time. Vibration testing is performed one axis at a time. If the device is still functional after being tested according to the test specs, it is considered to have passed. This type of testing does not provide an accurate representation of how the product might perform in service. As the industry progresses towards more and more miniaturization it become clear that these test are not adequate. Changing the variables one at a time and performing one dimensional vibration tests are not reflective of the real world operating environment. The use of HALT can lead to greater levels of product quality and reliability.

Highly Accelerated Life Test (HALT) is a process in which products are subjected to accelerated environments to find weak links in the design and/or manufacturing process. The primary accelerated environments include thermal (both temperature limits and rate of change) and vibration (pseudo-random 6 DOF). Other accelerated environments using voltage, frequency, etc. are applied as appropriate for the sample being tested. HALT is therefore a misnomer, as it is not a true life test but a process to determine the operation and endurance limits through the following process steps: cold limit determination, hot limit determination, rapid thermal cycling, vibrations limit determination and the combined environments response [69].

HALT exposes the product to a step-by-step cycling in environmental variables such as temperature, shock and vibration See figure 2-2). HALT involves vibration testing in all three axes using a random mode of frequencies. Finally, HALT testing can include the simultaneous cycling of multiple environmental variables, for example, temperature cycling plus vibration testing. This multi-variable testing approach provides a closer approximation of real-world operating environments [72].

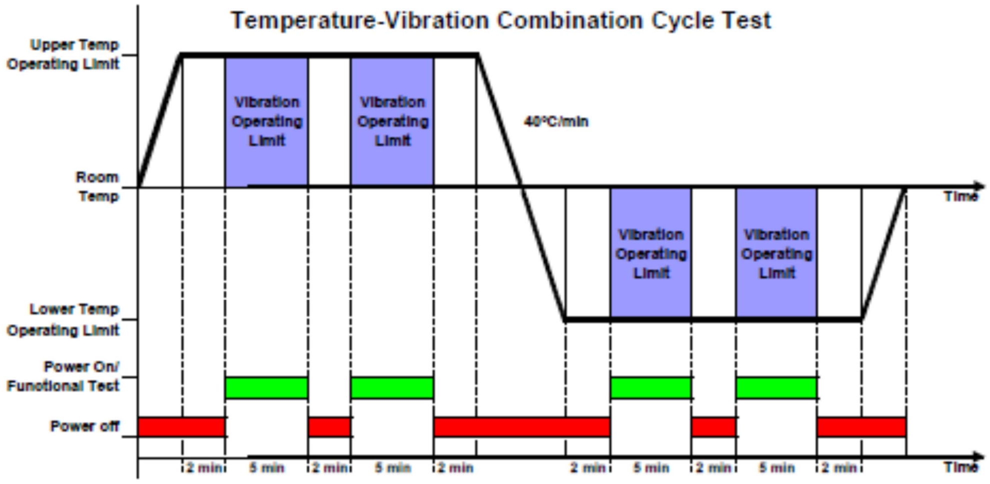

**Figure 2-2 HALT procedure performed by Dell on computer motherboards [72]**

Unlike conventional testing, the goal of HALT testing is to break the product. When the product fails, the weakest link is identified, so engineers know exactly what needs to be done to improve product quality. After a product has failed, the weak component(s) are upgraded or reinforced. The revised product is then subjected to another round of HALT testing, with the range of temperature, vibration, or shock further increased, so the product fails again. This identifies the next weakest link. By going through several iterations like this, the product can be made quite robust. With this informed approach, only the weak spots are identified for improvement. This type of testing provides so much information about the construction and performance of a product that it can be quite helpful for newer engineers assigned to a product with which they are not completely familiar. HALT testing must be performed during the design phase of a product to make sure the basic design is reliable [72].

## 2.3 The Mechanical Properties of SAC Solder

Solder joint reliability is a major concern for the electronics industry, the solder joints are exposed to different loading conditions, temperature, strain rate, etc. and the mechanisms of failure are many and varied. One of the major failure mechanisms of electronic assemblies is that of fatigue failure. To be better able to predict the behaviour of the solder undergoing fatigue loading reliable material properties data are needed coupled with comprehensive solder constitutive equations. This has been the Achilles heel of lead free solder research and application in that accurate material properties for a particular loading condition are not always available.

There are discrepancies of the material properties datasets available in the literature, possibly due to a number of factors including the materials used, fabrication methods, loading conditions, temperature, strain rate, etc. (see Table 2-1). A survey of the literature on Anand's creep model material parameters is detailed in Appendix C and the discrepancies highlighted above are demonstrated in the wide variation of parameters.

**Table 2-1 Tensile material properties for SAC solder alloys**

| Solder Alloy | E(GPa) | UTS (MPa) | YS (MPa) | Strain Rate | Reference Source |
|---|---|---|---|---|---|
| Sn-3.9Ag-0.5Cu | 50.3 | 36.2 | 31.9 | $4.2\times10^{-5}$ | Vianco [73] |
| | 54 | | | | Vianco [73] |
| | | 60 | | $1.78\times10^{-3}$ | Xiao [74] |
| | | 41 | | $1.78\times10^{-3}$ | |
| Sn-3.8Ag-0.7Cu | 43.1 | | | | Pang [75] |
| | | 40 | 35 | $6.68\times10^{-4}$ | Hwang [76] |
| | 50 | 45 | | $1.67\times10^{-3}$ | Fouassier [77] |
| | 44.4 | 39.6 | 35.1 | $5.6\times10^{-4}$ | Pang [78] |
| | 46 | | | $1\times10^{-4}$ | Wiese [79] |
| | 44.9 | | | | Li [80] |
| | 41 | 39 | 32 | $10^{-3}$ | Lin [81] |
| | 46 | | 47.1 | | Harrison [82] |

| Solder Alloy | E(GPa) | UTS (MPa) | YS (MPa) | Strain Rate | Reference Source |
|---|---|---|---|---|---|
| Sn-4.1Ag-0.7Cu | 43 | 36 | 33 | $6.86\times10^{-4}$ | Hwang [83] |
| Sn-3.0Ag-0.5Cu | 54 | 41.8 | 25.3 | $4\times10^{-3}$ | Kanchanomai [84] |
|  | 37.4 | 43 | 37 | $5\times10^{-4}$ | Zhu [85] |
| Sn-4.0Ag-0.5Cu | 40 |  |  |  | Wiese [79] |
|  | 48.3 |  |  |  | Rhee [86] |
|  | 45 |  |  |  | Chromik [87] |
|  |  | 51 |  | $1\times10^{-3}$ | Xiao [74] |
| Sn-3.1Ag-0.5Cu | 45 | 49 | 40 | $6.86\times10^{-4}$ | Hwang [83] |
| Sn-3.5Ag-0.7Cu |  | 44.6 |  |  | Wiese [79] |

Two mechanical methods favoured to extract the constitutive properties of solders are by directly loading [87] or indenting [88] actual solder joints such as BGA solder balls or flip chip solder bumps. While such approaches are attractive because the true solder microstructure is involved, the unavoidable non-uniform stress and strain states in the joint make the extraction of the correct mechanical properties or stress-strain curves from the recorded load-displacement data very challenging.

It is well understood that the temperature and strain rate affect the material properties of different materials. The mechanical properties of solder are temperature as well as strain rate dependent as a result of their high homologous temperature. Therefore the data generated from any test will have to be identical in all aspects or else the dataset will only be valid for the said conditions to which it was performed. The table 2-1 summarises the material properties as reported by different research groups of the major lead-free solders. The data presented are at room temperature. There is a wide variability in all the material properties reported. The Young’s Modulus ranges from 31 – 53 GPa, (Figure 2-4), the yield stress ranges from 31 - 60MPa (Figure 2-5).

The variations in material properties are accounted for by the difference in strain rate, specimen size, testing conditions and testing method.

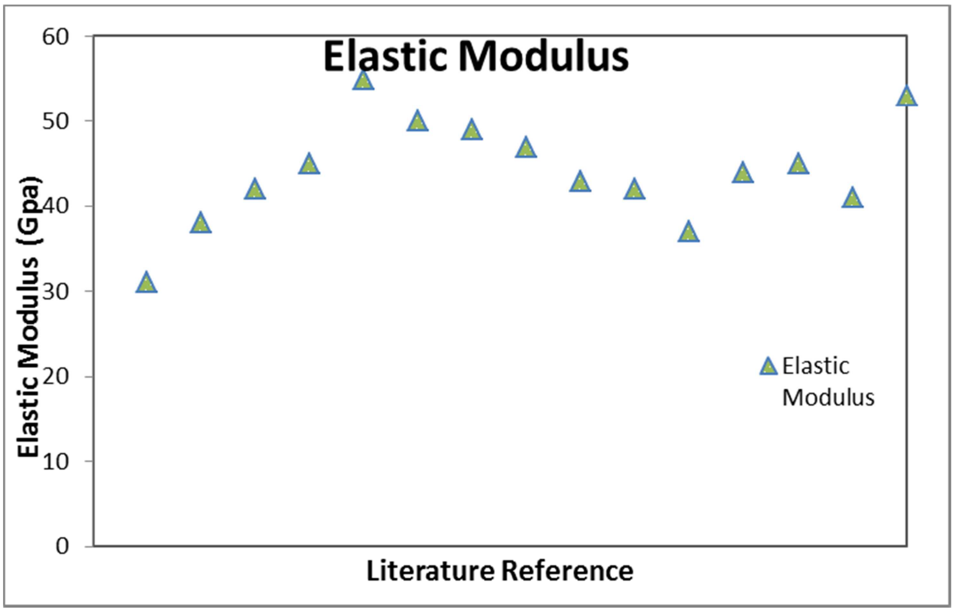

Figure 2-3 Variation in the Elastic Modulus of SAC Solders.

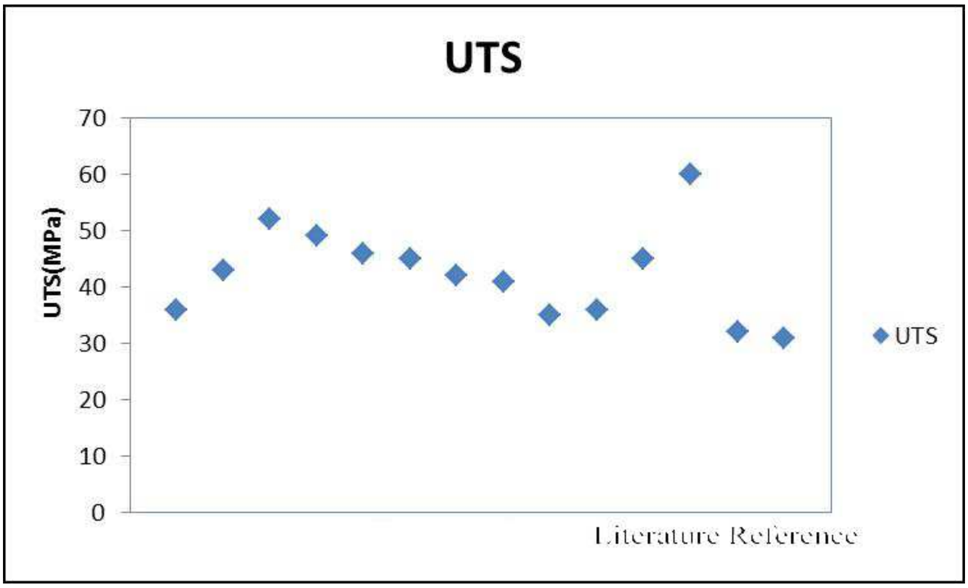

Figure 2-4 Variation in the UTS for SAC Solders

This difficulty with material properties does not affect only lead-free solders. The collected data shows there are also large variations in the mechanical properties published for eutectic Sn-Pb solder, with the elastic modulus ranging from 16 to 36 GPa, the UTS values ranging from 26 to 47 MPa and the Yield stress ranging from 27 to 41 MPa. MacCabe and Fine [89] reviewed the elastic modulus of Sn-eutectic solders and found a wide range, varying from 15 to 40 GPa. They concluded that the large differences were caused by the contribution of the inelastic deformation (plastic) from the slope of the stress-strain curve due to the high homologous temperature of solders. The slope of the stress-strain curve therefore does not represent the true elastic modulus.

As the above data shows, there are large discrepancies in the current database of mechanical properties for both lead-free and Sn-Pb solders. These discrepancies may have been caused by the lack of accepted standards for testing methods, specimen preparation, solder composition and testing conditions.  Using a generic material dataset from the literature therefore poses a unique problem when it comes to interpreting the result of the analysis. In this regard, it is the aim of the present work to utilise inverse modelling techniques to determine the material properties using both experimental and simulation data. The solder joint creeps during the experimental procedure, therefore understanding the mechanism of creep is vitally important.

## 2.4 Creep

Electronic assemblies are often subjected to long periods of constant elevated temperatures. Under such environments, the solder joints are susceptible to creep. Even at room temperature, because of the low melting point, solder alloy creep is significant. Therefore, creep deformation is one of the major failure modes of solder joints for electronic packaging modules [90].

### 2.4.1 The Creep Phenomenon

Creep is a slow, time-dependent permanent deformation that occurs when a material supports a constant load that is below the yielding point for a very long period of time. The level of load/stress and the temperature are dominant factors in creep deformation.

For most materials, creep develops in three stages, namely, primary, secondary and tertiary creep. A typical creep curve for solder is shown in Figure 2-6. The creep response begins with an initial instantaneous strain, which consists of the elastic or time-independent plastic deformation as soon as the constant load is applied [91, 92, 93]. The creep deformations then occur. They are typically divided into three regions or stages as discussed below:

Stage I: Primary Creep - In this stage, the creep strain rate (dε/dt) decreases rapidly over time due to strain hardening, which restricts the deformation.

Stage II: Secondary Creep or Steady-State Creep - In this stage, the creep strain rate is relatively stable (linear part of the curve) as strain hardening and recovery softening reach a dynamic balance. For metals, if the homologous temperature is greater than 0.5, most plastic deformation during creep will occur in this stage. At elevated temperature, strain hardening is associated with subgrain formation caused by the rearrangement of dislocations. On the contrary, recovery and/or recrystallization softening are related to thermally activated cross-slip and edge dislocation climb [94].

Stage III: Tertiary Creep - Tertiary creep is characterized by an accelerated creep strain rate, which may be caused by various weakening metallurgical instabilities such as localized necking, corrosion, intercrystalline fracture, formation of microvoids, dissolution of strengthening second phases, etc. [89]. Eventually, at the end of this stage, rupture occurs.

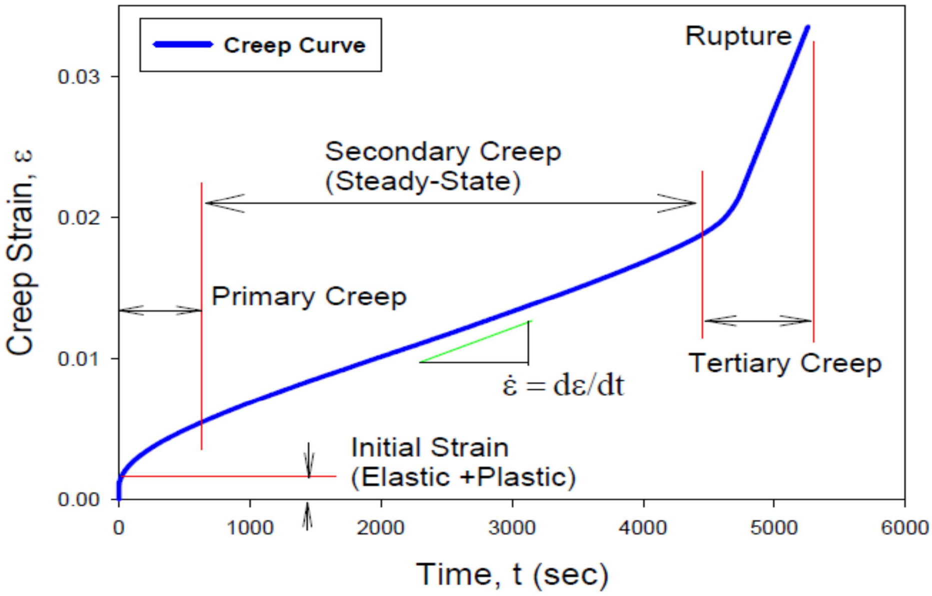

**Figure 2-5 Creep Curve under Constant Stress/Load and Temperature[89]**

### 2.4.2 Creep Mechanism

Creep deformation becomes critical when the temperature exceeds one-half the melting temperature in Kelvin (K) of the material. This is the case for most soldering alloys at room temperature. Several creep mechanisms have been proposed such as dislocation glide, dislocation creep, grain boundary diffusion, and lattice diffusion. A widely accepted deformation mechanism map of the dominant creep mechanisms is shown in figure 2-6. This deformation map was first constructed by Ashby and his co-workers [95], based on the idea that plastic deformation is a kinetic process occurring on the atomic scale. The kinetic processes include mechanical twinning, glide and/or climb of dislocations, the diffusive flow of individual atoms, and the relative displacement of grains by grain boundary sliding (involving diffusion and defect-motion in the boundaries). These are the underlying atomistic processes that cause plastic flow or deformation and contribute to deformation and depend on factors as strain, strain-rate, and temperature.

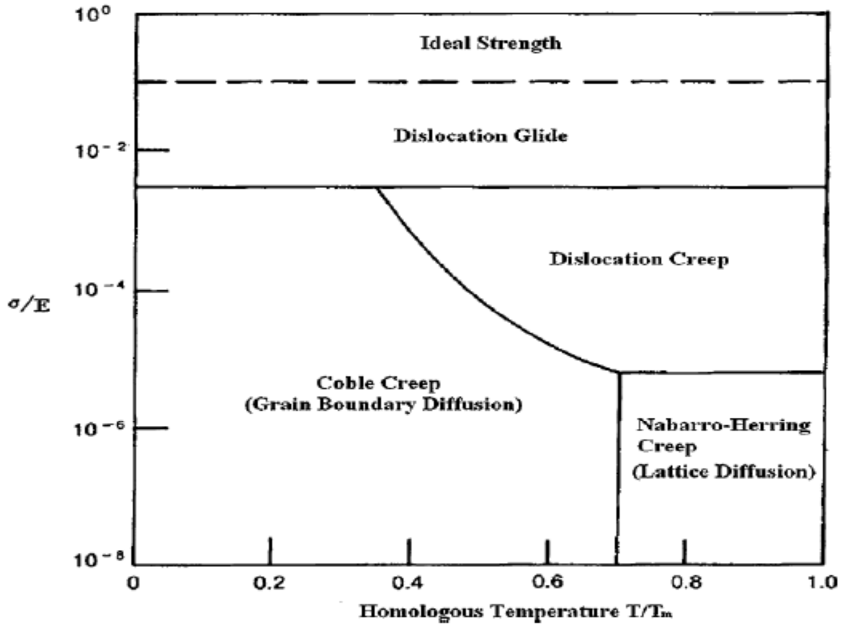

Figure 2-6 Creep Deformation Map for Solder Alloys [92, 95, 96]

In the deformation map shown in figure 2-6, the abscissa is the homologous temperature and the ordinate is normalized tensile or shear stress. Five zones are defined on the map, each of which corresponds to a particular deformation mechanism. These zones are:

Zone 1: Ideal Strength - Plastic flow occurs when the ideal shear strength is exceeded.

Zone 2: Dislocation Glide. This occurs at high stress levels over the entire homologous temperature range. The dislocations move along the slip planes [96].

Zone 3: Dislocation Creep. This is characterized by a high-temperature deformation mechanism with homologous temperatures greater than 0.5Tm and requiring intermediate high stress [96]. The deformation results from diffusion controlled dislocation movement, with dislocations climbing away from barriers.

Zone 4: Grain Boundary Diffusion – Coble Creep. This is a grain boundary based diffusion mechanism involves atomic or ionic diffusion along the grain boundaries. The deformation occurs at intermediate low stress levels over a low to intermediate temperature range.

Zone 5: Lattice Diffusion – Nabarro-Herring Creep. This occurs at low stress level and high temperature. Interstitial atoms and lattice vacancies along the gradient of a grain boundary migrate in reversed directions in the presence of tension or compression pressure. Lattice or bulk diffusion becomes the primary deformation mechanism under this circumstance [94].

In Nabarro-Herring creep, if there is no pressure, interstitial atoms and lattice vacancies will migrate in proportion to the gradient of their concentrations. Under pressure, the lattice defects tend to move in directions to relieve the imbalance of pressure. The movement will eventually cause creep deformation.

Grain-boundary sliding is another possible creep deformation mechanism at high temperatures and is caused by applied stress. However, this mechanism is not independent, and is associated with other deformation mechanisms aforementioned. Due to the high homologous temperature (> 0.5Tm) of most solder alloys under normal operating conditions, the stress level determines the creep deformation mechanism. At low stress levels, the controlling mechanism is lattice diffusion and grain-boundary diffusion. As the stress rises to intermediate levels, dislocation creep takes over, and at high stress level, dislocation gliding becomes dominant. Additionally, the contribution of grain boundary gliding to creep deformation should be taken into account at all stress levels [97].

## 2.5 Effect of Strain Rate and Temperature

The response of lead free solder to various loading conditions has been demonstrated by a number of researchers [98-100], all of these works have indicated that the response of the solder specimen is dependent on the strain rate at which the experiments were performed. It is very important that the temperature at which the analysis were performed and strain rate be included when a comparative analysis of the behaviour of a solder joint is being analysed. The response of a solder joint specimen is shown in figure 2-7 and figure 2-8. It shows that as the temperature increases the saturation stress decreases for constant strain rate. The stress v strain at constant temperature graph shows that increasing the creep strain rate increases the saturation stress. This stress-strain relationship has been observed experimentally by many but there is a wide scatter in the measured strain rates in the literature. To demonstrate spread in material data figure 2-9 plots similar experiments performed by Xiao[74], Xu[88] and Vianco[73]. This plot shows that for a particular stress, the strain rates predicted by the above researchers are very different.

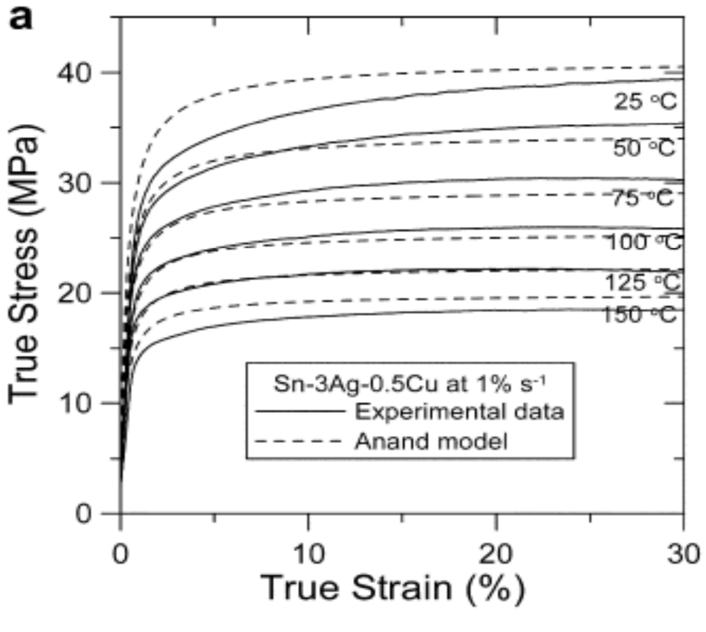

**Figure 2-7 Response of solder at fixed strain rate but different temperature [18]**

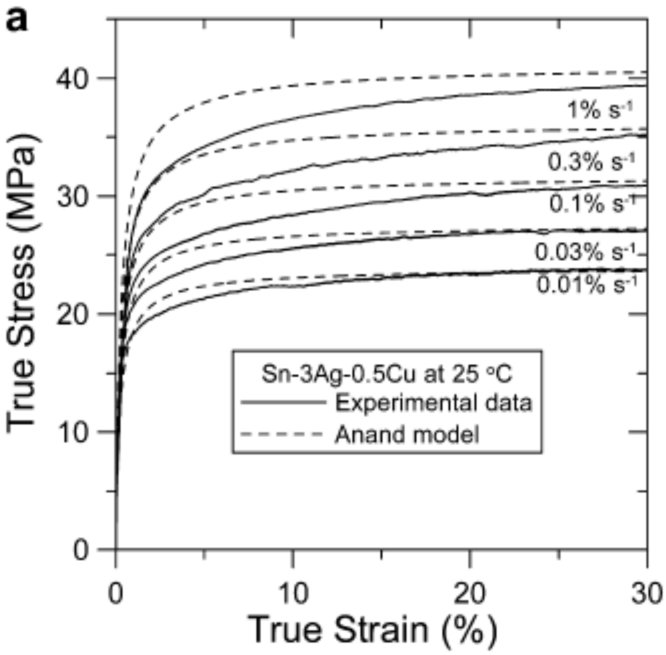

**Figure 2-8 Response of solder at different strain rate [18]**

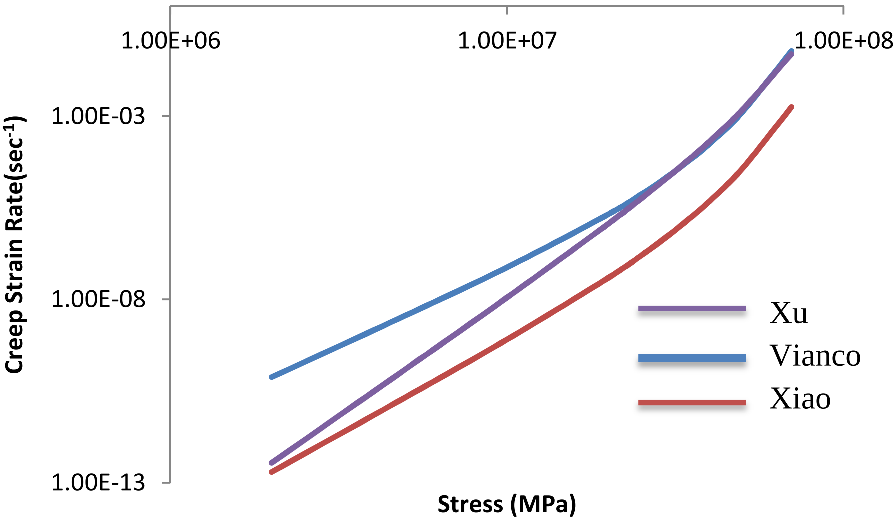

**Figure 2-9 Variability of material data in the literature**

## 2.6 Lifetime Models

The ability of models/equations that predict the lifetime of a solder joint and hence its reliability is a quest taken seriously by numerous authors. These lifetime models/equations inform researchers of the important parameters that are required to carry out the analysis. A brief discussion will hereby ensue about the various techniques that have been applied to determining the lifetime of solder in microelectronics. The lifetime prediction equations are different depending on the response regime being analysed. The main variables in the assessment of solder joint lifetime are the stress and strain. The stress generated by an applied strain can either result in elastic or plastic deformation. Most of the plastic deformation in solder develops with time, referred to as creep strain and is a function of the applied stress.

A number of methods to predict the life time of solder joints undergoing thermomechanical loading are well reported in the literature [101-103]. As discussed in section 2.4, strain rate, temperature and creep have a significant effect on the behaviour of the solder, the stress levels to which it is expose and hence its lifetime.

One of the most widely used method in estimating lifetime of solder joint interconnect is modelled around that of the Coffin-Manson's formula which was developed for tensile specimens undergoing cyclic loading.

$$N_f = C_1(\Delta\varepsilon^{pl})^{C_2} \tag{2-1}$$

where $N_f$ is the number of cycles to failure, $\Delta\varepsilon^{pl}$ is the amplitude of plastic deformation, and $C_1$ and $C_2$ are the material parameters. An example of the use of this formula is the work by Syed [104] who used the accumulated creep strain per cycle to determine the lifetime of solder joints:

$$N_f = \left(C_3\varepsilon_{acc}\right)^{-1} \tag{2-2}$$

$N_f$ - number of cycles to failure,

$\varepsilon_{acc}$ - accumulated creep strain per cycle,

$C_3$ - $1/\varepsilon_f$ inverse of creep ductility.

There is a large body of work by Engelmaier [105, 106] in determining a formula that will predict the behaviour of solder interconnect in thermomechanical loading, the modified formula is

$$N_f = C_4 \left( \frac{\Delta \gamma^{pl}}{2\varepsilon_f} \right)^{1/C_5} \tag{2-3}$$

$$C_5 = C_6 + C_7 T_{ave} + C_8 \ln(1+f)$$

where $\Delta \gamma^{pl}$ is the average plastic shear strain amplitude, $T_{ave}$ is the average temperature in the solder joint, and f is the loading frequency. $C_4 - C_8$ and $\varepsilon_f$ are parameters that depend on the solder material, the geometry of the interconnection, and, probably, on the properties of the component and PWB. Another equation developed by the same author using the x% to signify failure in terms of force drop is:

$$N(x\%) = \frac{1}{2} \left( \frac{2\varepsilon_f'}{\Delta D} \right)^{-\frac{1}{C_9}} \left( \frac{\ln(1-0.01x)}{\ln 0.5} \right)^{\frac{1}{\beta}} \tag{2-4}$$

$\varepsilon_f'$ - fatigue ductility coefficient;

$\Delta D$ - the solder cyclic creep-fatigue damage;

$C_9$ - creep-fatigue ductility exponent;

$\beta$ - the shape parameter of the Weibull distribution.

N(x%) – Lifetime for x% of force drop.

A method similar to that of Engelmaier was proposed by Gromala et al [107], from their experimental result on solder lifetime. The experimental results on lifetime expectancy were presented in the form of the Weibull characteristic number of cycles to failure ($N_{63}$), which means a failure rate of 63.2%. The correlation to the CSED was based on a simple inverse power law. The pre-factor $C_{10}$ and the lifetime exponent $C_{11}$ were fitted in the study.

$$N_{63} = \frac{C_{10}}{(\Delta W_{CR})^{C_{11}}} \tag{2-5}$$

$$(\Delta W_{cr})_L = (CSED_{TC} - CSED_{TC-1})_L$$

with TC ( thermal cycling) and TC-I indicating the end and the beginning of the last TC simulated, respectively, while L stands for the number of the result extraction layer.

A different approach used by Darveaux [108] uses the principle of plastic work density calculated during a loading cycle and relates that to the lifetime of the solder joint. He proposed that the crack propagation path in an interconnection should be determined on the basis of stress analysis, and the average plastic work along this path would correlate with the lifetime of the joint. The average plastic work during a cycle, $\Delta w_{pl}^{e}$, is given by:

$$\Delta w_{pl}^{e} = \int \sigma_{ij} d\varepsilon_{ij}^{pl}$$

$$\Delta W_{pl} = \frac{\sum_{e} \Delta w_{pl}^{e} V^{e}}{\sum_{e} V^{e}} \tag{2-6}$$

where $\sigma_{ij}$ and $\varepsilon_{ij}^{pl}$ are the components of stress and plastic strain , $V^{e}$ is the volume of element e and $\Delta W_{pl}$ is the total plastic work.

The equations for the calculation of thermal cycles to crack initiation $N_{f0}$ and crack propagation rate per thermal cycle dL/dN.

$$N_{f0} = C_{12}\left(\Delta W_{pl}\right)^{C_{13}} \tag{2-7}$$

where $C_{12}$ and $C_{13}$ are the model parameters and the propagation rate is given by

$$\frac{dL}{dN} = C_{14}\left(\Delta W_{pl}\right)^{C_{15}} \tag{2-8}$$

where $C_{14}$ and $C_{15}$ are the model parameters. Finally, the time to failure is

$$N_f = N_{f0} + \frac{L_{cr}}{dL/dN} \tag{2-9}$$

where $L_{cr}$ is the length of the determined crack propagation path. The model parameters $C_{12}$ – $C_{15}$ depend on the solder material and the interconnection shape.

Most of the experimental lifetime equations discussed above can be used for a number of loading situations. Mainly for simulated and finite element analysis the method by Syed using accumulated plasticity is quite popular with a number of authors [109, 110]. The differences between the various authors are the values of the constant that embodies the difference in specimen size, type and loading profile used.

## 2.7 Inverse Modelling

One of the main emphasis of this work is the determination of elastic and creep material properties for SAC305 using inverse modelling techniques. Due to the volatility of material data in the literature, there is a need therefore for material datasets that are representative of the experimental procedure being simulated. The purpose of using inverse techniques is to be able to use discretisation methods, for example finite element analysis, to obtain material properties data that can be used to match simulations and experimental results. The accuracy of the finite element analysis is dependent on the model used, the loads and boundary conditions applied and also most importantly, the material properties. In general engineering application this is generally not a major concern but as discussed in section 1.4, when dealing with specimen in the micron scale, the determination of these material properties takes added significance. The use of bulk material datasets is inadequate and bulk solder joint sized samples do not produce reliable material data that can be used for all solder joints.

Inverse techniques are matured mathematical methods that can be used to find the solutions of problems in various fields and many techniques and theories have been developed for very specific or general applications in a number of engineering processes to determine loading conditions, force response, model shapes and material properties to reference a few. Inverse problems can generally be divided into two classes: parameter estimation and function estimation problems. The distinction between the two depends on the type of engineering problem being solved. Theoretical, function estimation has to deal with a large number of parameter with special emphasis on the minimization of the function and not just individual parameters. One will therefore notice that function estimation involve minimization of parameters as well. Gladwell [111] provided issues that will enable one to distinguish between parameter and function estimation problems even though these will not be unique solution regime. In contrast to parameter estimation, function estimation usually has the following characteristics: the number of parameters to describe a function is usually large — maybe in the hundreds or even thousands.

A number of authors used the inverse analysis technique to determine the parameters for a diffusion analysis experiment of multi-ion transport[112-114]. Massoni et al. [115] used this technique to analyse thermomechanical upsetting, whilst Li et al. [116] applied this method to multi parameter analysis. The application of the FEM has found widespread application in a number of fields such as manufacturing, heat transfer, vibrations, mechanics, etc. The finite element method has been an invaluable tool in performing inverse analysis because most engineering problems have no analytical solutions. Inverse FEA techniques can determine material properties using simulation and experimentally obtained data.

In [117], Moulton et al determined the passive myocardial properties using a p- FEM model of the heart with a non-linear optimization technique and strains measured with MRI imaging. A 2D nonlinear strain energy function was developed in testing the inverse algorithm. P-version FE formulation was used as: (1) the geometry of the heart can be captured accurately with relatively few elements using basis functions of higher polynomial degree, (2) the p-version FEM provides for rigorous control of the numerical error associated with the finite element approximation.

In [118], Kauer used tissue aspiration experiments in conjunction with the inverse FEM techniques that have been used to find the material parameters in materials governed by viscoelastic neo-Hookean and reduced Veronda-Westmann laws. This algorithm also employs the Levenberg- Marquardt algorithm [119] to find weighting factors corresponding to the spectrum of relaxation times of a material as long as the smallest and largest relaxation times are known. The large relaxation times are activated by specific deformation only if the time scale of material relaxation is at least as large as the largest relaxation time of the model. The smallest relaxation times determine the maximum time step for implicit finite element code. There are a number of challenges involved in inverse vibration problems. In most inverse vibration problems, we require an intuition regarding the transformation of the system variables to construct the inverse problem. Usually, the experiments for undamped systems can accurately predict data only for the lower portion of the required spectral data. Problem associated with the reconstruction of the system parameters from the matrices. This problem can be addressed by the construction of element stiffness and mass matrices and the identification of the system parameters from the element matrices. Standard inverse FEA fail if the domain is highly complex. Thus, a natural alternative is to solve such problems over small sub-domains. In [120, 121], the discretized system resulting from the principle of virtual work (i.e., the direct problem) is solved via a Newton-Raphson iterative procedure. Finite strain inflation tests can be performed on non-axisymmetric membranes by placing markers to measure the displacements. Sub-domain based techniques are proved to be not only more accurate at probing regional variations but also are computationally less expensive.

Inverse techniques can be used in problems where the loading conditions cannot be accurately defined. Very few FEA techniques consider the compliance at the joints in their analyses inherently assuming that the effect on the overall response is minimal. In [111], using full field strain measurements, the loads and compliance of the joints are found. The compliance at the joints were modelled as springs of some stiffness k attached to nodes connected to the joints. The Gauss Newton algorithm is used to minimize the least squares error between the strain and displacements values. It should be noted that the error function here only considers the strain value, but not its direction. Hence, it is not advised to perform inverse analysis using only strain values. In many cases, a part cannot be forged in a single operation [122]. Thus, the problem of design of the shapes of the preforming tools is posed. This can also be treated as an inverse problem by using techniques similar to those described earlier.

An inverse finite element method algorithm is developed by Keanini and Desai [123] for simultaneous solution of multi-dimensional solid-liquid phase boundaries and associated three-dimensional solid phase temperature fields [123]. Beginning with an initial guess, $P_i$, the inverse procedure iteratively alters P until the total error F between spatially discrete temperature measurements and corresponding calculated temperatures is minimised.

The inverse modelling procedure demonstrated by Husain et al [124] was of particular interest to this work.  Whilst investigating the behaviour of steel using experimental data generated from small punch tests they computed the uniaxial tensile test (true stress vs. true plastic strain curve) using inverse modelling techniques. They divided the load displacement curve from experiment into a number of linear segments and they matched a similar curve at a similar load using the finite element technique. A schematic of the technique is shown in figure 2-10.

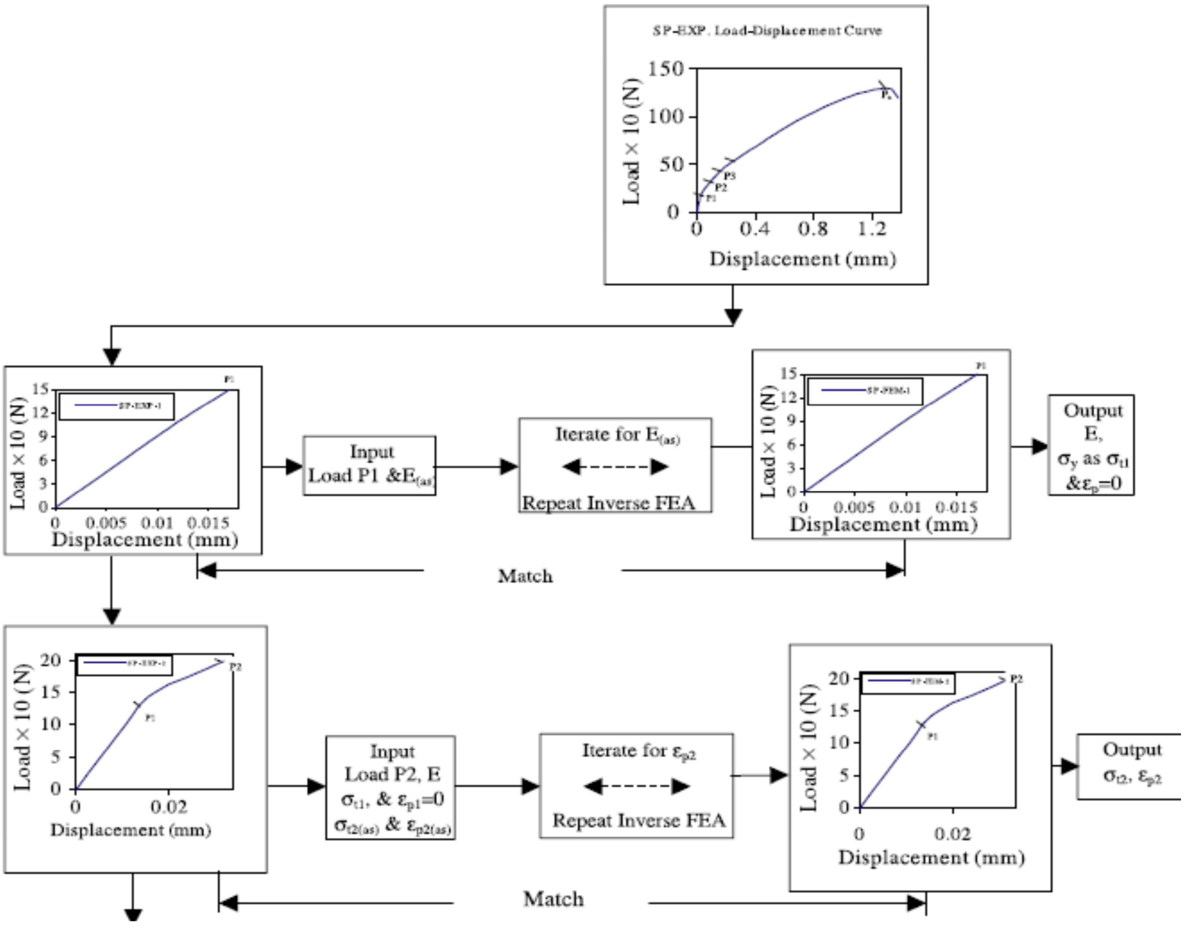

**Figure 2-10 Piecewise inverse modelling technique [124].**

## 2.8 Summary

A large body of published work detailing the behaviour of lead free solder in different loading conditions and regimes are available in literature. There are still a number of outstanding issues associated with lead free solder research. Although SnAgCu alloy is now widely used as the replacement of tin-lead solder, there is no agreement in the industry with regards to the exact composition of the alloy. All the variants touted in the literature have their respective strength and weaknesses and it is absolutely necessary that combination of elements have to be agreed on.

It is widely acknowledged and reported in the literature that there is a wide scatter in the material properties from different studies. As discussed above, this has to do in part with the large number of different material process parameters, process conditions and the quality of the solder joints. The large scatter in material properties is a source of concern, as it makes the analysis of the behaviour of solder joint unreliable.

A major limitation in the material data reported in the literature is that a large proportion of experimental and numerical simulation techniques used to determine the response of lead free solder joints uses equipment that they were not designed for. Of these, dynamic testing has had a primary role. Most of the testing performed makes use of off the shelf equipment that is generally unsuitable to conduct meaningful testing on very small solder specimens. The response of general purpose test equipment is mainly in the macro scale whilst the solder dimensions are in the micron scale. This therefore poses a serious limitation in interpreting the results obtained from these experiments for meaningful analysis.

The behaviour of the solder is also a major concern. Most of the published work in modelling the nonlinear response of the solder joint uses the Garofalo’s creep model. This model only models the secondary creep of the solder specimen and it neglects any hardening of the solder specimen that may occur. Using this model should therefore be seen as an approximation as the response of this model does not reflect the true behaviour of the lead free solder joints. To address this limitation of the Garofalo’s model, a more representative model initially used for modelling viscoplastic behaviour in metals is used to model the non-linear response of the solder joint. This model, Anand’s model, increased the complexity in determining the material parameters as there are nine parameters to be determined and there is a nonlinear relationship between the parameters that makes their determination more involved than that of the Garofalo’s model. The Anand’s model also required a large body of experimental work at different temperature and strain rates to make determination of the nine parameters possible.

In this work, in order to address the limitations of the existing research in the literature (of using bulk response equipment to perform micro-scale testing, for example), a new piece of equipment was designed with the specific aim of providing reliable response of solder in the micron scale. The design incorporates vibration fatigue testing, thermal cycling and combination of these. The equipment has a small footprint and can be controlled and monitored remotely. Simulation results of the equipment will be presented in the analysis to follow.

To determine the material parameters for the Anand’s creep model of lead free solder, use is made of inverse modelling techniques to match the force-displacement experimental data with that from simulations. The adverse effects that a spurious data can have on the entire analysis is minimised by using a small data sample and starting the analysis with a set of material parameters that matches closely with the experimental data obtained. This therefore reduces the reliance on a large body of experimental data and using inverse and optimisation techniques, the material parameters are thus determined.

# Chapter 3 Computer Simulation of Microelectronics Device and Test Equipment Using the Finite Element Method

## 3.1 Introduction

To perform the numerical analysis of the equipment design, multi-joint modelling and inverse analysis method, use is made of the finite element method. In the equipment design, it forms the primary analysis tool prior to fabrication of the individual components. In multi-joint analysis, it provides the basis for the comparison between the experimental response and its comparison to BGA package. During the inverse analysis, it provides a means of calculating the objective function from experimental result. As a result of the extensive use of the finite element technique in the simulation results, following is a brief discussion of the finite element formulation.

The Finite Element Method (FEM) is a mathematical approximation technique that has been used since the 1960's to solve initially large structural engineering problems. The rapid growth in computing power has accelerated the application and use of this method, and is now the tool of choice for structural analysis by mechanical, civil, biomechanical, and other engineers. It has been used to quantify design defects, fatigue, buckling, and crash simulation, and it can be used to identify failures that are caused by design deficiencies, materials defects, fabrication errors, and abusive use. It provides quantified results previously could only be obtained from metallurgical and mechanical testing. It provides excellent visual aids and animations that are easily understood.

The FEM procedure involves the breaking down of a domain into a number of subdomains referred to as elements and these elements are joined together at the nodes to form the FEM "mesh". This process of breaking the entire structure into elements is referred to as discretization. The reason for dividing the domain into elements is twofold: first, to represent the geometry of the domain numerically; and, second, to approximate the solution over each element of the mesh in order to better represent the solution over the entire domain. The behaviour of the physical property of interest is described in terms of algebraic equations within each element. The solution to the governing equations is closely approximated within each element, resulting in a number of equations that need to be solved for every element. The local response of the elements is used to provide the global response of the domain. Thus, the element equations cannot be solved in isolation to render the solution over each element. Instead, all the equations from all the elements over the entire structure need to be solved simultaneously. The rapid improvement in computer technology has made the FEM an attractive tool for both engineering practitioners and researchers in varied fields. In many applications of FEA, a computational domain contains a large number of elements and the number of governing equations is therefore huge. The solution of these large bodies of equations can only be solved using computers. It is worth noting that, as the structure is broken into a larger number of elements, a greater number of simultaneous equations need to be solved.

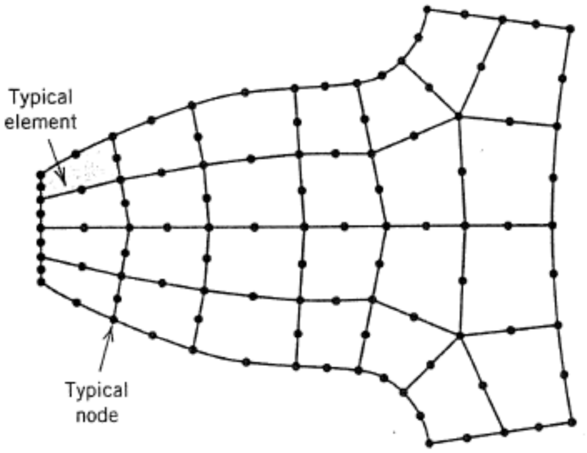

**Figure 3-1 An FEA mesh of a two-dimensional model of a gear tooth [125].**

## 3.2 Theory of Elasticity

Elasticity of solids and structure is a major area of structural engineering application and the FEM technique was initially applied to solving engineering problems in the elastic domain with considerable success. The results obtained in the early days of the usage of this technique provided the impetus for its applications in other branches of engineering.

Following is the finite element formulation for the solution of elastic problem using mathematical models.

Elastic materials return to their original shape when the external force causing the deformation is removed. The material can be classified as either linear or nonlinear. For a linear material, the stress and strain is linearly proportional to the applied force. The general equation of the constitutive equation for a linear material is $\sigma = E \cdot \varepsilon$ where $\sigma$, E and $\varepsilon$ are the stress, the modulus of elasticity (Young's modulus), and the strain.

For linear elastic solids, E is a constant. A solid is nonlinearly elastic if stress is not linearly related to strain but the material will return to its original configuration when load is removed and there is no energy lost in the system in the load-unload process.

## 3.3 Equilibrium Equations

To formulate the finite element method, we start off from the general dynamic equation and discretisation of the problem domain. The analysis and assumptions are discussed below.

The general governing equation of motion for solid can be written as:

$$[M]\{\ddot{u}\}+[C]\{\dot{u}\}+[K]\{u\}=\{F(t)\} \quad \textbf{(3-1)}$$

where $[M]$ is the mass matrix, $[C]$ is the damping matrix, $[K]$ is the stiffness matrix, $\{F(t)\}$ is the force vector and $\{u\}$ is the nodal displacement vector.

For a static analysis $\{\ddot{u}\}=\{0\}$ and $\{\dot{u}\}=\{0\}$, the above equation therefore reduces to

$$[K]\{u\}=\{F\} \quad \textbf{(3-2)}$$

The main task in the following analysis is to calculate the stiffness $[K]$ of the domain. There are a number of techniques in use to calculate $[K]$, and to demonstrate the concepts of the FEM the technique will be applied to an elastic example.

In 3D stress analysis, stress $\sigma$ and strain $\varepsilon$ are represented by vectors of six components:

$$\sigma = \left[\sigma_{xx}\ \sigma_{yy}\ \sigma_{zz}\ \tau_{xy}\ \tau_{yz}\ \tau_{zx}\right]^T \tag{3-3}$$

$$\varepsilon = \left[\varepsilon_{xx}\ \varepsilon_{yy}\ \varepsilon_{zz}\ \gamma_{xy}\ \gamma_{yz}\ \gamma_{zx}\right]^T \tag{3-4}$$

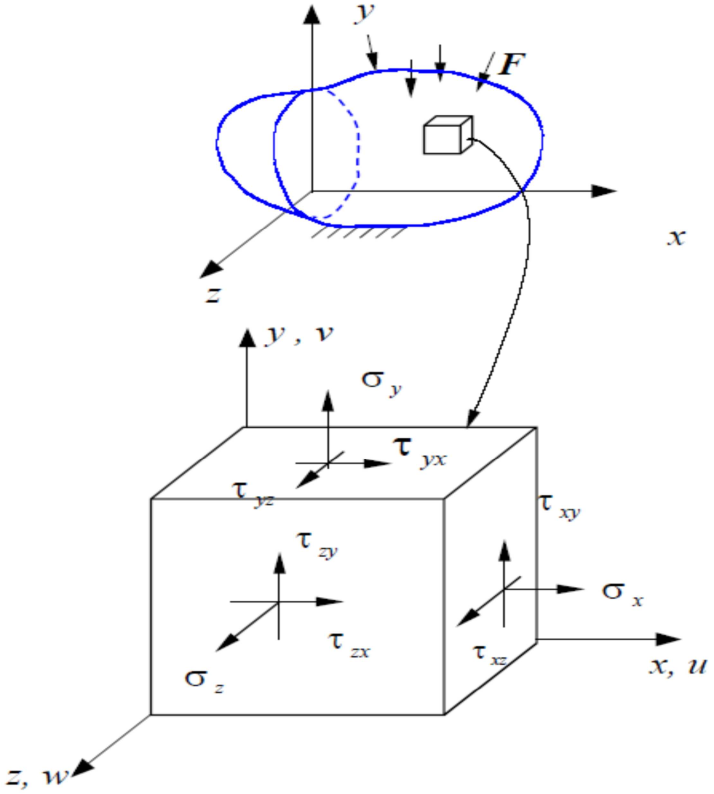

**Figure 3-2 Three dimensional stress state**

For an isotropic material, the stress strain relationship is given by:

$$\begin{Bmatrix} \sigma_x \\ \sigma_y \\ \sigma_z \\ \tau_{xy} \\ \tau_y z \\ \tau_{xz} \end{Bmatrix} = \frac{E}{(1+\nu)(1-2\nu)} \begin{bmatrix} 1-\nu & \nu & \nu & 0 & 0 & 0 \\ \nu & 1-\nu & \nu & 0 & 0 & 0 \\ \nu & \nu & 1-\nu & 0 & 0 & 0 \\ 0 & 0 & 0 & \frac{1-2\nu}{2} & 0 & 0 \\ 0 & 0 & 0 & 0 & \frac{1-2\nu}{2} & 0 \\ 0 & 0 & 0 & 0 & 0 & \frac{1-2\nu}{2} \end{bmatrix} \begin{Bmatrix} \varepsilon_x \\ \varepsilon_y \\ \varepsilon_z \\ \gamma_{xy} \\ \gamma_{yz} \\ \gamma_{xz} \end{Bmatrix} \tag{3-5}$$

or

$$\{\sigma\} = [D]\{\varepsilon\} \tag{3-6}$$

where *E*, ν and [*D*] are the Young's modulus, Poisson's ratio and material matrix respectively. This is the standard matrix form of the constitutive relationship for an isotropic linear elastic material.

The displacement profile is represented as:

$$u = \begin{Bmatrix} u(x, y, z) \\ v(x, y, z) \\ w(x, y, z) \end{Bmatrix} = \begin{Bmatrix} u_1 \\ u_2 \\ u_3 \end{Bmatrix} \tag{3-7}$$

For small strains and small rotations, the strains are defined as,

$$\begin{gathered} \varepsilon_x = \varepsilon_{xx} = \frac{\partial u}{\partial x},\ \varepsilon_y = \varepsilon_{yy} = \frac{\partial v}{\partial y},\ \varepsilon_z = \varepsilon_{yy} = \frac{\partial w}{\partial z} \\ \gamma_{xy} = \frac{\partial u}{\partial y} + \frac{\partial v}{\partial x},\ \gamma_{yz} = \frac{\partial v}{\partial z} + \frac{\partial w}{\partial y},\ \gamma_{xz} = \frac{\partial u}{\partial z} + \frac{\partial w}{\partial x}, \end{gathered} \tag{3-8}$$

or in tensorial notation

$$\varepsilon_{ij} = \frac{1}{2}\left(u_{i,j} + u_{j,i}\right) \tag{3-9}$$

where $u_{i,j} = \frac{\partial u_i}{\partial x_j}$, *i* and *j* are dummy variables.

In matrix form,

$$\begin{bmatrix} \varepsilon_x \\ \varepsilon_y \\ \varepsilon_z \\ \gamma_{xy} \\ \gamma_{xz} \\ \gamma_{yz} \end{bmatrix} = \begin{bmatrix} \frac{\partial}{\partial x} & 0 & 0 \\ 0 & \frac{\partial}{\partial x} & 0 \\ 0 & 0 & \frac{\partial}{\partial x} \\ \frac{\partial}{\partial y} & \frac{\partial}{\partial x} & 0 \\ \frac{\partial}{\partial z} & 0 & \frac{\partial}{\partial x} \\ 0 & \frac{\partial}{\partial z} & \frac{\partial}{\partial y} \end{bmatrix} \begin{bmatrix} u \\ v \\ w \end{bmatrix} \tag{3-10}$$

or

$$\{\varepsilon\} = [L]\{u\} \tag{3-11}$$

From elasticity theory, the stresses in the structure must satisfy the following equilibrium equation,

$$\begin{aligned} \frac{\partial \sigma_{xx}}{\partial x} + \frac{\partial \tau_{xy}}{\partial y} + \frac{\partial \tau_{xz}}{\partial z} + f_x = 0 \\ \frac{\partial \tau_{xy}}{\partial x} + \frac{\partial \sigma_{yy}}{\partial y} + \frac{\partial \tau_{yz}}{\partial z} + f_y = 0 \\ \frac{\partial \tau_{xz}}{\partial x} + \frac{\partial \tau_{yz}}{\partial y} + \frac{\partial \sigma_{zz}}{\partial z} + f_z = 0 \end{aligned} \tag{3-12}$$

or

$$\sigma_{ij,j} + f_i = 0 \tag{3-13}$$

where $\sigma_{ii}$ and $f_i$ are the components of stress and body forces acting in direction i. Einstein notation is used in equation 3-13. For an isotropic material homogeneous material undergoing small strain, the stress is related to the elastic strains through the linear elastic constitutive equation.

Boundary conditions are incorporated into the finite element procedure by introducing the surface integrals into the formulation for control volume whose faces lie on the boundary of the domain.

The specified displacement

$$u_i = \bar{u}_i, \qquad \text{on } \Gamma_u \tag{3-14}$$

The specified traction

$$\begin{aligned} t_i &= \bar{t}_i, \qquad \text{on } \Gamma_\sigma \\ t_i &= \sigma_{ij} n_j \end{aligned} \tag{3-15}$$

where $\bar{t}_i$ and $\bar{u}_i$ are the element's traction and displacement on the surface.

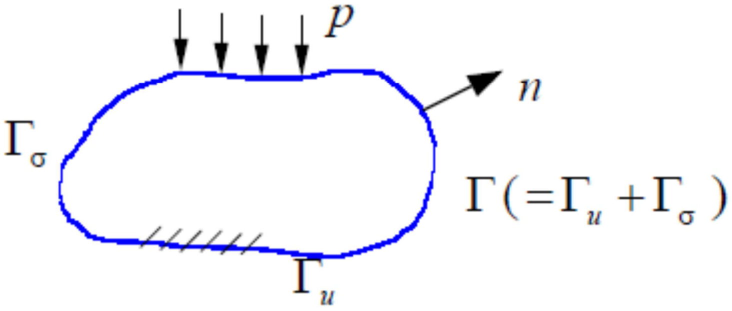

**Figure 3-3 Boundary conditions on a surface**

Solving equations (3-6), (3-8) and (3-13) using the boundary conditions as defined in equation (3-15) provides the stress, strain and displacement fields for the 3-D problem. Getting a solution analytically is usually not possible.

## 3.4 Finite Element Method Formulation

The basic procedure in the isoparametric finite element formulation is to express the element coordinates and element displacements in the form of interpolations using the natural coordinate system of the element. This has made possible a large number of nonrectangular elements to be used, elements with curved sides, ‘infinite’ elements for unbounded media and singularity elements for fracture mechanics [125].This coordinate system, is one-, two- or three-dimensional, depending on the type of element used.

In the isoparametric formulation the elements displacements are interpolated as follows:

$$u = \sum_{i=1}^{n} N_i u_i$$
$$v = \sum_{i=1}^{n} N_i v_i \qquad \textbf{(3-16)}$$
$$w = \sum_{i=1}^{n} N_i w_i$$

where $N_i$ are the shape functions.

In matrix form

$$\begin{Bmatrix} u \\ v \\ w \end{Bmatrix} = \begin{bmatrix} N_1 & 0 & 0 & N_2 & 0 & 0 & --- \\ 0 & N_1 & 0 & 0 & N_2 & 0 & --- \\ 0 & 0 & N_1 & 0 & 0 & N_2 & --- \end{bmatrix} \begin{Bmatrix} u_1 \\ v_1 \\ w_1 \\ u_2 \\ v_2 \\ w_2 \\ - \\ - \\ - \end{Bmatrix} \qquad \textbf{(3-17)}$$

or

$$\{u\} = [N]\{d\} \qquad \textbf{(3-18)}$$

where u, v, and w are the displacements at any point in an element and $u_i$, $v_i$, and $w_i$ where i=1………n, are the displacements at the nodes of the element and n is the number of nodes in an element.

### 3.4.1 Element Formulation

The choice of elements in a finite element analysis is a very important step in generating accurate results. Below are two typical 3-D solid elements. The first is a linear element whereas the second is a higher order element.

Hexahedron (Brick)

Linear (8 nodes)

Quadratic (20 nodes)

**Figure 3-4 Element types in finite element analysis**

In FEM, the natural coordinate system is convenient. In this system $\xi, \eta, \zeta$ represent the coordinates, and element boundaries are always defined by $\xi = \pm 1$, $\eta = \pm 1$ and $\zeta = \pm 1$ regardless of the shape or physical size of the elements or its orientation in the global coordinates (Figure 3-5).

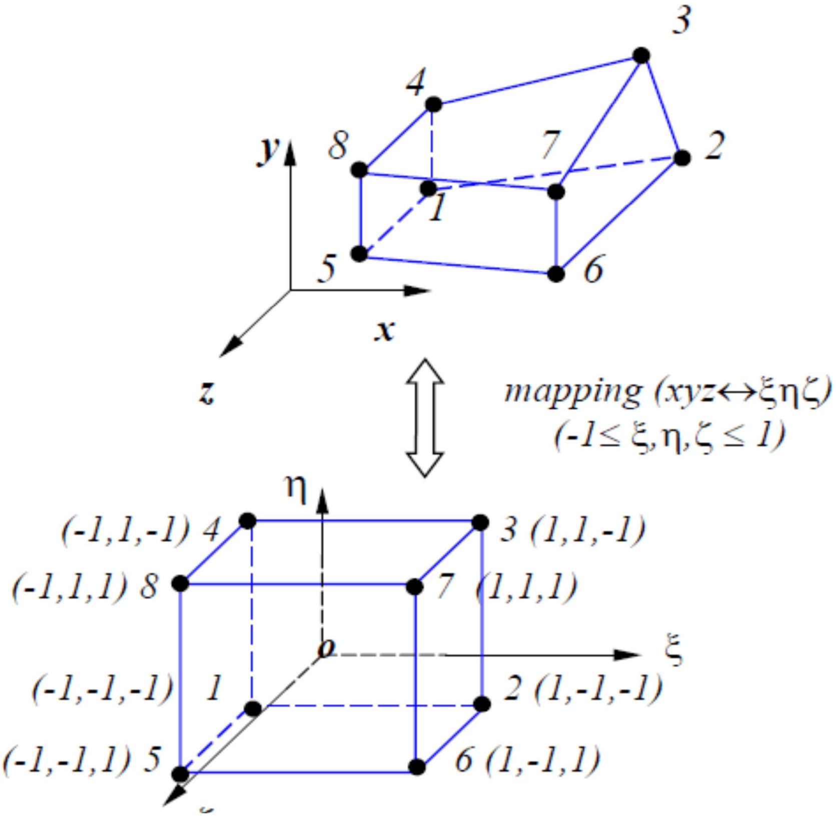

**Figure 3-5 Element mapping**

To be able to evaluate the stiffness matrix of an element, we need to calculate the strain-displacement transformation matrix. The element strains are obtained in terms of derivatives of element displacement with respect to the local coordinate system using (ξ, η, ζ), we need to relate x, y and z derivatives to ξ, η, ζ derivatives.

From equation 3-19:

$$x = f_1(\xi,\eta,\zeta); \qquad y = f_2(\xi,\eta,\zeta); \qquad z = f_3(\xi,\eta,\zeta); \qquad \textbf{(3-19)}$$

the inverse relationship can therefore be derived as:

$$\xi = f_4(x,y,z); \qquad \eta = f_5(x,y,z); \qquad \zeta = f_6(x,y,z); \qquad \textbf{(3-20)}$$

The displacement field in the element is given by:

$$u=\sum_{i=1}^{8}N_iu_i,\quad v=\sum_{i=1}^{8}N_iv_i,\quad w=\sum_{i=1}^{8}N_iw_i \tag{3-21}$$

The shape functions are defined as follows;

$$\begin{aligned}
N_1(\xi,\eta,\zeta)&=\frac{1}{8}(1-\xi)(1-\eta)(1-\zeta)\\
N_2(\xi,\eta,\zeta)&=\frac{1}{8}(1+\xi)(1-\eta)(1-\zeta)\\
N_3(\xi,\eta,\zeta)&=\frac{1}{8}(1+\xi)(1+\eta)(1-\zeta)\\
\vdots\qquad\vdots\qquad&\vdots\qquad\vdots\qquad\vdots\qquad\vdots\\
N_8(\xi,\eta,\zeta)&=\frac{1}{8}(1-\xi)(1+\eta)(1+\zeta)
\end{aligned} \tag{3-22}$$

The fundamental property of the shape functions $N_\mathrm{i}$ is that its value is unity at node i and zeros at all other nodes. This property can be expressed using the Kronecker delta as:

$$\begin{aligned}
&N_i\left(\xi_j,\eta_j,\zeta_j\right)=\delta_{ij},\quad \text{i, j=1, 2, .........8}\\
&\sum_{i=1}^{8}N_i(\xi,\eta,\zeta)=1
\end{aligned} \tag{3-23}$$

Considering the above three-dimensional element, the coordinate transformations (mappings) for isoparametric elements are:

$$\begin{aligned}
x&=\sum_{i=1}^{8}N_ix_i\\
y&=\sum_{i=1}^{8}N_iy_i\\
z&=\sum_{i=1}^{8}N_iz_i
\end{aligned} \tag{3-24}$$

where x, y, z are coordinates at any point within the element, and $x_i$, $y_i$, $z_i$, (i = 1………n) are the coordinates of the n element nodes. The shape functions $N_\mathrm{i}$ are defined in the natural coordinate system of the element.

Using the chain rule, the partial differentials of variable *u* with respect to x, y and z are given by;

$$\begin{aligned}
\frac{\partial u}{\partial x} &= \frac{\partial u}{\partial \xi}\frac{\partial \xi}{\partial x} + \frac{\partial u}{\partial \eta}\frac{\partial \eta}{\partial x} + \frac{\partial u}{\partial \zeta}\frac{\partial \zeta}{\partial x} \\
\frac{\partial u}{\partial y} &= \frac{\partial u}{\partial \xi}\frac{\partial \xi}{\partial y} + \frac{\partial u}{\partial \eta}\frac{\partial \eta}{\partial y} + \frac{\partial}{\partial \zeta}\frac{\partial \zeta}{\partial y} \\
\frac{\partial u}{\partial z} &= \frac{\partial u}{\partial \xi}\frac{\partial \xi}{\partial z} + \frac{\partial u}{\partial \eta}\frac{\partial \eta}{\partial z} + \frac{\partial u}{\partial \zeta}\frac{\partial \zeta}{\partial z}
\end{aligned} \qquad \textbf{(3-25)}$$

Also using the chain rule to derive the explicit inverse relationship, we have from equation 3-25

$$\begin{bmatrix} \frac{\partial u}{\partial \xi} \\ \frac{\partial u}{\partial \eta} \\ \frac{\partial u}{\partial \zeta} \end{bmatrix} = \begin{bmatrix} \frac{\partial x}{\partial \xi} & \frac{\partial y}{\partial \xi} & \frac{\partial z}{\partial \xi} \\ \frac{\partial x}{\partial \eta} & \frac{\partial y}{\partial \eta} & \frac{\partial z}{\partial \eta} \\ \frac{\partial x}{\partial \zeta} & \frac{\partial y}{\partial \zeta} & \frac{\partial z}{\partial \zeta} \end{bmatrix} \begin{bmatrix} \frac{\partial u}{\partial x} \\ \frac{\partial u}{\partial y} \\ \frac{\partial u}{\partial z} \end{bmatrix} \qquad \textbf{(3-26)}$$

The Jacobian matrix is defined as;

$$J = \begin{bmatrix} \frac{\partial x}{\partial \xi} & \frac{\partial y}{\partial \xi} & \frac{\partial z}{\partial \xi} \\ \frac{\partial x}{\partial \eta} & \frac{\partial y}{\partial \eta} & \frac{\partial z}{\partial \eta} \\ \frac{\partial x}{\partial \zeta} & \frac{\partial y}{\partial \zeta} & \frac{\partial z}{\partial \zeta} \end{bmatrix} \qquad \textbf{(3-27)}$$

$$\begin{bmatrix} \frac{\partial u}{\partial x} \\ \frac{\partial u}{\partial y} \\ \frac{\partial u}{\partial z} \end{bmatrix} = J^{-1} \begin{bmatrix} \frac{\partial u}{\partial \xi} \\ \frac{\partial u}{\partial \eta} \\ \frac{\partial u}{\partial \zeta} \end{bmatrix} \qquad \textbf{(3-28)}$$

The Jacobian operator relates the derivatives of the natural coordinates to the derivatives of the local coordinates. This therefore requires that the inverse of the Jacobian exists.

The governing equilibrium equations are integrated over each element. The integrals (volume for three dimensional and area for two-dimensional analysis) can be approximated using numerical integration techniques such as the Gauss quadrature. The discretised equations are solved by using the reference elements which represent the mesh elements in a local coordinate system. The stiffness matrix is calculated by considering the strain energy stored in an element. The strain energy *U* is given by

$$\begin{aligned} U &= \frac{1}{2}\int_v \{\sigma^T\}\{\varepsilon\}dV = \frac{1}{2}\int_v \left(\sigma_x\varepsilon_x + \sigma_y\varepsilon_y + \sigma_z\varepsilon_z + \tau_{xy}\gamma_{xy} + \tau_{yz}\gamma_{yz} + \tau_{xz}\gamma_{xz}\right)dV \\ &= \frac{1}{2}\int_v \left([D]\{\varepsilon\}\right)^T\{\varepsilon\}dV = \frac{1}{2}\int_v \{\varepsilon^T\}[D]\{\varepsilon\}dV \end{aligned} \tag{3-29}$$

substituting $\{\varepsilon\}$=[B]{d}

$$\begin{aligned} &= \frac{1}{2}\{d^T\}\left[\int_v [B^T][D][B]dV\right]\{d\} \\ &= \frac{1}{2}\{d^T\}[k]\{d\} \end{aligned} \tag{3-30}$$

where [*B*] the strain-displacement matrix and {u} the vector of nodal displacements are known for each element once the global finite element equation is solved.

From the above the general formula for the element stiffness matrix is given by,

$$[k] = \int_v [B^T][D][B]dV \tag{3-31}$$

d$V$ can be calculated in the natural coordinates,

$$\begin{aligned} &dV = (\det[J])d\xi d\eta d\zeta \\ &k \text{ is therefore} \\ &[\mathrm{k}] = \int_{-1}^{1}\int_{-1}^{1}\int_{-1}^{1}[B^T][D][B]\left(\det[J]\right)d\xi d\eta d\zeta \end{aligned} \tag{3-32}$$

The stiffness matrix is dependent on the [*B*] matrix which in turn is dependent on the shape functions. The stiffness matrix is symmetric since [*D*] is symmetric. This therefore means that the quality of finite element representing the behaviour of the structure is determined entirely by the choice of shape functions.

### 3.4.2 Stress Calculation

The stress in an element is determined by the following relation:

$$\begin{Bmatrix} \sigma_x \\ \sigma_y \\ \sigma_z \\ \tau_{xy} \\ \tau_{yz} \\ \tau_{xz} \end{Bmatrix} = [D] \begin{Bmatrix} \varepsilon_x \\ \varepsilon_y \\ \varepsilon_z \\ \gamma_{xy} \\ \gamma_{yz} \\ \gamma_{xz} \end{Bmatrix} = [D][B]\{d\} \qquad \textbf{(3-33)}$$

## 3.5 Dynamic Analysis

When a load is applied to a structure, it may deform, rotate or move in response to the load. If the loading is cyclical and the frequency is less than about a third of the structure's lowest natural frequency of vibration, the problem can be classified as static and analysed by the method described above. If the load has a higher frequency, varies randomly or is applied suddenly, then the variation of displacements with time is so rapid that inertial effects cannot be ignored; dynamic analysis needs to be used [126]. As described above, the first task in the static analysis was to calculate the stiffness matrix but in this case we also need a mass matrix and a damping matrix. This therefore means modelling of a dynamic system will include some aspect of static modelling plus governing equation terms for structural acceleration and friction, which are derivatives of displacements with respect to time [126].

### 3.5.1 Mass Matrix

In static analysis the inertial effect of the system is assumed to be negligible, this is not the case with dynamic analysis where the inertia effects are very important. Therefore, to perform a dynamic and vibration finite element analysis, a mass matrix is needed to pair with the stiffness matrix. As a general rule, the construction of the global mass matrix [M] largely parallels that of the global stiffness matrix [K]. Mass matrices for individual elements are formed in local coordinates, transformed to global, and merged into the master mass matrix following exactly the same techniques used for [K]. In practical terms, the assemblers for [K] and [M] can be made identical. This procedural uniformity is one of the great assets of the direct stiffness method.

A notable difference with the stiffness matrix is the possibility of using a diagonal mass matrix based on direct lumping. A master diagonal mass matrix can be stored simply as a vector. If all entries are non-negative, it is easily inverted, since the inverse of a diagonal matrix is also diagonal [127, 128].

There are several methods used in the construction of the mass matrix of the individual elements. These can be categorized into three groups: direct mass lumping, variational mass lumping, and template mass lumping. The last group is more general in that it includes all others. The first two techniques are by far the most popular in the FEM literature, and variants of these methods have been implemented in all general purpose codes. Following is a discussion of the formulation of direct mass lumping.

The general equation of motion for the whole is given in equation.3-1. To obtain the consistent mass matrix, we start by considering the kinetic energy $E_k$ of the system:

$$\begin{aligned} E_k &= \frac{1}{2}\int_v \rho \dot{u}^2 dV = \frac{1}{2}\int_v \rho(\dot{u})^T \dot{u} dV \\ &= \frac{1}{2}\int_v \rho\left(N\dot{d}\right)^T\left(N\dot{d}\right)dV \\ &= \frac{1}{2}\dot{d}^T \underbrace{\int_v \rho N^T N dV}_{m}\,\dot{d} \end{aligned} \tag{3-34}$$

*Therefore*

$$[M] = \int_v \rho N^T N dV \tag{3-35}$$

where the shape function $N$ is the same as that used in the displacement field.

A key motivation for the use of the direct lumping method is that, a diagonal mass matrix may offer computational and storage advantages in certain simulations where, for example, explicit time integration is carried out. Furthermore, direct lumping covers naturally the case where concentrated (point) masses are a natural part of model building [129]. Knowing the mass matrix [$M$], the damping matrix [$C$], the stiffness matrix [$K$] and the forcing vector {$F$(t)} the displacement and differentials thereof can be calculated. The use of FEM to carry out modal, harmonic and transient analysis of a structure will be described in the following section.

### 3.5.2 Modal Analysis

Modal analysis is used to determine the natural frequencies and mode shapes of the system. The natural frequencies and mode shapes are important parameters in the design for dynamic loading conditions and are inherent properties of the system that can be determined analytically. They are also required if one wants to perform a spectrum analysis or a mode superposition, harmonic or transient analysis. The resonant frequencies and mode shapes are important as they determine the stability of the system. If the frequency of the model is close to or at the resonant frequency then you are certain that the system will undergo uncontrolled non-linear displacement that will ultimately lead to the failure of the structure.

There are a number of benefits associated with this analysis: it allows the design to avoid resonant vibrations or to vibrate at a specified frequency, gives engineers an idea of how the design will respond to different types of dynamic loads and helps in calculating solution controls (time steps, etc.) for other dynamic analyses.

Starting from the general equation of motion, equation 3-1, ignoring damping and assuming free vibration, i.e {F(t)} = 0 and [C] = 0, the equation becomes:

$$[M]\{\ddot{u}\}+[K]\{u\}=\{0\} \tag{3-36}$$

Assuming that the displacement vary harmonically with time everywhere in the structure, then

$$\begin{aligned} u(t) &= \bar{u}\sin(\omega t), \\ \dot{u}(t) &= \omega\bar{u}\sin(\omega t), \\ \ddot{u}(t) &= -\omega^2\bar{u}\sin(\omega t) \end{aligned} \tag{3-37}$$

where $\bar{u}$ are the vectors of nodal displacement amplitudes.

The above equations now yield;

$$\left([K]-\omega^2[M]\right)\bar{u}=0 \tag{3-38}$$

The linear equation is homogeneous and solving it is what is generally referred to as the eigenvalue problem (EVP).

For the non-trivial solution: $u \neq 0$ the determinant of the coefficient matrix must then be zero, i.e.:

$$\left|[K]-\omega^2[M]\right|=0 \tag{3-39}$$

This is an n-th order polynomial of $\omega^2$, from which we can find n solutions (roots) or eigenvalues $\omega_i$ and these are referred to as the natural (or characteristic) frequencies of the structure.

To calculate the eigenvectors, each value of $\omega_i$ is substituted into equation (3-39) and this gives one solution or eigenvector;

$$\left([K]-\omega^2[M]\right)\bar{u}=0 \qquad \textbf{(3-40)}$$

$\bar{u}_i$ (i=1, 2, 3……n) are the natural modes or mode shapes.

Once the modal analysis has been performed, harmonic, transient, or spectrum analysis may be carried out if necessary.

### 3.5.3 Harmonic Analysis

The harmonic response analysis is a technique that can be used to determine the steady-state response of a linear structure to loads that vary sinusoidally (harmonically) with time. Any sustained cyclic load will produce a sustained cyclic response (a harmonic response) in a structural system. The idea is to calculate the structure's response at several frequencies and obtain a graph of certain response quantity (usually displacements) versus frequency. "Peak" responses are then identified on the graph and stresses reviewed at those peak frequencies. Harmonic response analysis allows for prediction of the sustained dynamic behaviour of the structures being modelled, thus enabling verification whether or not the designs will successfully overcome resonance, fatigue, and other harmful effects of forced vibrations.

### 3.5.4 Transient Analysis

Transient dynamic analysis (sometimes called time-history analysis) is a technique used to determine the dynamic response of a structure under the action of any general time-dependent loads. This type of analysis is used to determine the time-varying displacements, strains, stresses, and forces in a structure as it responds to any combination of static, transient, and harmonic loads. The time scale of the loading is such that the inertia or damping effects are considered to be important. If the inertia and damping effects are not important, you might be able to use a static analysis instead.

There are generally two transient dynamics solution methods in literature: modal superposition and direct integration. The modal superposition method uses free vibrations mode shapes to uncouple the equation of motion. The equations are now in terms of a new variable called the modal coordinates. The modal coordinate solutions are obtained by solving the equations independently. A superposition of the modal coordinates then gives solution to the original equation. The direct integration technique is so termed because no special transformation techniques are required.

For transient analysis the general equations of motion are solved directly and equation (3-1) can be written as

$$[M]\{\ddot{u}_n\}+[c]\{\dot{u}_n\}+[K]\{u_n\}=\{f_n\} \qquad \textbf{(3-41)}$$

where n is the time step number and $u_n$ is the nodal displacement vector at time step n. The time increment is $\Delta t = t_{n-1} - t_n$ n = 0,1,2,3, $\cdots\cdots$.

## 3.6 Solution Methods

There two methods that are often used to solve equation 3-42: the central difference method and the Newmark method.

### 3.6.1 The Central Difference Method

The basis of the finite difference method is a set of finite difference formula for the approximate first and second derivatives centred at instant n.

By definition:

$$\begin{aligned}\{\dot{u}_n\} &= \frac{1}{2\Delta t}\left(\{u_{n+1}\}-\{u_{n-1}\}\right)\\ \{\ddot{u}_n\} &= \frac{1}{2\left(\Delta t\right)^2}\left(\{u_{n+1}\}-2\{u_n\}+\ \{u_{n-1}\}\right)\end{aligned} \qquad \textbf{(3-42)}$$

After substituting for $\{\ddot{u}_n\}$ and $\{\dot{u}_n\}$, the governing equation becomes

$$[M]\left\{\frac{1}{2\left(\Delta t\right)^2}\left(\{u_{n+1}\}-2\{u_n\}+\ \{u_{n-1}\}\right)\right\}+[C]\left\{\frac{1}{2\Delta t}\left(\{u_{n+1}\}-\{u_{n-1}\}\right)\right\}+[K]\{u_n\}=\{f_n\} \qquad \textbf{(3-43)}$$

which can be written as

$$
\begin{aligned}
&[A]\{u\}_{n+1} = \{F(t)\} \\
&\textit{where} \\
&[A] = \frac{1}{(\Delta t)^2}[M] + \frac{1}{2\Delta t}[C] \\
&\{F(t)\} = \{f_n\} - \left[[K] - \frac{2}{(\Delta t)^2}[M]\right]\{u_n\} - \left[\frac{1}{(\Delta t)^2}[M] - \frac{1}{2\Delta t}[C]\right]\{u_{n-1}\}
\end{aligned}
\qquad \textbf{(3-44)}
$$

$u_{n+1}$ is calculated from $u_n$ and $u_{n-1}$ the solution progresses step by step until the end of the simulation time is reached.

The central difference method is conditionally stable, if $\Delta t$ is very large, the computed displacement will grow beyond bounds and the result will be inaccurate or diverge. To guarantee numerical stability the following conditions must hold:

$$
\begin{aligned}
&\Delta t < \Delta \mathrm{t}_{cr} \quad \text{where} \quad \Delta \mathrm{t}_{cr} = \frac{2}{\omega_{\max}} = \frac{T_{\min}}{\pi} \\
&T_{\min} = \frac{2\pi}{\omega_{\max}}
\end{aligned}
\qquad \textbf{(3-45)}
$$

where $\omega_{\max}$ is the largest undamped natural frequency of the system [126, 130]

### 3.6.2 Newmark Method

This method is based on the following approximations [128, 132]:

$$
\begin{aligned}
&\{u_{n+1}\} \approx \{u_n\} + \Delta t\{\dot{u}_n\} + \frac{(\Delta t)^2}{2}\left[(1-2\beta)\{\ddot{u}_n\} + 2\beta\{\ddot{u}_{n+1}\}\right] \qquad \textbf{(3-46)} \\
&\{u_{n+1}\} \approx \{u_n\} + \Delta t\left[(1-\gamma)\{\ddot{u}_n\} + \gamma\{\ddot{u}_{n+1}\}\right]
\end{aligned}
$$

$$
\{u_{n+1}\} \approx \{u_n\} + \Delta t\{\dot{u}_n\} + \frac{(\Delta t)^2}{2}\left[(1-2\beta)\{\ddot{u}_n\} + 2\beta\{\ddot{u}_{n+1}\}\right] \qquad \textbf{(3-47)}
$$

where β and γ are constants that can be chosen by the analysts. Substituting in the equation of motion

$$[M]\frac{1}{(1-2\beta)}\left\{\frac{2}{(\Delta t)^2}\left(\{u_{n+1}\}-\{u_n\}-\Delta t\{\dot{u}_n\}\right)-2\beta\{\ddot{u}_{n+1}\}\right\}+ \\ [C]\left\{\{\dot{u}_{n+1}\}-\Delta t\left[(1-\gamma)\{\ddot{u}_n\}-\gamma\{\ddot{u}_{n+1}\}\right]\right\}+[K]\{u_n\}=\{f_n\} \quad \textbf{(3-48)}$$

This can be written in the form

$$[A]\{u_{n+1}\}=\{f_n\} \quad \textbf{(3-49)}$$

where

$$[A]= [\mathrm{K}] + \frac{\gamma}{\beta\Delta t}[C] + \frac{1}{\beta(\Delta t)^2}[M] \\ f_n = \mathrm{f}(\mathrm{f}_{n+1},\ \gamma,\ \beta,\ \Delta t,\ C,\ M,\ u_n,\ \dot{u}_n,\ \ddot{u}_n) \quad \textbf{(3-50)}$$

This method is unconditionally stable if

$$2\beta \ \geq\ \gamma\ \geq\ \frac{1}{2} \quad \textbf{(3-51)}$$

## 3.7 Nonlinear Elasto-Viscoplasticity

The finite element method has been applied to the solution of plasticity with a high degree of success. The numerical procedure for the solution of elastic-viscoplastic material behaviour is discussed in the following section. The fundamental assumption of elasto-viscoplasticity is that the total deformation can be separated into its elastic and viscoplastic parts [133,134].

The total strain can be expressed as

$$\varepsilon=\varepsilon^e+\varepsilon^p$$

total strain rate is given by **(3-52)**

$$\dot{\varepsilon}=\dot{\varepsilon}^e+\dot{\varepsilon}^p$$

where $\dot{\varepsilon}^e$ is the elastic strain rate and $\dot{\varepsilon}^p$ is the viscoplastic strain rate. The elastic strain rate is related to the stress through Hooke's law

$$\{\sigma\} = [D]\{\varepsilon\} \tag{3-53}$$

Therefore

$$[\dot{\sigma}] = [D]\{\dot{\varepsilon}\} \tag{3-54}$$

The constitutive equation for the viscoplastic model can be written as;

$$\dot{\varepsilon} = \left\langle \Theta\left(F\right)\right\rangle \gamma \frac{\partial Q}{\partial \sigma} \tag{3-55}$$

where

$$F = \mathrm{f}\left(\sigma_{ij} - C_y\right)$$

$Q$ is the plastic potential, the common case of associated plasticity correspond to taking $Q$=$F$, $C_y$ is the yield stress and $\gamma$ is the material property fluidity. A widespread choice of $\Theta(F)$ is $\Theta(F) = \left(F/C_y\right)^N$ for some prescribed constant $N$.

For elastic solid we have;

$$\int_\Omega [B_i^T]\{\sigma\} d\Omega + \{f_i\} = 0 \qquad \text{i = 1……}n \tag{3-56}$$

where $f_i$ contains the body forces and the surface integral of the tractions. The relationship between the total strain rate and displacement field rate is given by

$$\{\dot{\varepsilon}\} = \sum_{i=1}^{n} [B_i]\{\dot{u}_i\} \tag{3-57}$$

where the total strain rate is known since $[B_i], \{u_i\}$ and $[D]$ are known from the elastic analysis.

The vector equation for the displacement field cannot be generated by eliminating the stress and strain quantities in an elasto-viscoplasticity analysis as the total strain rate $\dot{\varepsilon}$ introduces nonlinearities into the solution procedure. By proper discretisation, an iterative process can be derived where a linear system is solved with respect to the displacement field. In its simplest form, the linear system appearing in this numerical method has a coefficient matrix identical to that of the elasticity problem.

Combining equation 3-52, 3-54 and 3-57 yields

$$\{\dot{\sigma}\}-[D]\left(\sum_{i=1}^{n}[B_i]\{\dot{u}_i\}-\{\dot{\varepsilon}^p\}\right)=0 \qquad \textbf{(3-58)}$$

Since $\{\dot{\varepsilon}^p\}$ depends nonlinearly on {σ}, it cannot be eliminated but must work with essentially two types of spatially discrete equations governing {σ} and $\{u_i\}$ using equation 3-56 and 3-58. Equation 3-58 can be approximated using the θ-rule [135, 136] and ANSYS® uses the Newton-Raphson iterative method to solve the equation.

## 3.8 Discussion

The analysis and simulation of the proposed equipment, multi-joint modelling, and inverse finite element analysis makes uses of structural and material nonlinearity techniques as described and programmed in ANSYS®. Use is made of ANSYS® since it is a general purpose finite element modelling package for solving a wide variety of mechanical problems. These problems include static, dynamic, structural analysis (linear and nonlinear), heat transfer, electromagnetic and fluid-structure interaction. It is widely applied in electronic packaging research to simulate the response of a physical system to a wide variety of loading. All of the nonlinear material models used in the following work are already programmed in the software thereby providing direct applications of these models and provide detailed solutions. ANSYS® employs the Newton-Raphson approach to solve problems that are nonlinear in formulation. The loads defined during the analysis are typically applied over several load steps. During the analysis, the out of balance load vector is evaluated (which is the difference between the restoring forces, the loads corresponding to the element stresses, and the applied loads) using the Newton-Raphson method. ANSYS® then performs the solution using the out of balance loads and check for convergence. If convergence criteria are not satisfied, the out-of-balance load vector is re-evaluated, the stiffness matrix is updated, and a new solution is obtained. This iterative procedure continues until the problem converges. There are a number of convergence criteria detailed in the ANSYS® program:

convergence based on forces, moments, displacements, or rotations, or on any combination of these items. A force based convergence analysis is used as the convergence criteria for the simulations.

During the simulation for creep analysis, we specified the creep criterion for automatic time step adjustments. The ANSYS® computes the ratio of the creep strain increment ($\Delta\varepsilon^{cr}$), the change in creep strain in the last time step) to the elastic strain ($\varepsilon_{el}$), for all elements. A stability limit is placed on the step size, this is because an explicit integration procedure is used in which the stresses and strains are referred to at time $t_{n-1}$. ANSYS® recommends using timestep such that the creep ratio, $\Delta\varepsilon_{cr}/\varepsilon_{el,}$ is less than 0.10. If the ratio $\Delta\varepsilon_{cr}/\varepsilon_{el}$ is above the stability limit of 0.25, and if the time increment cannot be decreased, the solution diverges and the run will terminate.

# Chapter 4 Vibration Testing and Modelling

## 4.1 Introduction

Vibration testing as discussed in Section 2.2.2 plays an important role in the testing and validation of electronic components. The reliability of a component is of particular importance in the electronics industry because of the wide ranging applications to which it is applied. Electronics devices are increasingly used in hash environments such as automotive, aerospace and defence applications where they were not originally intended to. Apart from the extreme temperature and possibly high humidity, vibration could also be a major cause of failure of electronics components and systems.

To understand the behaviours of electronics components, it is important to acquire the properties of the materials in the components. In order to characterise the properties of solder alloys, a range of test equipment and techniques have been used by many researchers to analyse the response of these materials under various loading conditions. Generally vibration testing is performed using electrodynamics shakers in which the specimen (e.g. a PCB) to be tested is attached onto the shaker assembly and vibration pulse, generally in the z-direction, is applied to the shaker-PCB assembly. One of the main limitations of this testing method is that since the PCB is populated with various components, the precise loading conditions experienced by the various components are not the same but are dependent on their location on the PCB assembly. Therefore, it is not possible to gain detailed knowledge of the behavioural response of individual solder joint interconnections using this technique. The response of solder joint interconnections are dependent on a number of ever varying factors and each individual solder may behave differently. This therefore highlights partly the reason why there is so much scatter in the physical properties of solder interconnects derived using such methods in the literature. Factors such as the vibratory frequency, clamping conditions, size of the test specimen, location on the shaker, etc. are not the same across the different experiments performed. To overcome this limitation Barry [137] designed a fixture that holds up to eight specimens that can be attached to a shaker and shaken in the vertical direction. Although this method attempted to remove the uncertainty and effect of location of the solder interconnects the solder shape was not optimum for the analysis performed as the loading profile will be evenly distributed along the specimen and solder. It is generally accepted that to determine the response of the solder joint to any loading condition, the loading profile should be concentrated on the solder. Also, the limitations inherent in using shakers are still present and it does not simulate the complex loading profiles in service.

There have been numerous studies in designing equipment to analyse the behaviour of solder joint interconnects. Kim and Lee [138] developed a cyclic four point bending tester to analyse solder response to bending. The testing machine applied a load to the specimen via an electro-magnetic coil guided through a linear bushing. Various sensors were attached. A high-resolution load-cell measured the applied loads and these values were used for feedback control. The linear variable displacement transformer (LVDT) for measuring the distance between the two grips was attached at the grips. The failure detection system consisted of a Wheatstone-bridge circuit, which includes a daisy chain of specimens as one resistance arm. A strain measurement system using strain gauges were also constructed that could measure eight channel strains simultaneously.  Herkommer et al [139] developed and commissioned a comprehensive shear testing facility for the testing of metals. It is one of very few test setups reported in the literature that are capable of carrying out in situ optical observation of lead-free solder joints during testing. Bathias[140] developed an ultrasonic fatigue testing machine to determine crack growth and S-N curve of metals. His design operates at different temperature ranges, pressure and also three point bending. Saito et al[141] designed a fatigue testing machine for irradiated specimens with piezoelectric ceramic actuators and a prototype was manufactured for high-cycle fatigue tests with small specimens. The machine has a simple mechanism and was compact. These features make it easy to set up and maintain the machine in a hot cell. The excitation of the actuator can be transmitted to the specimen using a lever-type testing jig. More than 100μm of displacement could be prescribed precisely to the specimen at a frequency of 50 Hz. The relationship of a displacement applied to the specimen and the strain of the necking part of the sample were obtained by experimental methods and by finite element method (FEM) calculations. Both results showed good agreement. Recently, compact vibration test equipment has been designed at the National

Physical Laboratory in order to test small solder joints under vibration loading conditions. As in the work by Saito et al [141], the equipment uses piezoelectric cells as the source of vibration but the solder joint specimen are solder joints made from lead-free solder and copper.

It is expected that the stress and strain distributions in the small solder joint is sensitive to vibration modes of the equipment which may make the design of the equipment more challenging. The main thrust of this work was on the development of equipment for high cycle fatigue testing that will meet the specifications desired by the industrial partner. Once the equipment was developed, there was also a need for a test specimen to be developed that will be used to determine whether the equipment as designed meets the initial specifications.

## 4.2 Solder Joint Test Methods and Equipment

As stated in section 4.1 most of the tests performed to analyse the vibration properties of solder joints are done on shakers. The issues associated with using this procedure in dealing with very small solders in the micron scale is well stated in section 1.4. To overcome these issues a number of researchers have used different mechanical processes and equipment to understand the response of the solder to the loading regime. In some instances, researchers saw the need to design different equipment for the said purpose above. Following are some of the equipment that have been used or designed for the above analysis.

A mechanical cyclic bending testing system was developed by Kim et al [138] shown in Figure 4-1 & Figure 4-2 that used an electro-magnetic coil to apply the load to the specimen. The applied loads are applied through a load cell and this is also used for feedback control. To measure the displacement use is made of a linear variable displacement transformer attached at the grips. They found that the lead-free solder (95.5Sn4.0Ag0.5Cu) has a stronger fatigue resistance than the lead-containing solder (63Sn37Pb) under low loading levels. When the applied load increased, however, the lead-contained solder has a longer lifetime.

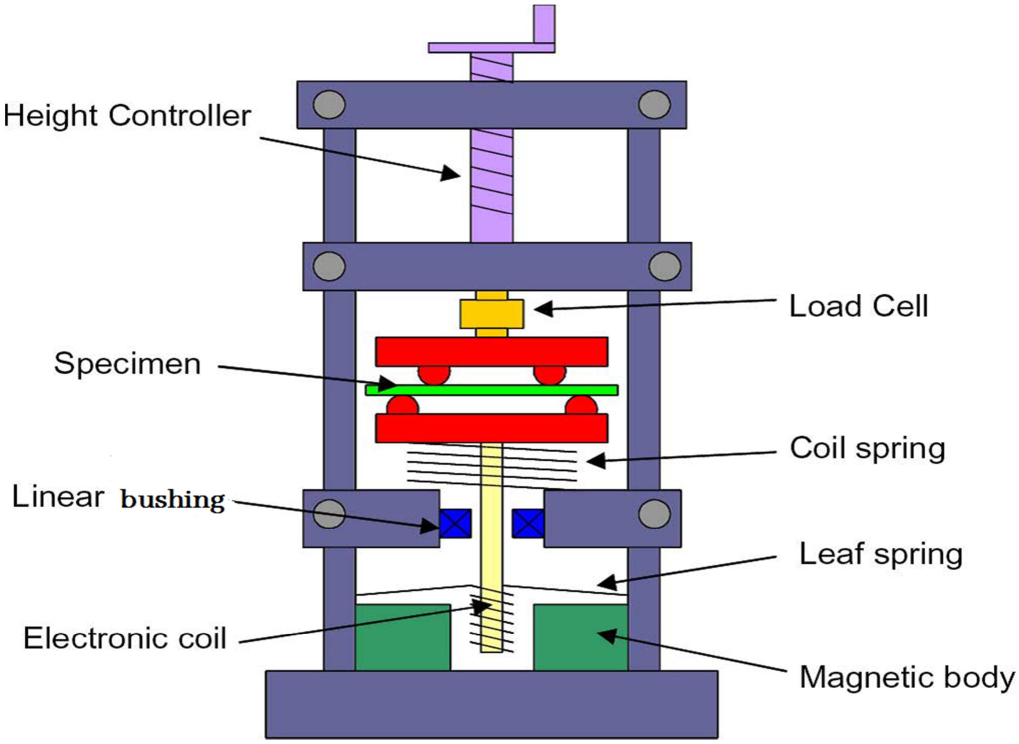

**Figure 4-1 A mechanical solder bending testing system [138]**

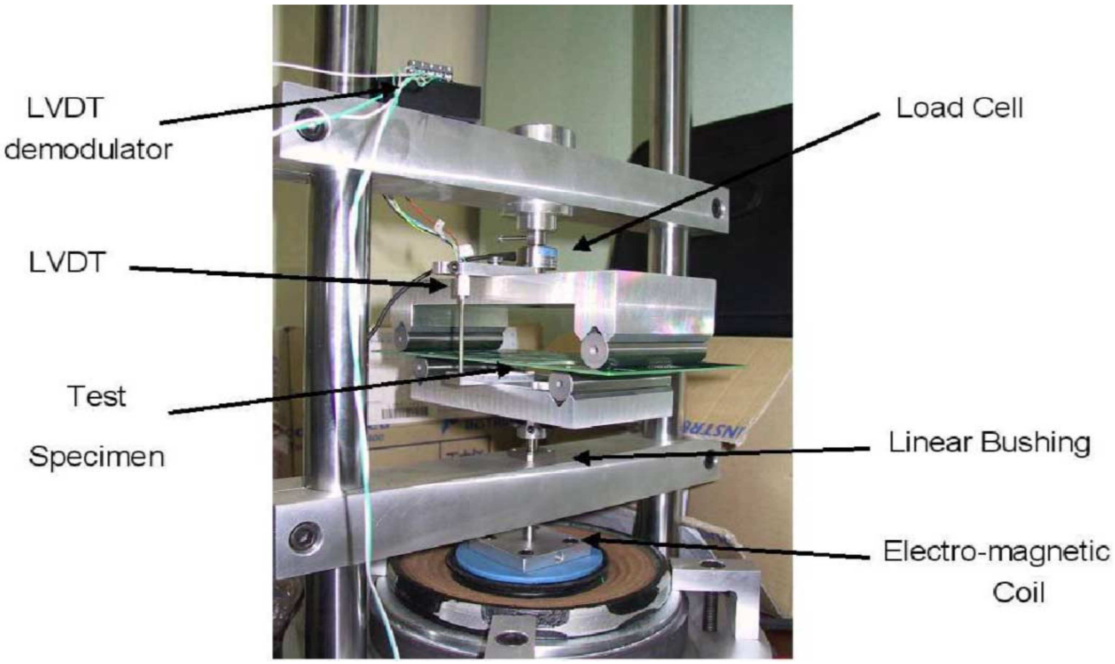

**Figure 4-2 Fatigue testing system [138]**

Saito et al [141] developed a mechanical cyclic bending testing system to investigate the fatigue behaviour of the solder joints for PBGA packages, and a non-linear finite element model considering creep and plastic constitutive models was used to analyse the stress and strain distribution induced during the test (Figure 4-3). It was found that the lead-free solder (95.5Sn4.0Ag0.5Cu) has a stronger fatigue resistance than the lead-containing solder (63Sn37Pb) under low loading levels.

The equipment used piezoelectric cells as actuators. The machine has two actuators (Tokin Co. Ltd.), which are mounted on opposite sides of the testing jig. The piezoelectric material converts the mechanical pressure to an electric field. The advantages of the actuator are high sensitivity to an applied voltage and high positional accuracy. For these reasons, piezoelectric ceramics actuators are suitable for driving a small fatigue testing machine.

The maximum amplitude of the actuator itself is about 120 µm. The displacement of the actuator can be transmitted to the specimen using a lever-type testing jig. The jig presently installed has a lever ratio of 1:3. The maximum amplitude of the specimen is about 360 µm at 26 Hz. The frequency may be varied in the range between 26 and 108 Hz. It is possible to perform tests at lower frequencies by changing the controller unit. The upper limit of the test frequency is determined by the resonance frequency (3 kHz) of the actuator and the following capability of the testing jig.

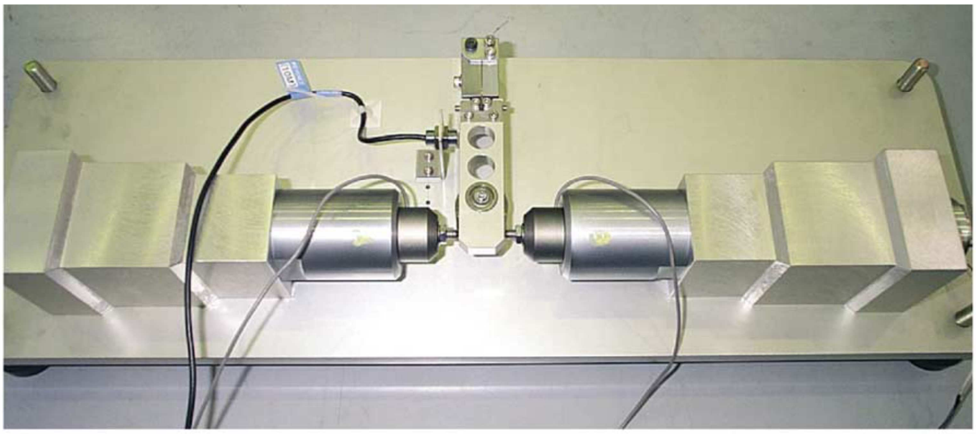

(a)

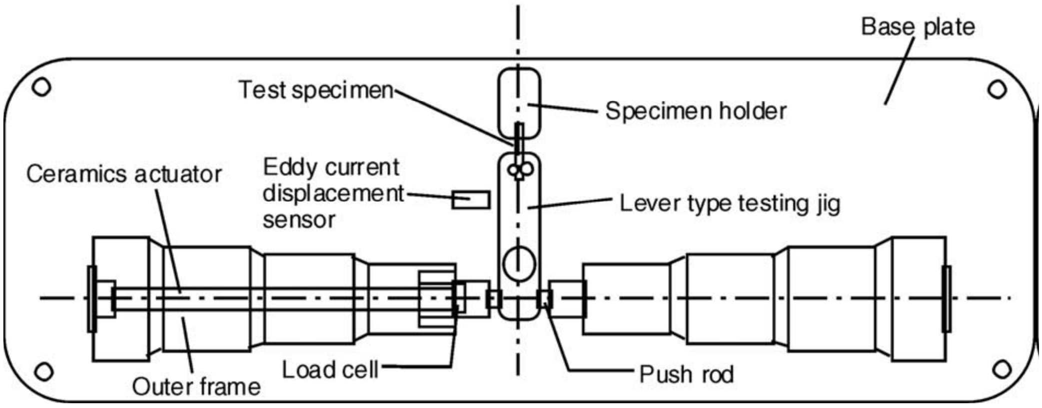

(b)

**Figure 4-3 Test equipment using piezoelectric cells as actuators [141]**

As stated in section 2.1 most of the experimental analysis performed on lead-free solder is done using shakers. There are a number of issues that affect the reliability of the results obtained. Barry [137] tried to eliminate some of these by designing a structural component that holds the solder specimen before being attached to the shaker (Figure 4-4).

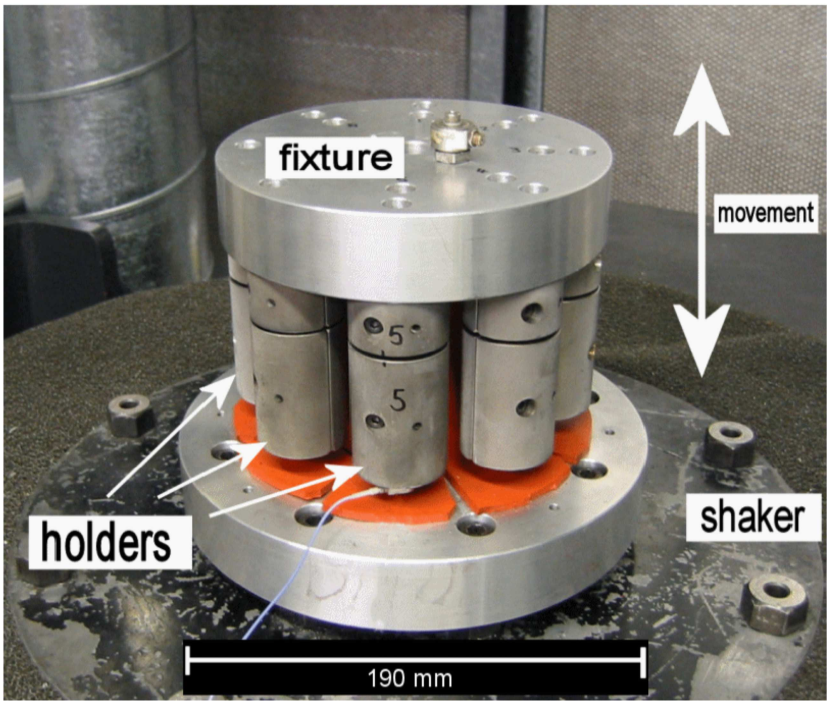

**Figure 4-4 High-cycle fatigue testing fixture, mounted to electro-dynamic shaker, containing stainless steel holders and Cu rods joined by solder [137]**

For small size solder joints, Kim et al [138] developed an accurate testing system which consists of a testing machine part, a control and sensing part, and visual inspection part using a CCD camera (Figure 4-5 and Figure 4-6). The testing machine applied a load to the specimen via a step motor attached to a ball screw driven rail table. The displacement of the specimen can be controlled with the resolution of 0.5μm. The capacity of load cell is 500N and that signal can be acquired with the resolution of 2mV in the range of 10V. The PC controlled the system automatically and acquired all measured signals. The loading fixture for the specimen was designed to be suitable for pull shear and bending test of SMC/PCB assembly.

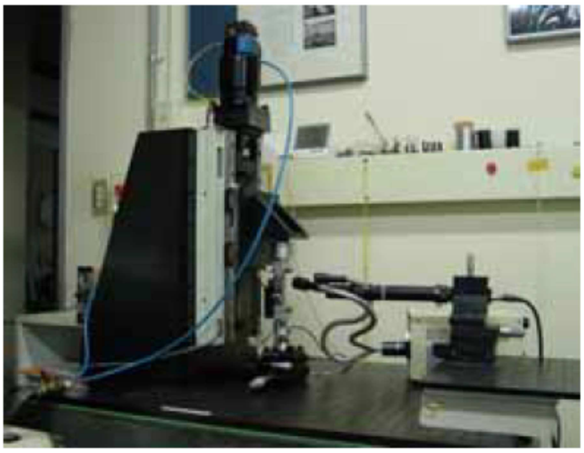

**Figure 4-5 Micro-mechanical fatigue tester with high accuracy load-cell, capacitance sensor and CCD camera [138]**

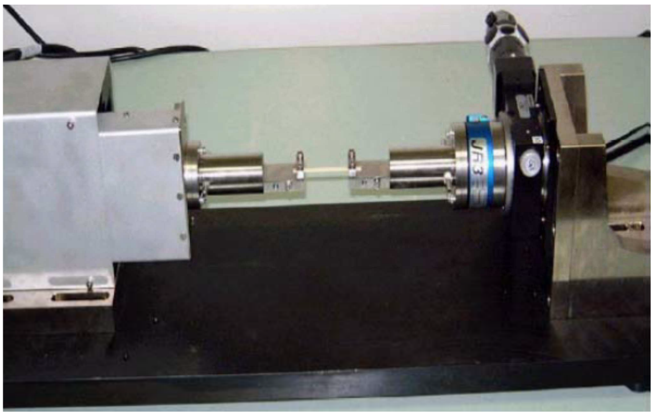

**Figure 4-6 Micro tension tester [138]**

The above discussions about existing test equipment have influenced the proposed design in this work in a number of ways. The use of electrodynamics shakers was not adopted because of the drawbacks discussed and instead piezoelectric cells were used. Most of the equipment highlighted have a vertical profile and hence a smaller footprint, minimising and/or eliminating the small effect of gravity on the samples. This was adopted for the design of the vibration properties testing instrument, resulting in more compact equipment with a smaller footprint than the initially proposed design.

The various design and test equipment highlighted are general engineering testing equipment whose testing are in the macro scale to interpret results for solder joints on a micro scale. This therefore creates a problem of scale and difficulties in analysing the results. The proposed designs will be specifically for small solder joints undergoing thermomechanical and vibration testing.

## 4.3 Vibration Test Equipment Design

Two vibration test equipment designs will be analysed in this sections: the first design and results here presented was published in a paper at the EUROSIME 2010 conference and the second design, though similar to the first in terms of loading methods and specimen design, overall is different from the first and therefore the mechanical response is also different from its predecessor. As noted earlier, this work is a collaboration with NPL and the specification given below are for a production machine that will be used to analyse lead free solder joint interconnects.

### 4.3.1 Specifications

The machine’s designs need to have the following specifications and satisfy the following requirements:

- To perform vibration fatigue test for lead-free solder alloy.
- To operate below 1 kHz frequency with displacement amplitude of about .05 mm for the specimen.
- To be simple, compact, and easily assembled.

- To have provision for the testing under a range of temperatures and the inputs and outputs can be remotely controlled.
- Use commercial piezoelectric cells as the vibration source and possibly have a load cell to measure displacement of the specimen.

### 4.3.2 Testing Equipment

The design idea of the equipment is based on a previous collaboration between the University of Greenwich and NPL, this work is presented elsewhere [143]. The original concept was to have metal turrets to which a vibratory source is attached mounted on a base that will allow the vibration of the specimen to be performed efficiently. As noted earlier most of the equipment used in lead-free solder testing are general testing equipment that were not designed to test small solder joints specifically. Though acceptable results can be obtained from bulk solder testing, they are inadequate for the understanding of miniature solder joints. This equipment, however, is designed for the testing of miniature solder joints of similar size to BGAs used in microelectronics devices. The specifications in Section 4.3.1 were predetermined to ensure that the equipment was fit for purpose.

To meet the requirements as stated in section 4.3.1 above the following design decisions were made:

- The turrets were designed of stainless steel and of size 50x50x50mm$^3$
- The distance between the two turrets is 150mm.
- Commercial piezoelectric cell will be used as actuators with dimensions of 13mm in diameter and 50mm in length
- All of these will be on a granite base of size 400x250x50mm$^3$ to ensure that the equipment is as stable as possible with minimal effect on its environment.

The conceptual design of the equipment without any monitoring equipment is shown in Figure 4-7.

The equipment is constructed to be strain controlled. The piezoelectric transducers produce the vibration at one end whilst monitoring equipment is at the other end. As shown in figure 4-7 and the exploded view in figure 4-8, the specimen is connected to two steel tube holders that house the piezoelectric actuators. The specimen is attached to the holders using two pins that go through holes in the holders and at the two ends of the specimen. One of the piezoelectric cells is used to generate the displacement for the equipment and the other one may be used for monitoring purposes. The minimum amplitude of these actuators will be in the range of 0.1 mm. If elevated temperatures are required in the experiments, heating elements can be introduced to produce a constant temperature around the specimen.

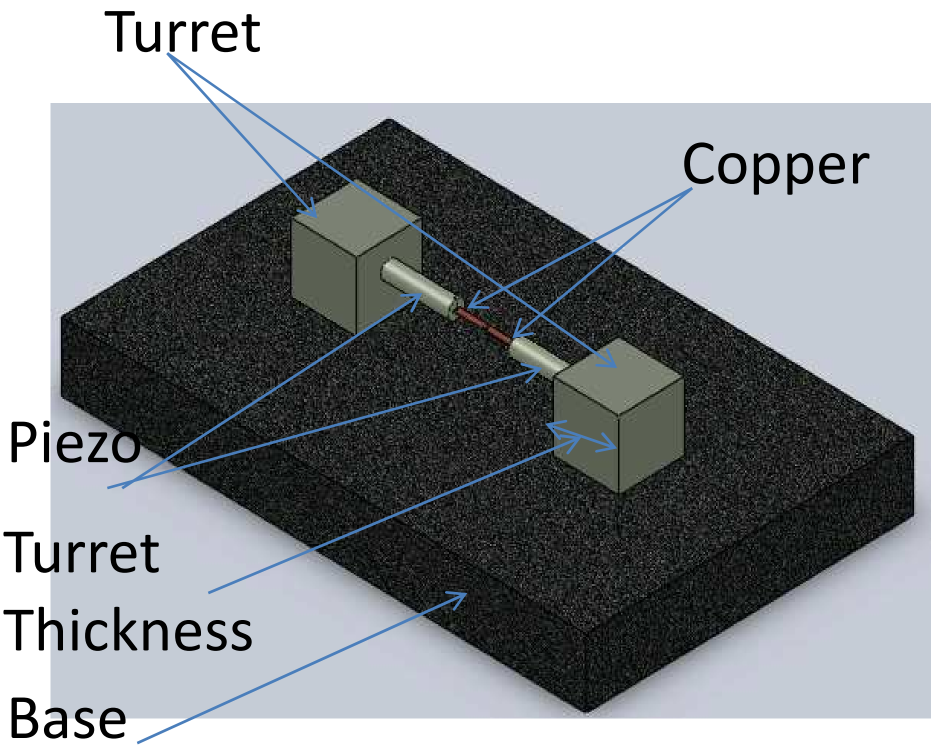

**Figure 4-7 Conceptual design of proposed equipment**

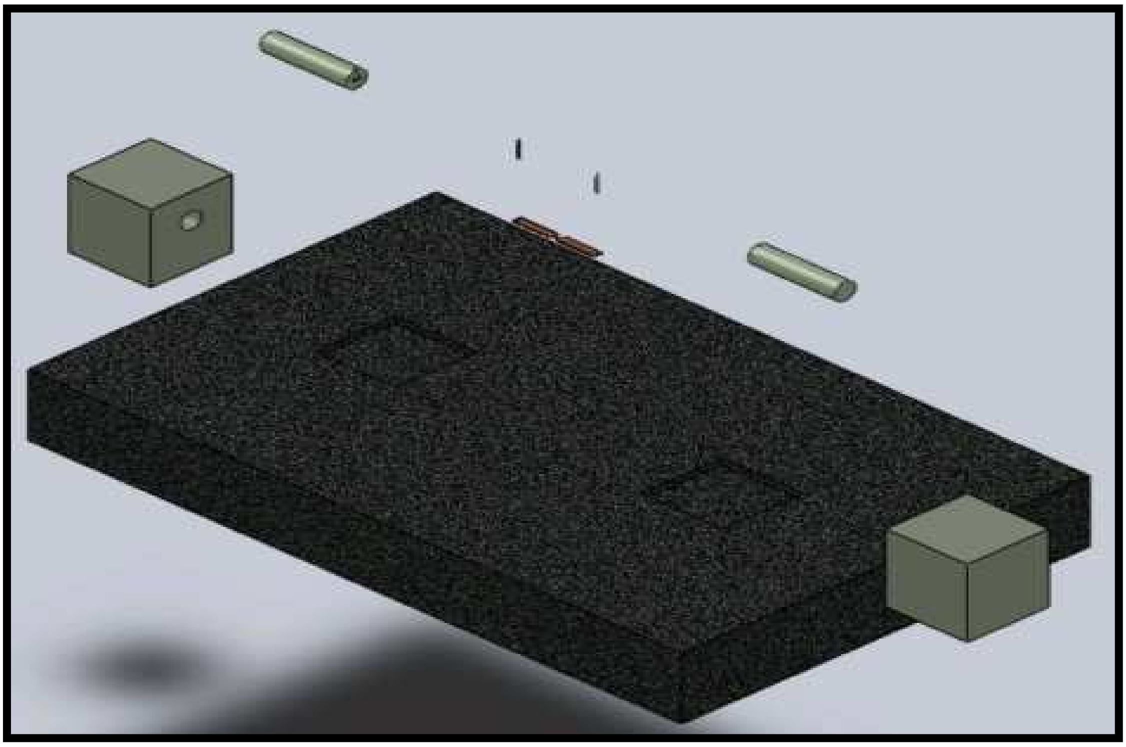

**Figure 4-8 Exploded view of proposed equipment**

The displacement is to be measured using two linear differential variable transformers (LVDT). The equipment is designed to minimise the off axis forces on the sample. The control of the machine is achieved using a PC, which collects displacement, temperature and force readings from an 18-bit A/D data acquisition device, and controls a power source (resistive heating element) via standard communication ports (RS-232C, GPIB, USB). The dataset collected is analysed using Labview commercial software. Although in the design shown here the sample is tested at room temperature, a heater inserted around the sample provides an elevated temperature facility. The instrument is therefore capable of performing an isothermal test under controlled strain conditions, where the displacement follows a defined profile.

### 4.3.3 Test Specimen

The test specimen is constructed from a copper bar of 50mm in length, 5mm in width and 1mm in thickness. In preparing the specimen, a slit of 0.3mm is cut through a 1mm thick copper plate first using an electric diamond saw at slow speeds (Figure 4-9). The solder width is determined by the thickness of the diamond blade. The gap is filled with a solder paste, which may be either lead-free or lead-containing, and reflowed using a gas torch capable of fully reflowing a solder paste. To avoid exhausting the flux and therefore causing voiding, extreme care should be exercised. 50mm sections are now marked onto the copper plates then a circle of 2 mm radius is now punched between the 50 mm copper sections. The reflowed lead free solder is poured into the slit to completely fill the slit cut initially. The copper plate is now cut into 50mm length and the excess solder is sanded down using progressive finer grit paper until all the excess solder have been removed. The copper-solder specimen is now put into an ultrasonic bath to clean the joint and remove the excess oxide that has formed. The specimens are then batch labelled and prepared for testing. Using the cutting blade thickness to control the solder joint thickness is effective, but the quality of the joints produce is a concern and the development of voids in joints is difficult to quantify.

The size of the solder specimen is designed to be reflective of and similar to the sizes of solder balls used in BGA soldering operations and other surface mounted packages. Since there is a piece of copper on either side of the solder, there is a need to ensure that the stress and strains are concentrated on the solder specimen instead of the copper. To achieve this, a large transition radius is designed onto the specimen to allow the stresses and strain to be concentrated on the rectangular sectioned solder specimen.

One disadvantage of this sample design is the compliance in the copper. The sample displacement measured is a combination of the deformation in the solder and the extension of the copper. This elastic extension in the copper can be added to the measured deformation for solder (displacement) presented below.

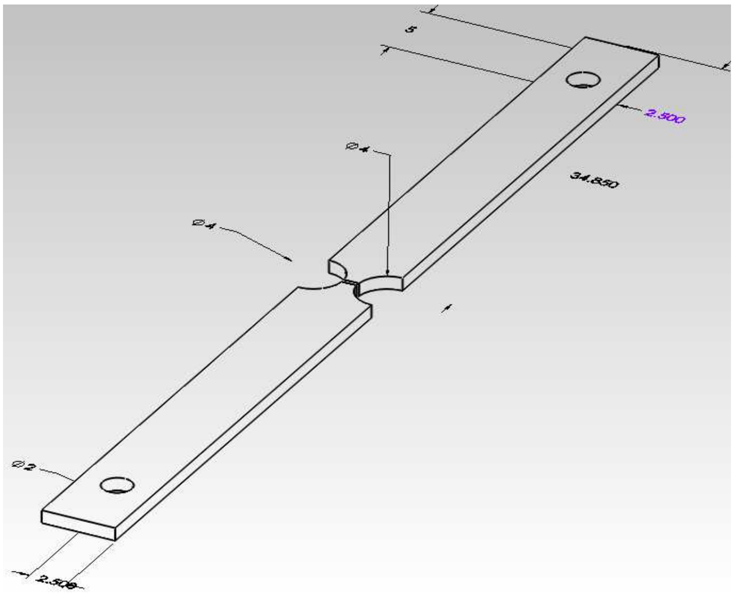

**Figure 4-9 Test specimen. The units are in mm.**

## 4.4 Modelling of Piezoelectric Actuators

To model the piezoelectric vibration source, use is made of the datasheet provided by the manufacturer of the piezoelectric actuator to model its vibration response under electric loading. To be able to use the data provided by the manufacturers in ANSYS® [144], a number of adjustments have to be made to have the data in the format required by ANSYS® (See section 4.4.1).

ANSYS® Solid5 element has been used to model the piezoelectric cells (Figure 4-10). The exact laminate structures of the cells are not known but the maximum displacement range is given in the product specifications. Therefore, the cell is modelled as a single ceramic cylinder which can expand freely along the axis when electric voltage loading is applied. The applied voltage is adjusted so that the total displacement is the same as in the product specifications. A schematic of the PZT cell model and an example of stress distribution are shown in figure 4-11.

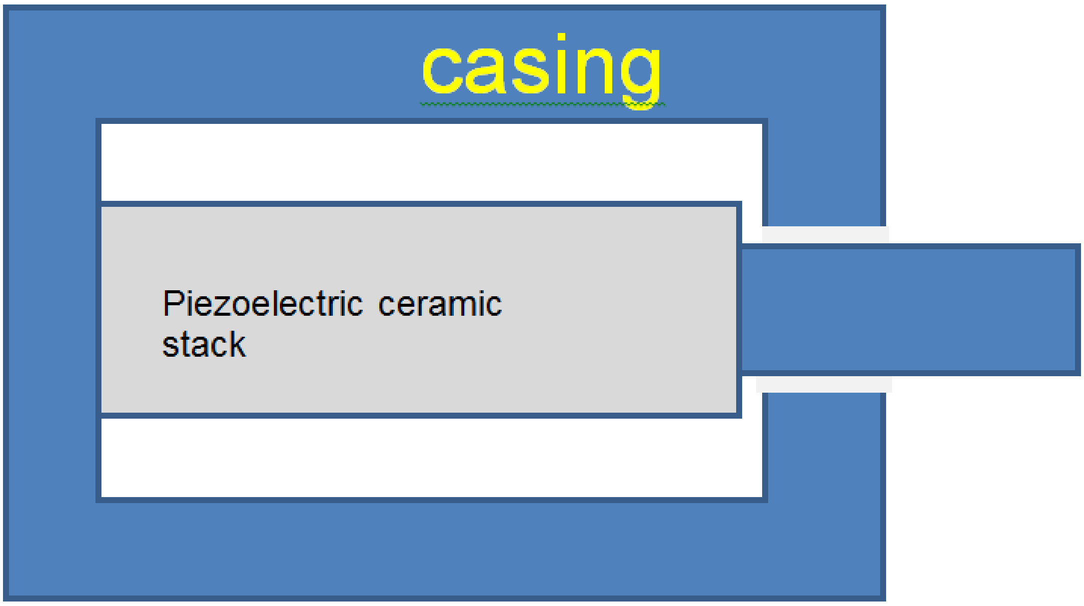

**Figure 4-10 Conceptual modelling of piezoelectric stack. The piezo ceramic is connected to the casing on the left and free to move on the right.**

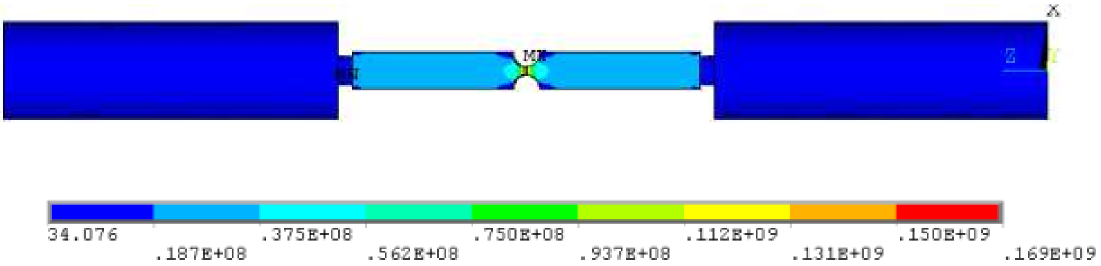

Figure 4-11 An example of Von Mises stress distribution in the test specimen (Pa). Two piezo cells are represented in this model.

### 4.4.1 Piezoelectric vibration source

In modelling the piezoelectric stack in the piezoelectric cell using ANSYS [144], changes and adjustments have to be carried out to the data in manufacturer's datasheet. The constitutive relationship given by manufacturers or published data/reports are in the form:

$$\left[s^E\right]\{T\}=\{S\}-[d]\{E\} \qquad \textbf{(4-1)}$$

$$\{D\}=[d]^t\{T\}+\left[\varepsilon^T\right]\{E\} \qquad \textbf{(4-2)}$$

where

$\{T\}$= stress vector (six components x, y, z, yz, xz, xy)

$\{S\}$= strain vector (six components x, y, z, yz, xz, xy)

$\left[s^E\right]$= compliance matrix evaluated at constant electric field, i.e. short circuit

$[d]$= piezoelectric matrix relating strain/electric field

$\{E\}$= electric field vector (three components x, y, z)

$\{D\}$= electric displacement vector (three components x, y, z)

$[d]^t$= piezoelectric matrix relating strain/electric field (transposed)

$\left[\varepsilon^T\right]$= dielectric matrix evaluated at constant stress, i.e. mechanically free

On the other hand, ANSYS® requires data in the following form;

$$\{T\}=\left[c^E\right]\{S\}-[e]\{E\} \qquad \textbf{(4-3)}$$

$$\{D\}=[e]^t\{S\}+\left[\varepsilon^s\right]\{E\} \qquad \textbf{(4-4)}$$

$\left[c^E\right]$= stiffness matrix evaluated at constant electric field, i.e. short circuit

$[e]$= piezoelectric matrix relating stress/electric field

$[e]^t$= piezoelectric matrix relating stress/electric field (transposed)

$\left[\varepsilon^s\right]$= dielectric matrix evaluated at constant strain, i.e. mechanically clamped

The manufacturer's data as indicated in Equations. 4-1 and 4-2 is based on strain whilst that used in the ANSYS® formulation is based on stress. To convert the manufacturing data in equations.(4-1 and 4-2) to ANSYS® notation in equations (4-3, 4-4) we have

$$\{S\} = \left[s^E\right]\{T\} + [d]\{E\} \qquad \textbf{(4-5)}$$

$$\left[s^E\right]\{T\} = \{S\} - [d]\{E\} \qquad \textbf{(4-6)}$$

$$\{T\} = \left[s^E\right]^{-1}\{S\} - \left[s^E\right]^{-1}\left[d\{E\}\right] \qquad \textbf{(4-7)}$$

Since equation 4-2 relates electric displacement to strain rather than stress, equation 4-5 can then be substituted into equation 4-2

$$\{D\} = [d]^t\left\{\left[s^E\right]^{-1}\{S\} - \left[s^E\right]^{-1}\left[d\{E\}\right]\right\} + \left[\varepsilon^T\right]\{E\} \qquad \textbf{(4-8)}$$

$$\{D\} = [d]^t\left\{\left[s^E\right]^{-1}\{S\} - \left[s^E\right]^{-1}\left[d\{E\}\right]\right\} + \left[\varepsilon^T\right]\{E\} \qquad \textbf{(4-9)}$$

Comparing equations (4-5) and (4-7) with equations (4-3) and (4-4) the following relations between the manufacturers' data and ANSYS® values are obtained as:

$$\left[c^E\right] = \left[s^E\right]^{-1} \qquad \textbf{(4-10)}$$

$$\left[\varepsilon^s\right] = \left[\varepsilon^T\right] - [d]^t\left[s^E\right]^{-1}[d] \qquad \textbf{(4-11)}$$

$$[e] = \left[s^E\right]^{-1}[d] = [d]^t\left[s^E\right]^{-1} \qquad \textbf{(4-12)}$$

These equations formed the basis of the conversion routines used in the simulation.

Assuming polarization in the 3rd-axis (z-axis), the manufacturer's data are mapped to ANSYS® data to generate a compliance matrix:

$$\left[s^E\right]=\left[c^E\right]^{-1}=\begin{bmatrix} s_{11}^E & s_{12}^E & s_{13}^E & 0 & 0 & 0 \\ s_{12}^E & s_{11}^E & s_{13}^E & 0 & 0 & 0 \\ s_{13}^E & s_{13}^E & s_{33}^E & 0 & 0 & 0 \\ 0 & 0 & 0 & s_{66}^E & 0 & 0 \\ 0 & 0 & 0 & 0 & s_{44}^E & 0 \\ 0 & 0 & 0 & 0 & 0 & s_{44}^E \end{bmatrix} \qquad \textbf{(4-13)}$$

### 4.4.2 Permittivity Matrix

The permittivity matrix evaluated at constant strain is input into ANSYS®. Oftentimes, manufacturers' data has permittivity evaluated at constant stress, so conversion is necessary. As noted in equation 4-12, one can calculate the dielectric constants based on constant strain from the following relationship:

$$\left[\varepsilon^s\right]=\left[\varepsilon^T\right]-\left[d\right]^t\left[s^E\right]^{-1}\left[d\right] \qquad \textbf{(4-14)}$$

After evaluating equation 4-12 above, we can input the permittivity. The permittivity matrix has only diagonal terms:

$$\left[\varepsilon^S\right]=\begin{bmatrix} \varepsilon_{11}^S & 0 & 0 \\ 0 & \varepsilon_{11}^S & 0 \\ 0 & 0 & \varepsilon_{33}^S \end{bmatrix}=\varepsilon_0\begin{bmatrix} K_{11}^S & 0 & 0 \\ 0 & K_{11}^S & 0 \\ 0 & 0 & K_{33}^S \end{bmatrix} \qquad \textbf{(4-15)}$$

where $K_{11}^S=\dfrac{\varepsilon_{11}^S}{\varepsilon_0}$ is the relative permittivity. In ANSYS®, the user has the choice of inputting permittivity as absolute or relative values.

### 4.4.3 Piezoelectric Constant Matrix

Usually, manufacturers' data has [*d*], which relates mechanical strain to electric field. However, ANSYS® requires [e], relating mechanical stress to electric field, therefore this means a conversion is also necessary.

From equation 4-12 above, a relationship between [e] and [d] is established as follows:

$$[e]=\left[s^E\right]^{-1}[d]=[d]^t\left[s^E\right]^{-1} \qquad \textbf{(4-16)}$$

where, assuming polarization in the 3rd-axis (z-direction) and symmetry in the unpolarized directions ($d_{32}=d_{31}\ and\ d_{24}=d_{15}$):

$$[d]^t=\begin{bmatrix} 0 & 0 & 0 & 0 & 0 & d_{15} \\ 0 & 0 & 0 & 0 & d_{15} & 0 \\ d_{31} & d_{31} & d_{33} & 0 & 0 & 0 \end{bmatrix} \qquad \textbf{(4-17)}$$

In the manufacturer's data, strain/stress vectors are in the form of {x, y, z, yz, xz, xy} whereas ANSYS®'s mechanical vector is in the form {x, y, z, xy, yz, xz}. This means the rows in [*d*] will have to be shifted: row 4 needs to be shifted to row 5, and, similarly, row 5 to row 6 and row 6 to row 4. Hence $d_{24}$ and $d_{15}$ are shifted one across.

To evaluate the matrix [*e*] with the rows 4, 5 and 6 modified as explain above, the user can use $\left[c^E\right]=\left[s^E\right]^{-1}$. This then becomes

$$[e]=\begin{bmatrix} 0 & 0 & e_{31} \\ 0 & 0 & e_{31} \\ 0 & 0 & e_{33} \\ 0 & 0 & 0 \\ 0 & e_{15} & 0 \\ e_{15} & 0 & 0 \end{bmatrix} \qquad \textbf{(4-18)}$$

## 4.5 Finite Element Analysis of the Equipment

In this analysis, static, modal, and transient Finite Element analysis has been undertaken. Modal analysis is used to determine the natural frequencies and mode shapes of the equipment. The natural frequencies and mode shapes are important parameters in the design for dynamic loading conditions. The resonant frequencies and mode shapes determine the stability of the machine. If the frequency predicted by the model is close to or at the resonant frequency then the machine may undergo uncontrolled non-linear deformation that may ultimately lead to the failure of the structure or misleading test results.

Transient dynamic analysis (sometimes called time-history analysis) is a technique used to determine the dynamic response of a structure under the action of any general time-dependent loads. This type of analysis is used to determine the time-varying displacements, strains, stresses, and forces in a structure as it responds to any combination of static, transient, and harmonic loads. If the time scale of the loading is such that the inertia or damping effects are considered to be important, this method should be used.

### 4.5.1 Material properties

Several materials were used in modelling the specimen and equipment. The elastic material properties used are shown in Table 4-1. In most situations involving vibration, the elastic-plastic properties can be used for all materials. But in the case of very slow vibration, creep may also become important. For creep modelling the Garofalo creep equation has been used:

$$\dot{\varepsilon}_{cr} = c_1\left[\sinh\left(c_2\sigma_e\right)\right]^{c_3}\exp\left(c_4/T\right) \qquad \textbf{(4-19)}$$

The values of the constant for SAC used are given below in Table 4-2.

**Table 4-1 Material properties for the model [20].**

| Material | E(GPa) | Poisson's ratio | Density (kg/m3) |
|---|---|---|---|
| Steel | 210 | 0.30 | 7850 |
| Copper | 120 | 0.35 | 8900 |
| Granite | 70 | 0.25 | 2750 |
| Macor | 66.9 | 0.29 | 2520 |
| Sn3Ag0.5Cu | 35 | 0.4 | 7440 |

**Table 4-2 Garofalo's constants for SAC [20]**

| | |
|---|---|
| C1 | 44100/s |
| C2 | 5e-9 1/Pa |
| C3 | 4.2 |
| C4 | 5412K |

The yield stresses of copper and solder are 70 MPa and 32MPa respectively. The piezoelectric properties of PZT401 [145] have been used in the modelling of piezoelectric cells. The piezoelectric constants in compliances form are used as the inputs of material models in ANSYS®.

### 4.5.2 Meshing of equipment and loading profile

The FEA mesh of the equipment and solder joint specimen model (Figure 4-7) are shown in figures 4-12 and 4-13. The structural elements are modelled using rectangular 3D Solid185 elements and the piezoelectric actuators are modelled using Solid5 elements. To accommodate the difference in the smaller solder joint as compared to that of the copper parts, a gradual transition from small to medium sized elements were used during the element generation.

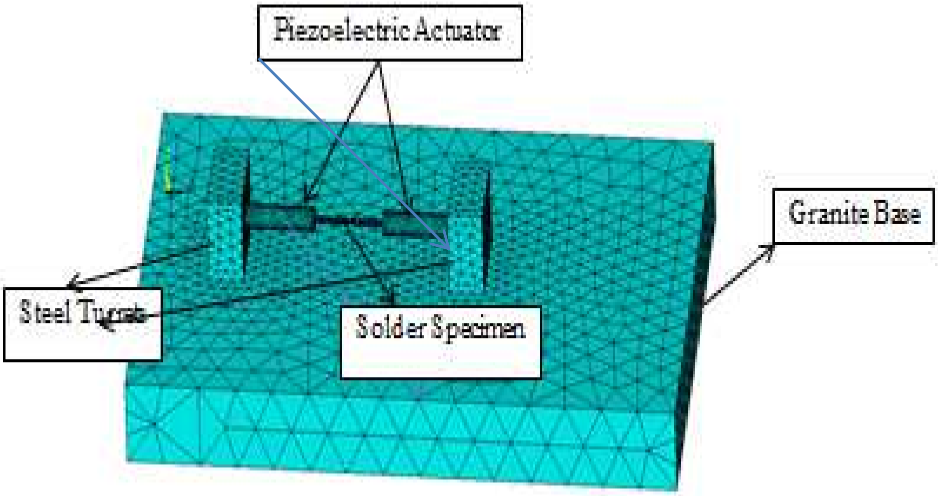

**Figure 4-12 FEA model of concept equipment design**

Different materials were used in the conceptual design of the equipment: the base was made of granite, the turrets were of stainless steel, the piezoelectric actuators were modelled with PZT401, the specimen was of copper and SAC305.

When simulating the entire equipment with the solder specimen attached, the base of the equipment is fixed in all directions (x, y, z). This can be done to simulate the effect of fixing the base on test platform when it is in operation. The specimen is attached to the piezoelectric actuator through design of a holder that fits at the front of the piezoelectric tubes and the base of the specimen. In simulations where only the test specimen part is modelled, the boundary conditions applied are as shown in figure 4-13. One of the end of the specimen is fixed whilst the specified loading profile for the simulation is applied to the other end. The loading profile applied is shown in figure 4-14. This profile is used for testing the response of the equipment to the load.

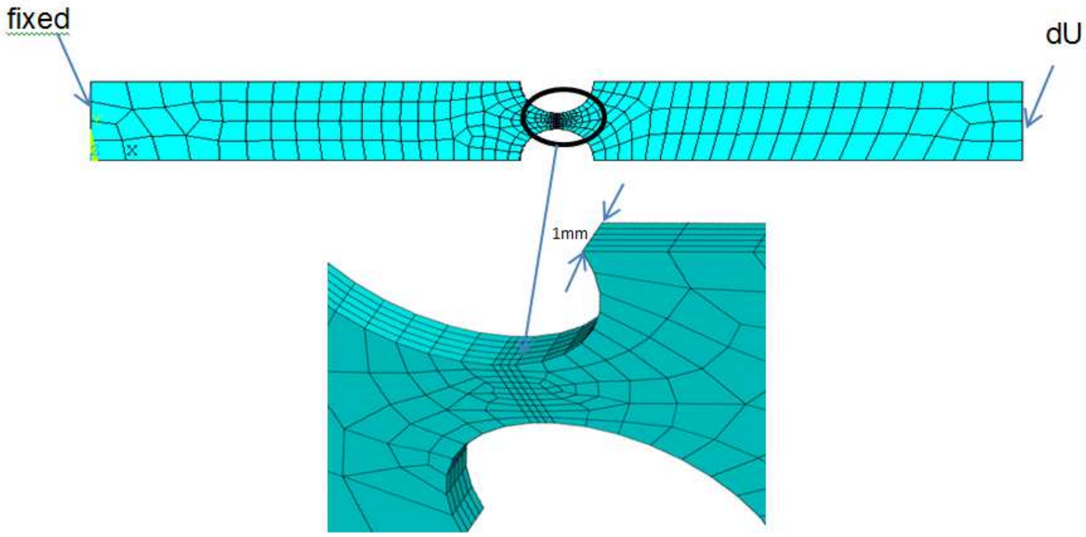

**Figure 4-13 Mesh specimen, with indication of boundary conditions and magnified view. The thickness of the specimen is 300 μm**

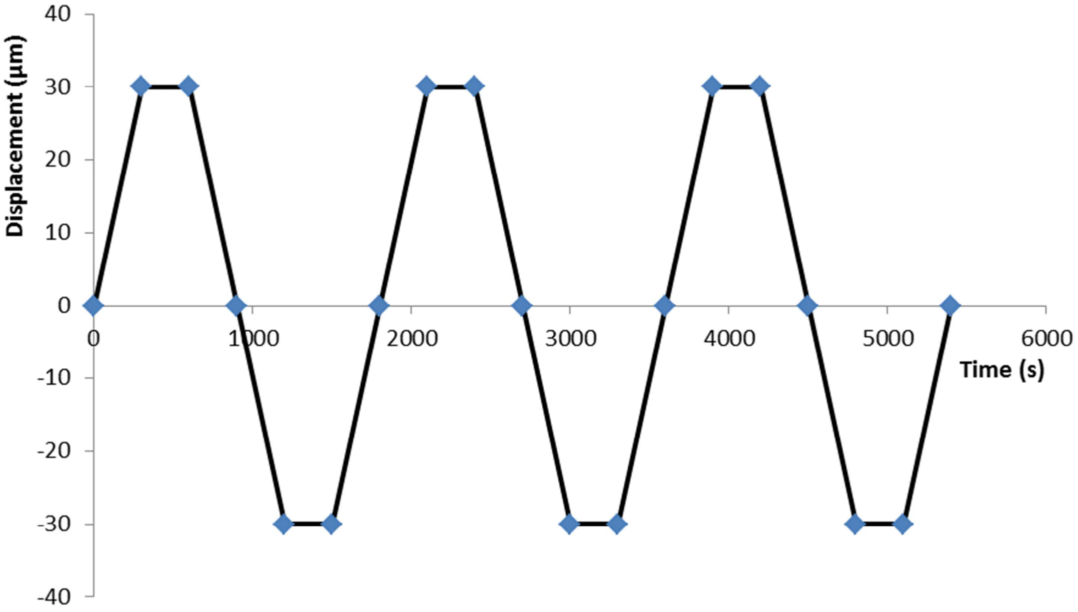

**Figure 4-14 The loading profile applied to the free end of the specimen. The period of the load is 1800s.**

## 4.6 Results and Discussions

Simulation was performed on the entire equipment in order to study the dynamic response of the equipment, and also on the specimen only model so that the deformation of the proposed specimen design can be studied.

### 4.6.1 Modal Analysis of the Equipment

Modal analysis is used to predict the natural frequencies and mode shapes of solid structures. Several algorithms that are implemented in ANSYS® may be used for solving eigenvalue problems. For this analysis, the Block-Lanczos algorithm was used. A number of modes have been extracted and they are compared with the operational frequency to determine the suitability of the proposed design. Ideally resonance should be avoided and the deformation mode does not adversely affect test results.

Three different models were used in this analysis to determine the effect of design variations on the performance of the equipment. The first is the base model which has both the turrets and the actuators made of solid steel (in reality actuator is made of steel and ceramic). In the second model, a 5 mm thermal insulation layer is added to the bottom of the turrets. If implemented, this insulation layer could be useful when tests need to be carried out at temperatures other than at room temperature. The addition of the insulation layer reduces the thermal latency and confine temperature rise to the specimen. The insulation material is assumed to be Macor, which is a machinable ceramic. The third model has also the Macor layer but the piezoelectric cell is modelled as piezoelectric ceramic and this model is used to compare with Model 1 so that the effect of modelling the actuator cell as  steel cylinder can be understood. The three models are summarised in Table 4-3.

**Table 4-3 The models used in the simulation**

| | Model 1 | Model 2 | Model 3 |
|---|---|---|---|
| PZT cell | steel | steel | ceramic |
| Macor | no | 5 mm | 5 mm |

**Table 4-4 Natural frequencies for the three models (Hz).**

| | Model 1 | Model 2 | Model 3 |
|---|---|---|---|
| Mode1 | 1447 | 1446 | 1322 |
| Mode2 | 2885 | 2871 | 1906 |
| Mode3 | 3005 | 2993 | 1985 |
| Mode4 | 3089 | 3076 | 2075 |

The lowest four natural frequencies are shown in Table 4-4. It can be seen that they are all much higher than the proposed working frequency of 1000 kHz. This means that no resonance is possible. The Macor insulation has almost no effect on the modes, especially the low frequency ones. By comparing Model 3 and the other two models, it can be concluded that by modelling the piezoelectric cell as a solid steel cell the frequencies are significantly higher than modelling it as ceramic cylinders. The more accurate values are expected to sit somewhere in between the two sets of results.

The mode shapes of the first and the third modes of Model 1 are given in figure 4-15. The turrets are very stiff and the deformation is concentrated in the specimen. In order to analyse the effects of the turrets dimension on the vibration, analysis has been carried out with turrets' thickness of 5, 10, and 25 mm and the results for the first four modes are shown in Table 4-5. For the mode with the lowest frequency, the frequency decreases only when the thickness is below 10 mm.

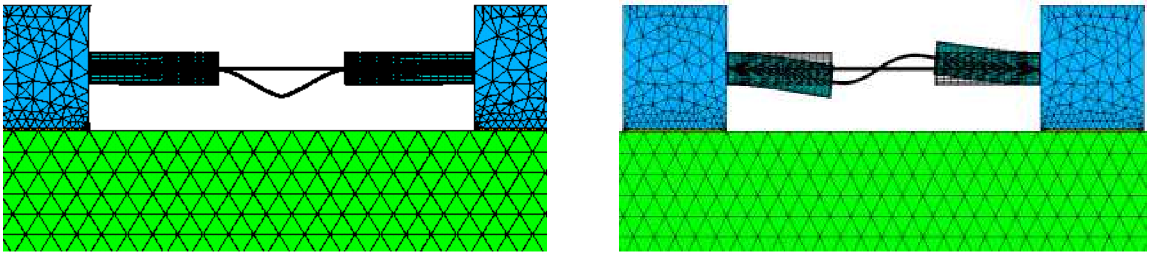

**Figure 4-15 Mode shapes of the first and the third modes of the test equipment without Macor insulation layer.**

Table 4-5 The natural frequencies of the first four modes of the models with turrets of different thickness (Hz).

| Turret thickness | 50mm | 25mm | 10mm | 5mm |
|---|---|---|---|---|
| Mode 1 | 1447 | 1445 | 1432 | 1177 |
| Mode 2 | 2880 | 2839 | 1909 | 1321 |
| Mode 3 | 3012 | 2857 | 2073 | 1605 |
| Mode 4 | 3095 | 2933 | 2537 | 1923 |

Table 4-6 Resonant frequencies (Hz) for double actuator (50mm turrets) with macor

| Macor Thickness | 1mm | 2.5mm | 5mm | 7.5mm | Without macor |
|---|---|---|---|---|---|
| Mode 1 | 1377 | 1377 | 1322 | 1322 | 1447 |
| Mode 2 | 1906 | 1904 | 1903 | 1900 | 2880 |
| Mode 3 | 1989 | 1987 | 1982 | 1980 | 3012 |
| Mode 4 | 2088 | 2087 | 2073 | 2070 | 3095 |

The effect of Macor layer thickness on natural frequency is shown in Table 4-6.

Since the design only considers actuation from a single piezoelectric cell, modal analysis was also performed on a design with a single actuator (Figure 4-16). The mode shapes are similar and the fundamental frequency is above the equipment operational frequency.

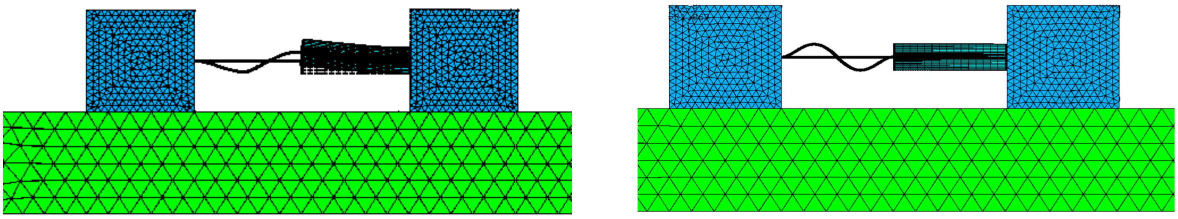

**Figure 4-16 Mode shapes of the first and the third modes of the test equipment with single actuator**

### 4.6.2 Transient analysis of the test specimen

This analysis predicts the deformation of solder specimen under time-dependent mechanical loading as function of time. It is very useful in understanding the way solder joints deforms in a test – very important on the interpretation of test results.

An ad hoc loading profile (shown in Figure 4-14) is applied at one end of the specimen while the other end was fixed. In this simulation, the model contains only the specimen, not the piezoelectric cells because the objective is to investigate how solder joint of different thickness react to loading.

The finite element model of the solder component and an example of predicted stress distribution are shown in figure 4-17. Transient analysis method was used but the dynamics effect is not expected to show up because the specimen is small and acoustic wave velocity in copper is about 4000m/s and the load frequency is very low.

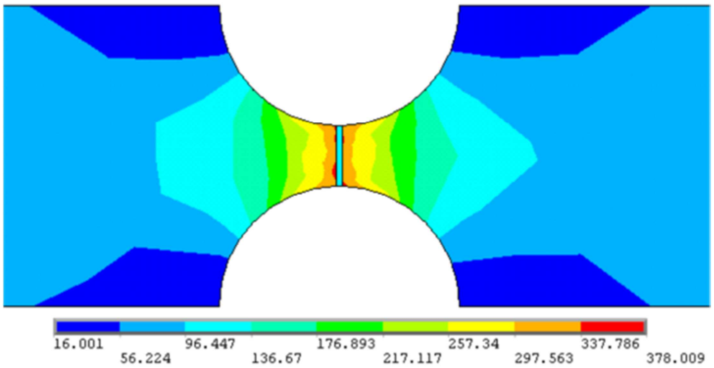

**Figure 4-17 Typical stress distribution around the solder joint. The stress unit is MPa.**

Models with three different solder joint thicknesses were studied: 100 µm, 300 µm and 500 µm, to determine the optimum thickness to use in the analysis. Figures 4-18 to 4-20 showed that the strain, stress and creep strain distribution in the solder joint are inhomogeneous. This is caused by the geometry as well as the deformation of the specimen. It was observed that this strain variation is less prominent in the thinner solder joint. This suggests that any damage accumulation in thinner solder is more evenly distributed in thinner joints. Hence under loading conditions that cause low cycle failure, Coffin-Manson type lifetime model may be more suitable for thinner solder joints than the thicker ones. In the thicker solder model, a crack propagation rate model is perhaps more applicable. If a Coffin-Manson model is used for the thicker solder joint a width parameter may need to be included.

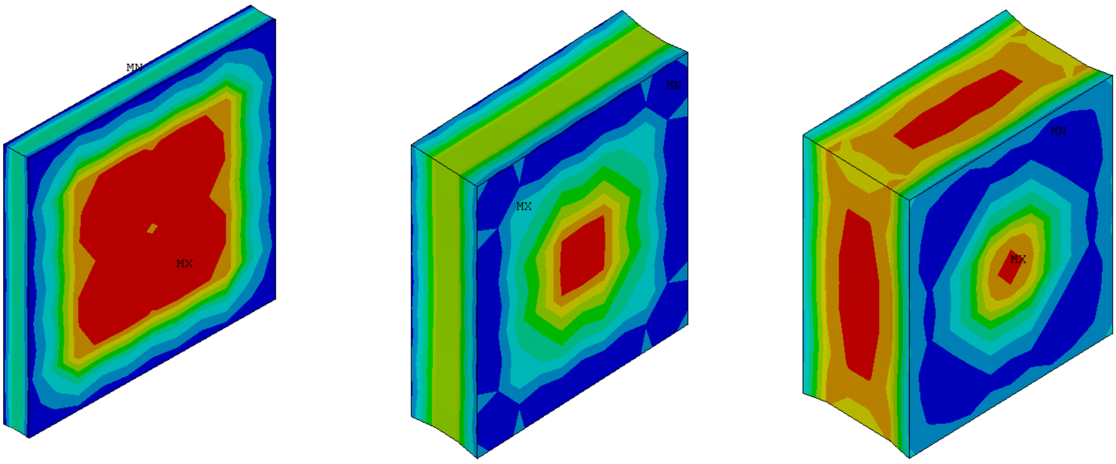

100µm thick

Min :  0.002439

Max:  0.00769

300µm thick

Min : 0.002032

Max : 0.007027

500µm thick

Min : 0.001387

Max: 0.005091

**Figure 4-18  Von Mises Strain in solder of various thickness at t=240s.**

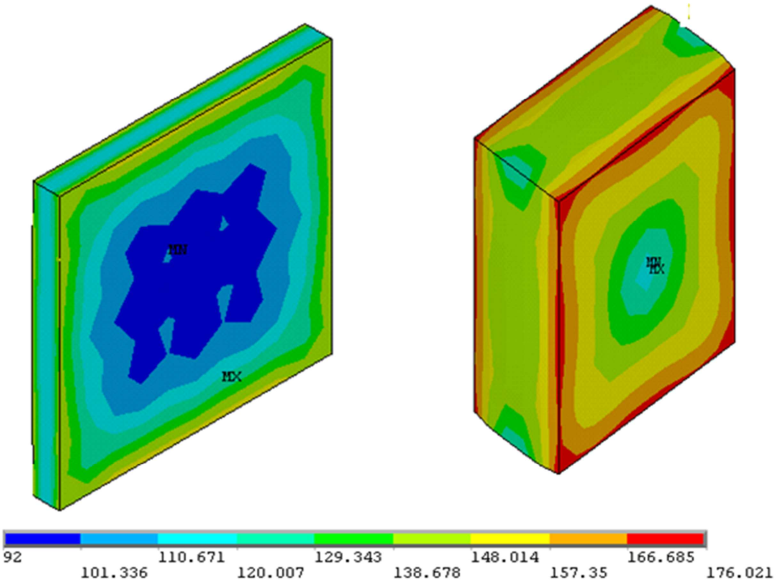

**Figure 4-19   Von Mises Stress distribution at t=302 s for the 100µm specimen on the left and the 500µm specimen on the right.**

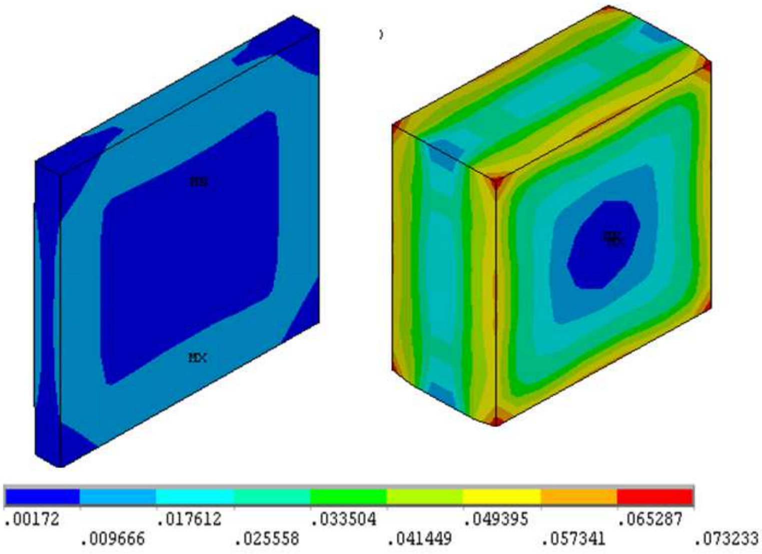

**Figure 4-20   Creep strain distribution at t=302 s for the 100µm specimen on the left and the 500µm specimen on the right.**

The results shown in Figures 4-19 & 4-20 are from simulations at a load frequency of 0.00056 Hz and at this low frequency creep strain is significant in the solder joint. As the loading frequency increases, this strain is expected to decrease. In fact, as shown in Table 4-

7, where the maximum stress and strain are listed for a few different loading frequencies, creep strain decreases by about 1000 times as frequency increases from 0.08 to 0.7 Hz. This shows that at high frequency visco-plastic strain becomes negligible and in damage analysis only rate-independent plastic strains need to be taken into count and this makes easier to determine if low cycle fatigue is expected for given load level.

**Table 4-7 Maximum von Mises stress and equivalent creep strain (at the end of 3.5 cycles).**

| Frequency (Hz) | Maximum Von Mises Stress(MPa) | Equivalent creep strain |
|---|---|---|
| 0.7 Hz | 95 | $8x10^{-7}$ |
| 0.08 Hz | 95 | $5x10^{-3}$ |
| 0.01 Hz | 101 | $4x10^{-2}$ |

### 4.6.3 Effect of solder thickness on stress strain distribution

Solder joints with three thicknesses, 100µm, 300µm and 500µm were modelled and the distribution of stresses and strains across the solder specimen were analysed. The maximum stresses and strain for the modelled solder thicknesses are shown in Table 4-8 below.

**Table 4-8 Maximum and minimum stresses and strain for the different thicknesses modelled at the end of three cycles. The units of stress are MPa.**

| Solder Thickness | Min Von Mises Stress | Max Von Mises Stress | Min Von Mises Strain | Max Von Mises Strain |
|---|---|---|---|---|
| 100µm | 123.827 | 421.446 | 0.002439 | 0.00769 |
| 300µm | 110.65 | 360.748 | 0.002032 | 0.007027 |
| 500µm | 52.473 | 142.976 | 0.001387 | 0.00385 |

The results above indicates that the thinner the specimen the greater the stresses and strains it is exposed to. The distribution of stresses is also different between all three thicknesses. This result is expected because compared to copper, solder joints bears most of the applied displacement loading and the thicker the solder joint the lower the strain for a fixed loading.

## 4.7 Improvements and Results

The design described above meets all of the initial design requirements but there are a number of issues that needed to be addressed to make the implementation of this equipment as effortless as possible.

The specimen attachment mechanism (Figures 4-7 and 4-8) is a concern as it introduces out of axis stresses that can lead to breakage of the solder joint and introduce uncontrolled deformation mode that complicates stress state analysis of solder joint. The profile of the equipment was also of concern as the gravitational effect, although small because of the sample sizes, will cause misalignment of the sample. There is a need also to reduce the footprint of the equipment to achieve better portability. To address these issues, the equipment was redesigned.

### 4.7.1 New Equipment Design

The assembled equipment design and its exploded view are shown in figure 4-21 and figure 4-22. The principle of operation of this equipment is similar to that presented in section 4.5. The vibration source is provided by a piezoelectric cell and the monitoring equipment is attached on the frames. Simulations were performed to analyse the response of the new equipment to the prescribed loading condition.

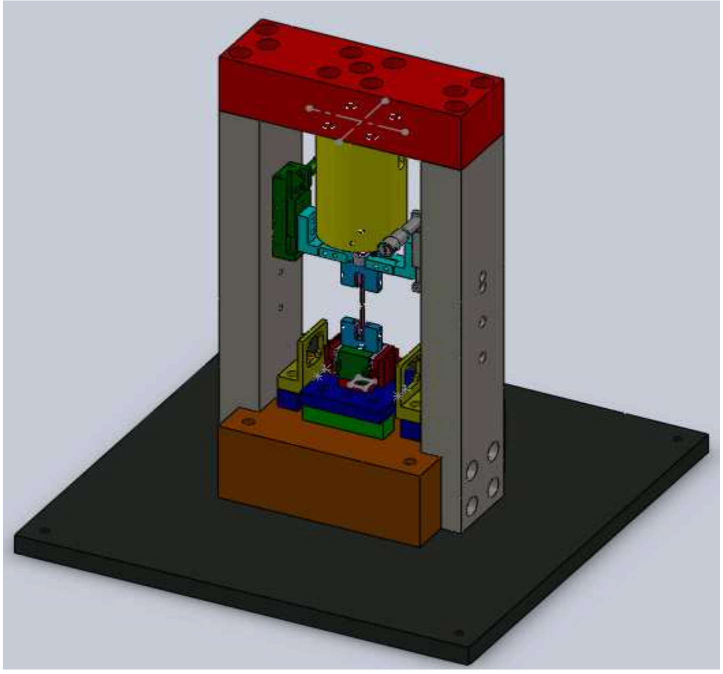

Figure 4-21 Re-design high cycle fatigue solder tester

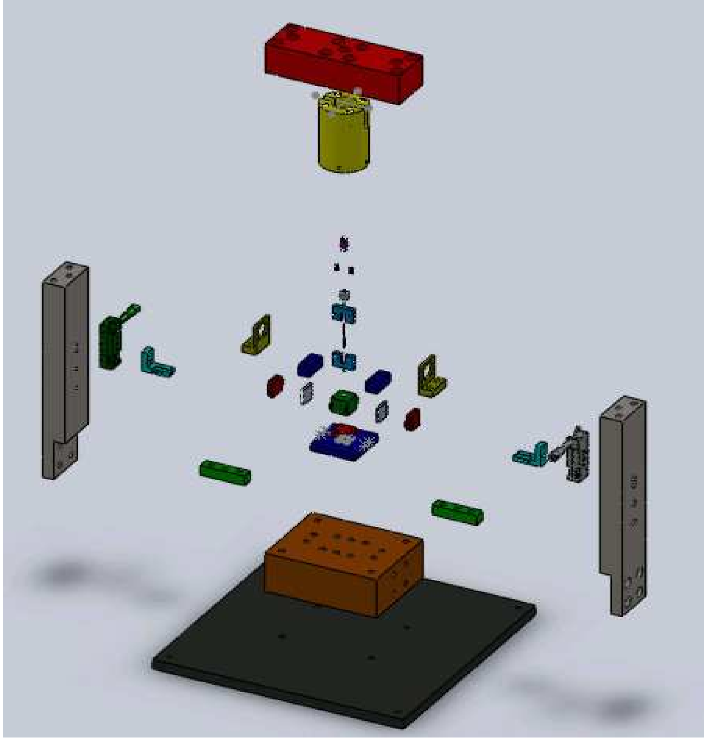

Figure 4-22 Exploded view of test equipment

In this new design, the equipment has a vertical profile and the specimen is attached to the specimen holders using clamps that are tightened using screws.

### 4.7.2 Modal Analysis

To assess the compatibility of the new design to the design specifications, modal analysis was performed on the new design without any parts of the monitoring equipment. The geometry model and the mesh of the equipment is shown in figures 4-23 and 4-24 respectively.

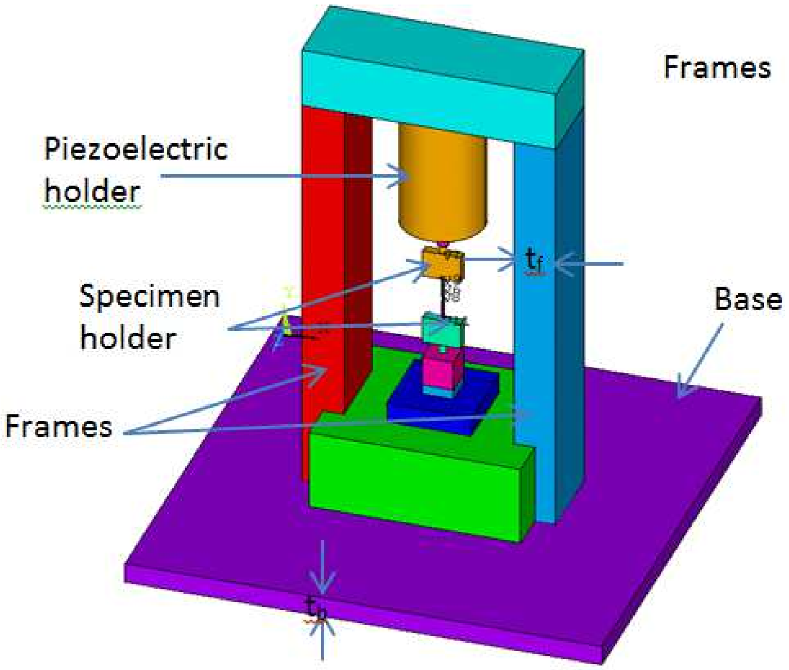

**Figure 4-23 Volume representation**

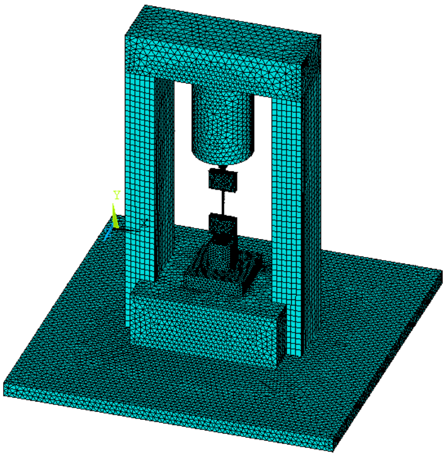

**Figure 4-24 Mesh of equipment**

The first four natural frequencies are shown in Table 4-9, and the mode shapes are shown in figure 4-25. The response of the equipment during the modal simulation demonstrates that the first three modal shapes are mainly due to the deformation of the frames. This therefore poses a serious concern for the above design in that the first four modal frequencies are well below the proposed operational frequency of the equipment. This therefore indicates that there is a tendency for the equipment to perform at its resonant frequency during its operation. The material column represents the finite element model using the different material properties for the different components.

**Table 4-9 Modal frequencies for the models**

| Modal Frequencies (Hz) | | | | |
|---|---|---|---|---|
| Mode | All Steel | Material | Adjust 1 | Adjust 2 |
| 1 | 274 | 206.9 | 275.9 | 274.2 |
| 2 | 405.8 | 239.9 | 408.1 | 405.8 |
| 3 | 645.8 | 594.9 | 648.3 | 645.8 |
| 4 | 875.8 | 873.9 | 875.8 | 875.7 |

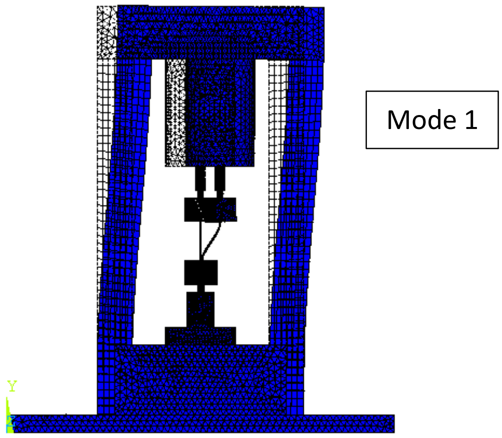

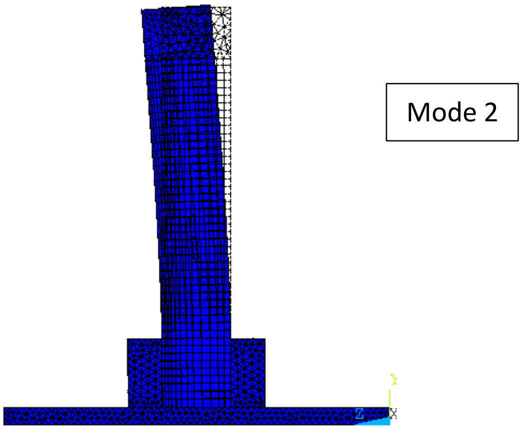

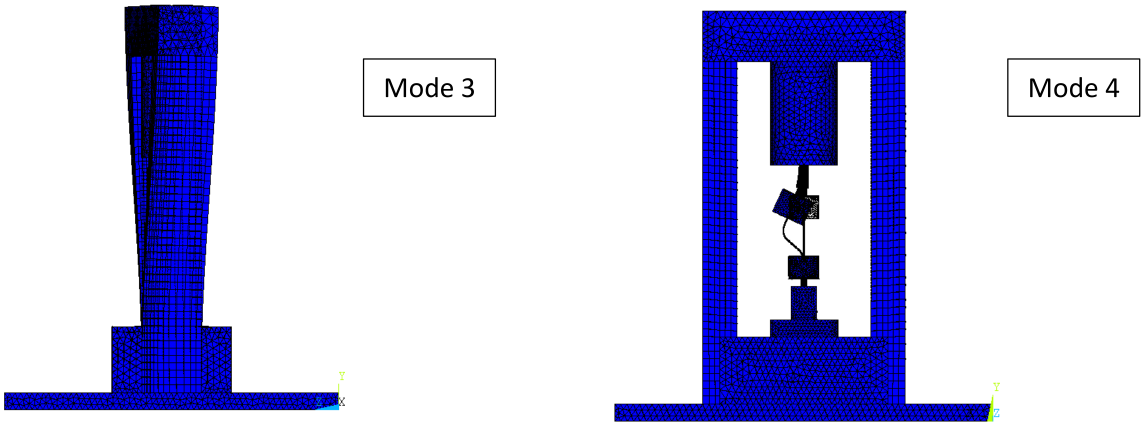

Figure 4-25 First four mode shapes of the new equipment

The mode shapes shown above demonstrate that the major issue with the above design has to do with the effective stiffness of the frames. The first three mode shapes involves the translation and/or rotation of the frames.

In order to analyse the effect of the dimensions of the frame and base, two design variations, “Adjust1” and “Adjust2”, were studied and the results are compared with that of the initial design (Figure 4-26). Adjust1 has a frame thickness $t_f$ (Figure 4-23) that is 50% thicker than the original design and Adjust2’s frame and the base thickness is increased by 50%. The results indicate that the increase in fundamental frequency is not very appreciable. This is because the fundamental natural frequency of the structure is given by

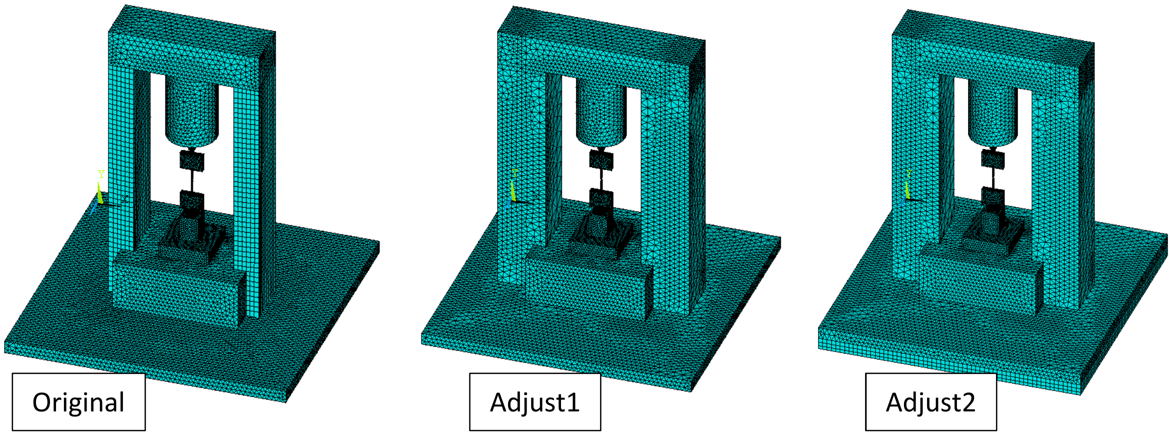

Figure 4-26 Three models compared and simulated

$$f = \sqrt{\frac{K_{eq}}{M_{eq}}} \tag{4-20}$$

where $K_{eq}$ is the equivalent stiffness and $M_{eq}$ is the equivalent mass. This therefore demonstrates why the increase in fundamental frequency is not as fast as expected because when the dimensions increase, the stiffness of the equipment increases but at the same time the equivalent mass also increases and this has a small effect on the frequency. This means that changing the dimensions of the equipment does not always change the natural frequencies of the structure. Although by changing the dimensions in other ways may change the natural frequencies question may also be asked if resonance causes any significant impact on the particular equipment in question. In order to answer this question a harmonic analysis was performed so that the response of the equipment to applied loading at a range of frequencies can be obtained.

### 4.7.3 Harmonic Response

Since the calculated fundamental frequency is far lower than the operational frequency, the response of the structure at the fundamental frequency needs to be obtained using harmonic analysis method.

During the harmonic analysis, the solution of the time dependent equations of motion for a linear structure undergoing steady vibration is calculated. All loads and displacements vary sinusoidally at the same frequency.

$$\begin{aligned} F_i &= F\sin(\omega t + \phi_1) \\ F_j &= F\sin(\omega t + \phi_2) \end{aligned} \tag{4-21}$$

The harmonic response of the structure is shown in figure 4-27. The analysis generates a plot of the amplitudes of displacements at given points in the structure as a function of the forcing frequency. This confirmed the modal results that the largest deformations are at the frames.

The maximum response of the frame is 0.02% of the applied displacement and the deformation at the specimen is much smaller. However, this resonance may still cause noise and long term reliability issues. A number of variations in the dimensions of the overall equipment were discussed and analysed. The changes in the design increased the stiffness of the equipment but they had quite limited effect on fundamental frequency. Further changes in design by adding stiffeners may work better but are not cost effective because they increase the weight and the complexity in fabrication. As the response at resonance was quite small in relation to the applied load, passive vibration suppression technique was used as it was less expensive and can be implemented quickly.

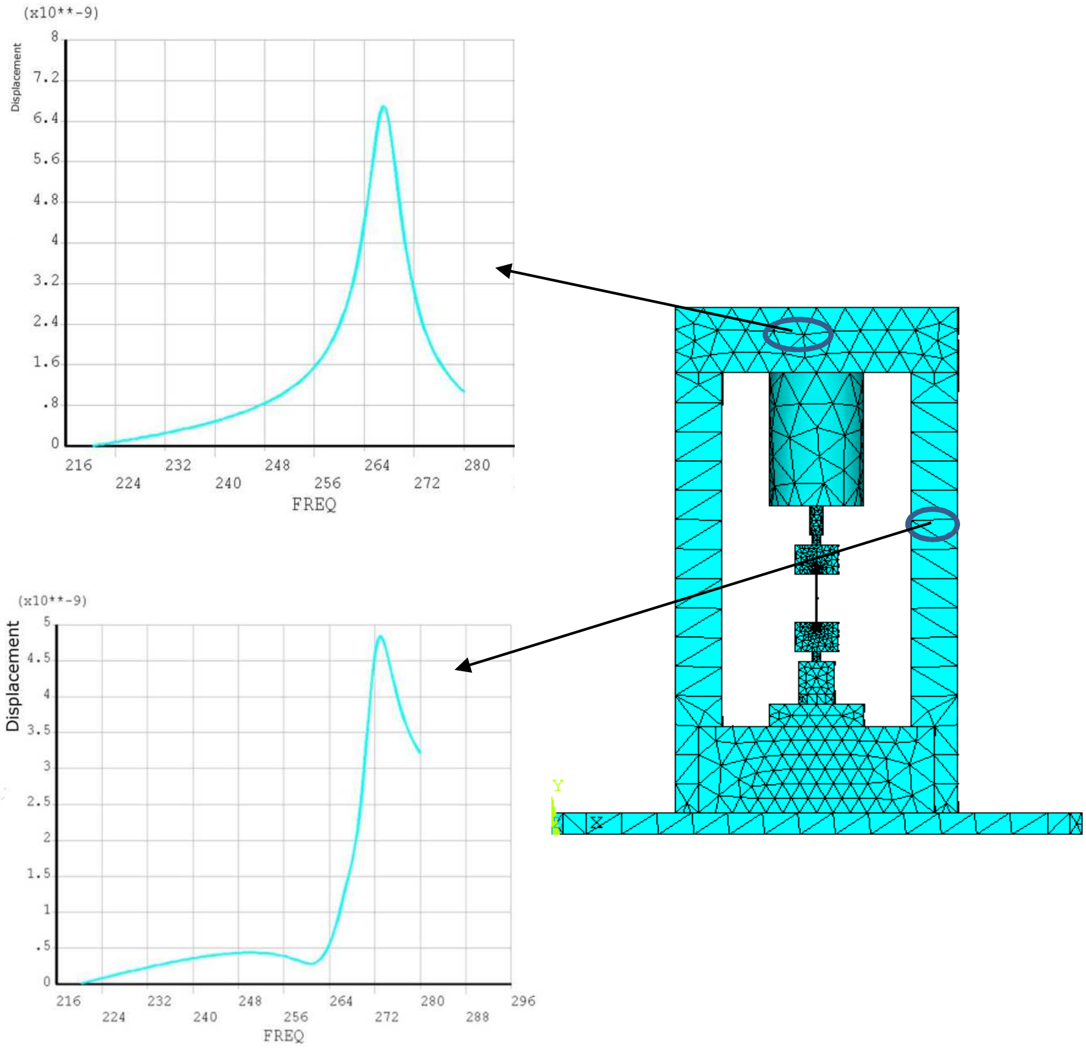

**Figure 4-27 Harmonic response of the frame and top bar. The units of the displacement and frequency are meter and Hertz respectively.**

## 4.8 Summary

The vibration test equipment has been analysed using the FEA method to determine whether it will operate with the design parameters as envisaged. It was determined that the final design's natural frequencies are within the range of proposed working frequency. Several ideas were looked at in trying to alter the natural frequencies. Increasing the thicknesses of the frames and the base has only a small effect on the overall resonant frequency because of the direct and inverse relationship of the resonant frequency to the equivalent stiffness and equivalent mass. This therefore means that as the dimension increases, the mass also increases which affect the change in the natural frequencies of the equipment. With the help of these results, NPL decided to use vibration suppression technique to solve the resonance issue. Vibration suppression is the practice of using damping, isolation or a cancellation solution to reduce or eliminate vibrations that would otherwise result in loss of performance or limit the useful life of a system. Vibration suppression can either be passive or dynamic. For the above design passive vibration damping was applied to the base of the equipment ensuring that there is no out-of-control vibration during testing.

# Chapter 5 Testing and Modelling of Solder Joints under Cyclic Mechanical Loading

Thermal-mechanical fatigue of solder joints is of significant concern in the design and manufacturing of high reliability electronics products. In both test and real application environment, solder interconnects are often the most vulnerable parts of a device. This is because they are often used to connect components with different thermal expansion coefficient and solder joints are susceptible to inelastic deformation even at room temperature and moderate stress levels. The continuous match of replacing SnPb solder with lead-free solder in high end safety critical packages and its use in array packages makes the determination of the behaviour of the solder joint of paramount importance. It is therefore vital that the performance of these joints be properly understood.

In the electronics manufacturing industry, the performance of solder joints are routinely assessed under cyclic thermo-mechanical testing conditions where cyclic temperature loading is applied, or isothermal cyclic mechanical testing where cyclic mechanical loading is applied. In both test methods the solder joint experiences cyclic stresses and damage accumulates leading to crack formation and propagation in solder joint. While the loading conditions in a temperature cycling test resemble more closely those extreme environments that the devices may experience in real applications, the test method requires environment chambers with cumbersome supporting infrastructure. In this work, the latter method was used but the deformation of solder joints in the test specimens resemble that in a strip of a BGA package that is subject to cyclic thermal-mechanical loading.

A number of different specimen designs and methods for solder joint test have been used in the industry and research labs to analyse solder specimens in shear, and prominent amongst these is the grooved lap-joint (GLJ), which is shown in figure 5-1. Grooved lap joints are designed for easy manufacture and to produce a nearly uniform distribution of shear stress in the solder joint with very little bending. Another advantage of the GLJ is that the size and deformation profile of the solder joint is similar to many solder joints in real electronics devices. The geometry of the lap joint that is reported here is derived from the work of

Reinikainen et al [146]. To understand the solder joints' response to stress and strain in real applications, solder joint size and the solder's microstructure such as the grain size needs to be as realistic as possible.

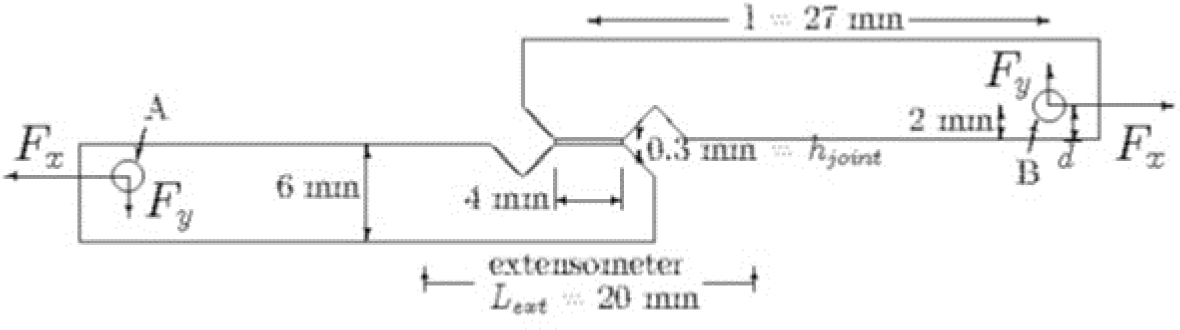

**Figure 5-1** Groove lap joint [146]

Other types of specimen have also been developed in the past and the single and double lap joints are two examples of these specimens. Single lap joint specimens are similar to grooved lap joint specimens but without the groove. Double lap joints have two solder joints in one specimen on the two sides of a mirror symmetry plane. The desired microstructures of these solder joints can be achieved by controlling the manufacturing process. Darveaux et al [147] have used a BGA type specimen in which two rigid plates are soldered together using an array of solder interconnections. These are realistic representations but the stresses and strains are less uniform than in the groove lap joint. This is adequate for the purpose of analysing the solder joint reliability performance but this does limit the accuracy of the creep strain rate model that can be obtained from experiments because of the complexity of the stress state in the BGA solder joint.

Ball Grid Array (BGA) is a surface mount packaging technique that is popular in electronics manufacturing industries. It offers high interconnection density, easy assembly, and low thermal resistance compared to other packaging technologies such as through-hole packages. Typically, a square array of solder balls connect a laminate substrate and a semiconductor die. Because of their geometry, the ball-shaped solder joints in BGAs are not able to easily deform to accommodate thermal-mechanical and other stresses [148]. Due to the Coefficient of Thermal Expansion (CTE) mismatch between Printed Circuit Board (PCB) substrate and the package, solder joints experience a cyclic strain in temperature varying conditions that induce fatigue in the solder joints and other parts of the assembly, leading to failure of the solder resist, delamination at interfaces of materials, or in the solder joints [149, 150].

This work, is focused on isothermal fatigue testing of specimens containing multiple solder joints. The specimens have been designed in such a way that they are inexpensive, easy to manufacture and the deformation of the solder joints is similar to those found in BGAs that are subject to thermal-mechanical loading. The principal aim of the work is to establish an effective low cost test and analysis system that can be used for the evaluation of solder alloys that are used for BGAs, and to provide material data that can be used in physics-of-failure based reliability prediction for BGA or other similar devices with solder interconnects.

## 5.1 Test Equipment and Specimen

The solder interconnect test specimens with multiple joints were fabricated from copper coupons of size 51×6×1 mm. A low speed diamond saw was first used to produce a 0.3 mm wide cut running centrally along almost the entire length of the coupon. This slit was placed over a jig comprising an oxidised stainless steel shim with a specified number of slots corresponding to the size and number of joints required in the sample. Before soldering, this space was filled in excess with the desired solder paste. In this study, 96.5Sn3.0Ag0.5Cu lead free solder was used. The jig was then placed onto a hot plate in order for the solder to reflow. After about 5 seconds into the reflow process, the jig was removed from the hot plate and placed on a cold metallic surface to cool such that the time above the reflow temperature was between 10 to 30 seconds. This above-reflow-temperature period is shorter than that in general reflow of lead-free soldering. Therefore, this limits the development of intermetallics and the subsequent modelling assumption that the effect of intermetallics on the solder joint behaviour is limited and thus the representation in the model is an accurate representation. Abrasive paper was used to remove excess solder and slots were cut in the sample such that when pushed/pulled, a shear force is applied to the solder joints. Samples with 1 to 8 joints were prepared using this procedure and these are referred to as M1-M8. These specimen preparation steps are illustrated in Figure 5-2. The dimensions of a 5-joint specimen are shown in figure 5-3 and the CAD model of a four-joint sample is shown in figure 5-4.

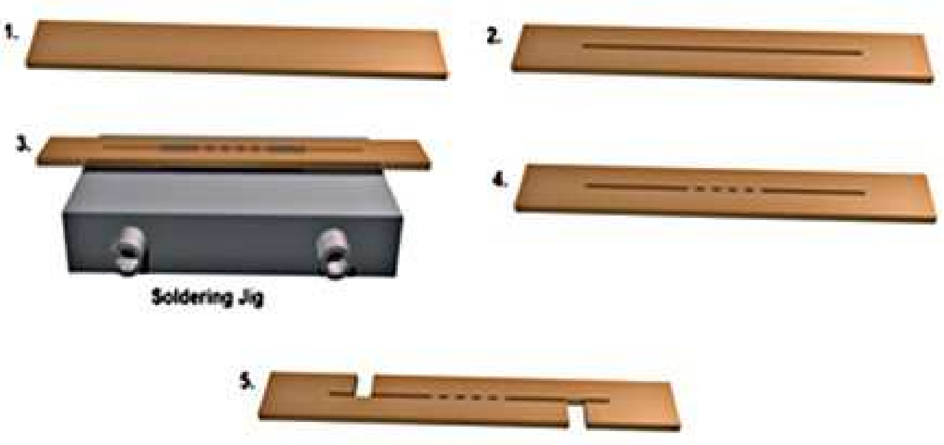

Figure 5-2 Illustration of steps during the sample preparation.

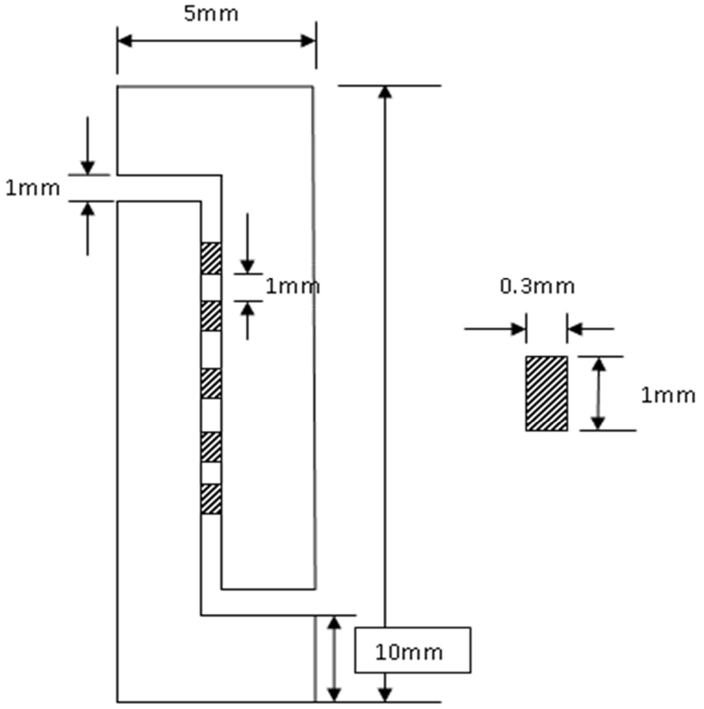

Figure 5-3 Dimensions of a five-joint specimen.

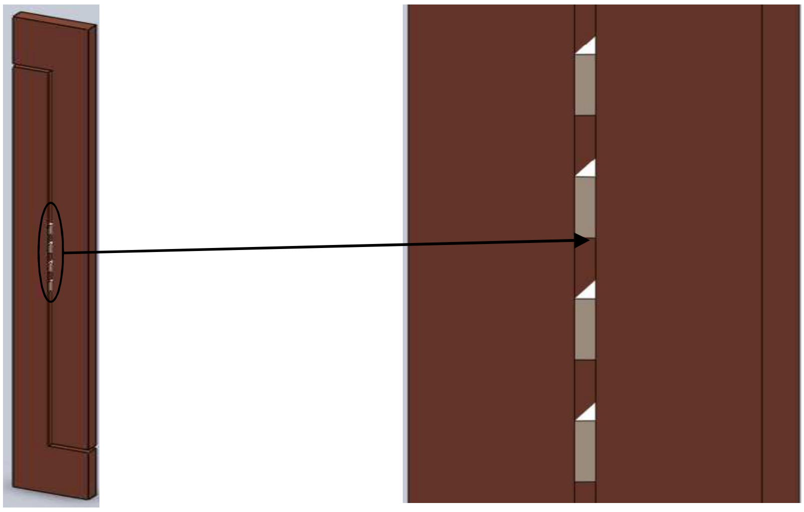

**Figure 5-4 Schematic of a four -joint specimen**

The samples were tested by applying isothermal cyclic displacement loading using the Interconnect Properties Testing Machine (IPTM) developed at the National Physical Laboratory [151, 152]. Figure 5.5 shows a 6-joint specimen mounted on the instrument.

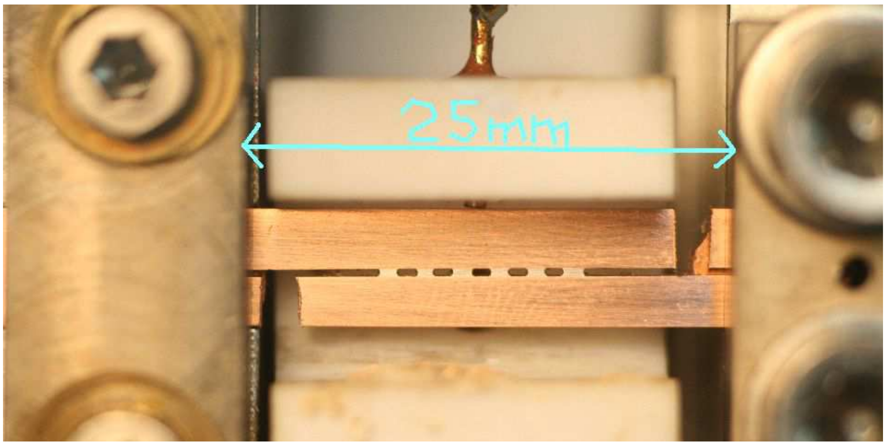

**Figure 5-5 Experimental setup for testing a 6-joint specimen.**

The two ends of a specimen were clamped and pulled/pushed along the length of the sample to produce shear dominated cyclic deformation in solder joints. A load cell was used to monitor the applied force and laser displacement sensors were used to measure the distance between the fixed and moving stages of the instrument. The displacement was controlled through the thermal expansion of a stainless steel tube connected to the moving stage. By changing the temperature of the steel tube, displacement loading can be controlled. As such, the machine can accurately control the strain applied to the sample, whilst measuring the force load. In addition, a camera with microscope attachment was placed over the sample to take time-lapse photos of the sample during the test. This level of control and monitoring would be much more difficult to achieve in thermal-cycling tests.

The range of displacement that is applied to the samples is from -30 to 30 µm. This loading results in strains that are in the same order of magnitude as in BGA solder joints under temperature cycling conditions [153]. The ramp rate is 0.1µm/s and the dwell time is 5 minutes, producing a cycle time of 30 minutes. With increasing number of solder joints, the supported force load increases and the strain in the copper also increases, whilst the strain in the solder joints is reduced because part of the strain is absorbed by the increase in the strain in copper. To produce a controlled strain in samples with different number of solder joints, the compliance of the copper needs to be taken into account when applying the displacement. To apply this correction, a copper coupon with a similar geometry but without solder joints was first tested on the IPTM. Since the stress caused by the applied force is in the elastic region of the copper, it is possible to correct the solder joints tests in real time with the maximum applied displacement adjusted to take into account the extra displacement in the copper. The applied displacement is calculated as:

$$d(t) = w(t) + kF(t) \qquad \textbf{(5-1)}$$

where $d(t)$ is the displacement applied at time $t$, $w(t)$ is the target displacement waveform, $F(t)$ is the applied force and $k$ is an experimentally determined constant compliance. With this correction, solder in samples with different number of solder joints will be subject to similar level of deformation.

## 5.2 Computer Simulation of the Tests

To address the issue caused by the compliance of the copper, Equation(5-1) is used in experiment as an idealised representation of the correction made to the displacement for the multi-joint specimen. In performing mathematical simulation the model should be representative of the physical process being modelled. During the experiment, a loading profile can be programmed into the control software, and feedback loops are then used to compare the actual displacement of the equipment with that programmed in. If they don't match, then the actual displacement is corrected to match the programmed profile. During the course of the entire experiment, constant corrections are made to match the input profile. For the simulation to correctly match the experiment the major challenge is to model the loading condition experienced by the solder joint correctly but the problem is that to apply those corrections in FEA simulations is difficult. To ensure that the loading condition is similar across the solder joints a correction factor is applied to the modelling procedure to account for the increased number of joints and this method is described in the following.

The constant, *k* in equation (5-1) is approximately 0.08 microns per Newton based on NPL experimental data. In order to perform the analysis and have loading regimes similar to that in the experiments, the waveform in simulation was adjusted based on the compliance of copper. The initial force magnitude seen from the results of NPL is given by:

$$A = 30 + kN \tag{5-2}$$

where *A* (μm) is the amplitude of the displacement waveform to apply, *N* is the number of joints in the sample and k is a constant.

The deformation Δx is given by:

$$\Delta x = \frac{FL}{EA} \tag{5-3}$$

Assuming that the two different materials are connected as shown in figure 5-6, the total displacement is given by:

$$\Delta x = 2\frac{FL_1}{E_1A_1} + \frac{FL_2}{E_2A_2}$$

which rearranges to

$$\Delta x = F\left(\frac{2L_1}{E_1A_1} + \frac{L_2}{E_2A_2}\right) \tag{5-4}$$

From experiment it was determined that $F = 32N$, where $N$ is the number of joints. Equation 5-7 then becomes:

$$\Delta x = 32N\left(\frac{2L_1}{E_1A_1}+\frac{L_2}{E_2A_2}\right) \tag{5-5}$$

This maximum applied displacement is therefore directly proportional to the number of joints in the sample. After substituting the various parameter values, the revised maximum displacement for specimens with different number of solder joints are shown in Table 5-1.

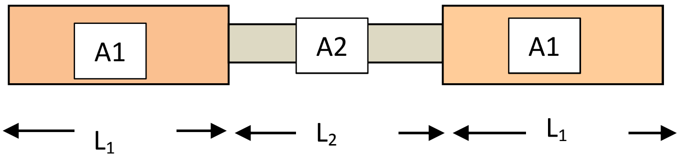

**Figure 5-6 Simplified structure of the specimen**

**Table 5-1 Calculated maximum displacement loading of specimen**

| $N$ | 1 | 2 | 3 | 4 | 5 | 6 | 7 | 8 |
|---|---|---|---|---|---|---|---|---|
| Δx(μm) | 2.44 | 4.88 | 7.32 | 9.76 | 12.20 | 14.65 | 17.09 | 19.53 |
| dU_max(μm) | 32.44 | 34.88 | 37.32 | 39.76 | 42.20 | 44.65 | 47.09 | 49.53 |

The above displacements in Table 5-1 are used during the finite element simulations. The maximum displacement of the samples from experiments matched quite closely the numerical result in Table 5-1 with the suggested correction. In Figure 5-7, the load-displacement curves in the experiment on a four-joint model are shown and maximum displacement is about 0.04 mm or 40 microns which is very close to the value of 39.76 microns shown in Table 5-1.

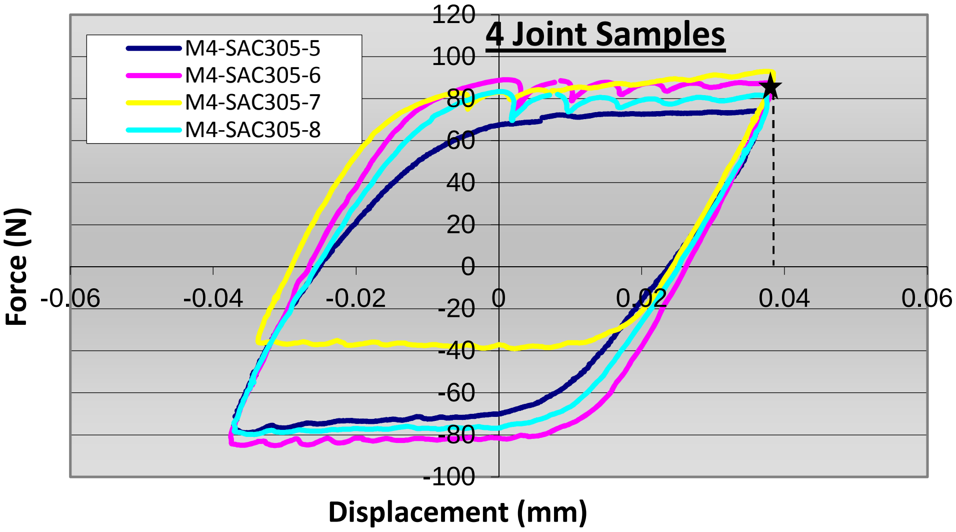

**Figure 5-7 Hysteresis loop for 4-joint samples.**

### 5.2.1 Loading Condition

The displacement loading of 30μm (before correction) was applied to one end of the specimen as the other remains fixed (figure 5-8).

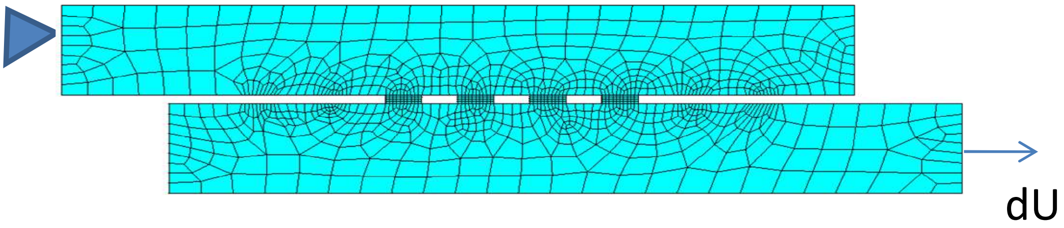

**Figure 5-8 Numerical model of the specimen and loading conditions.**

The loading profile is as shown in figure 5-9. A loading cycle of 30 minutes with two 5-minutes dwells at a strain rate of $2x10^{-6}$ $s^{-1}$ at the maximum and minimum displacement extremes. The displacement loading after correction for copper deformation are shown in figure 5-10.

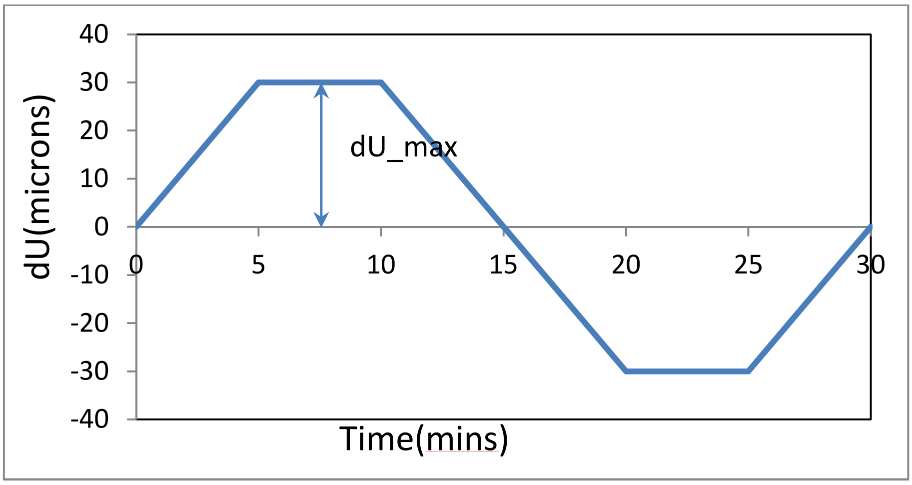

**Figure 5-9 Loading profile applied to specimen.**

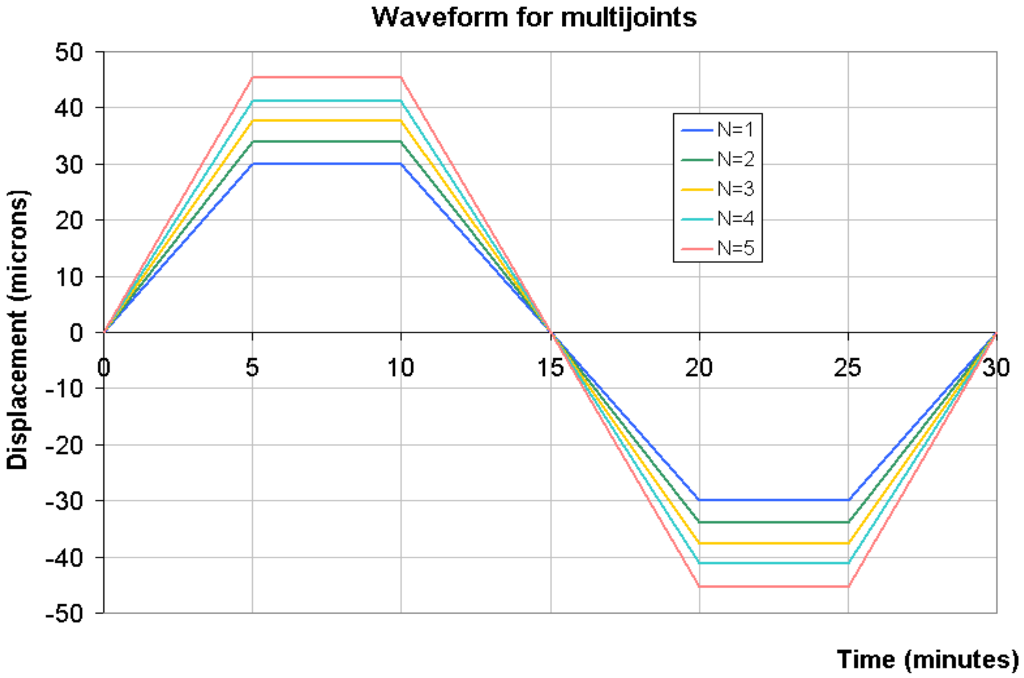

**Figure 5-10 Corrected loading profile with compliance correction**

In the current experiments, solder joint shape may deviate from the expected cuboid shape. In order to understand the effects of geometry on the stress state in solder joints, three different solder interconnect shapes are modelled: flat, convex and concave shapes (illustrated in figure 5-11).

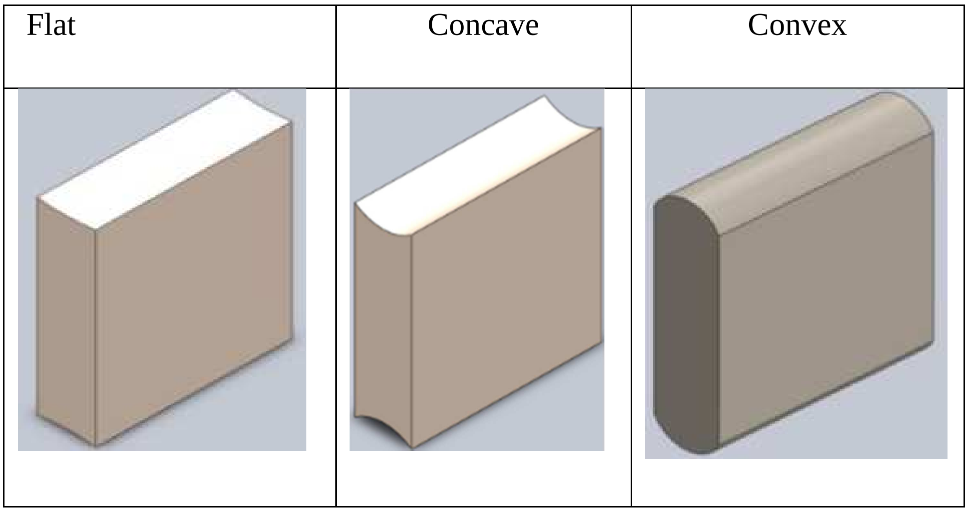
Flat Concave Convex

**Figure 5-11 Solder joint shapes investigated.**

### 5.2.2 Material properties for FEA Simulation

The tests have been simulated using Finite Element Analysis (FEA) software ANSYS® Mechanical APDL [144]. Figure 5-12 shows the model of a sample with 6 solder joints.

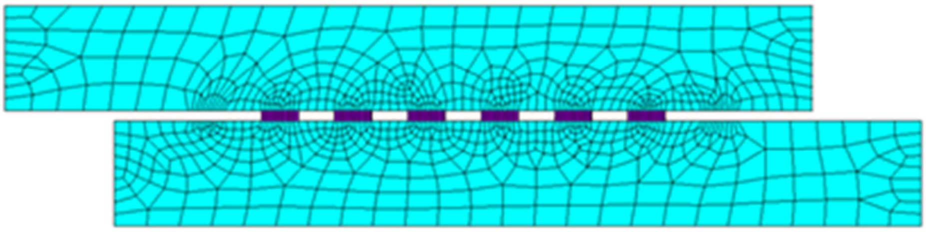

**Figure 5-12 Representative six joint model.**

Since solder has high homologous temperature even at room temperature, the effect of creep is significant and should be taken into account in the simulation. In this study the Garofalo's creep model is used to simulate the effect of creep in solder specimens and the creep strain rate equation is shown in Equation 5-6.

$$\dot{\varepsilon}_{cr} = c_1\left[\sinh\left(c_2\sigma\right)\right]^{c_3}\exp\left(-\frac{c_4}{T}\right) \qquad \textbf{(5-6)}$$

where $c_1$, $c_2$, $c_3$ and $c_4$ (see Table 4-1) are material constants, $T$ is the temperature, σ is the effective stress and $\dot{\varepsilon}_{cr}$ is the creep strain. The elastic material properties used for the simulations are as shown in Table 5-2.

**Table 5-2 E and ν are Young's modulus and Poisson's ratio respectively [18].**

| Material | E (GPa) | ν |
|---|---|---|
| Sn3.0Ag0.5Cu | 50 | 0.4 |
| Copper | 120 | 0.33 |

## 5.3 Results and Discussions

In the tests, each sample was subject to cyclic loading until the load dropped to 50% of the maximum supported load. Figure 5-13 shows how the load changes for three five-joint specimens. The variability in the rate at which the load drops for samples of the same type is mainly caused by the statistical nature of the fatigue process [154], variation in solder joint geometry, voids and defects in the samples. Optical micrographs of the fatigue damage produced in some of the five-joint (M5) samples are shown in figure 5.14.

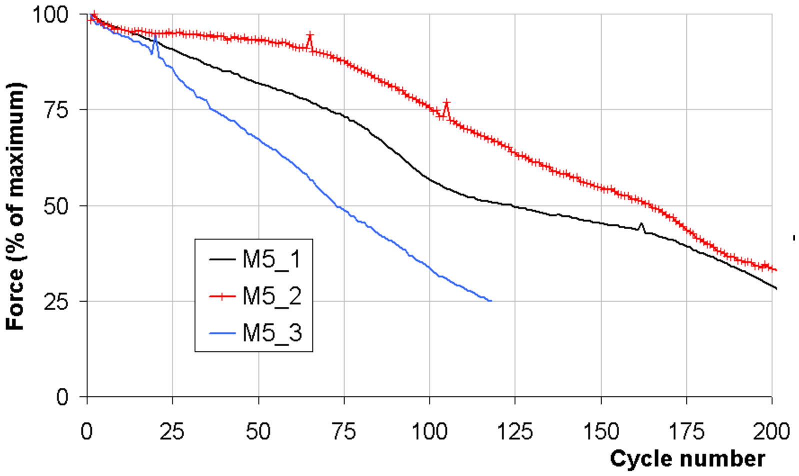

**Figure 5-13 Force drop (as % of maximum) vs. cycle number for M5 samples, i.e. five-joint samples.**

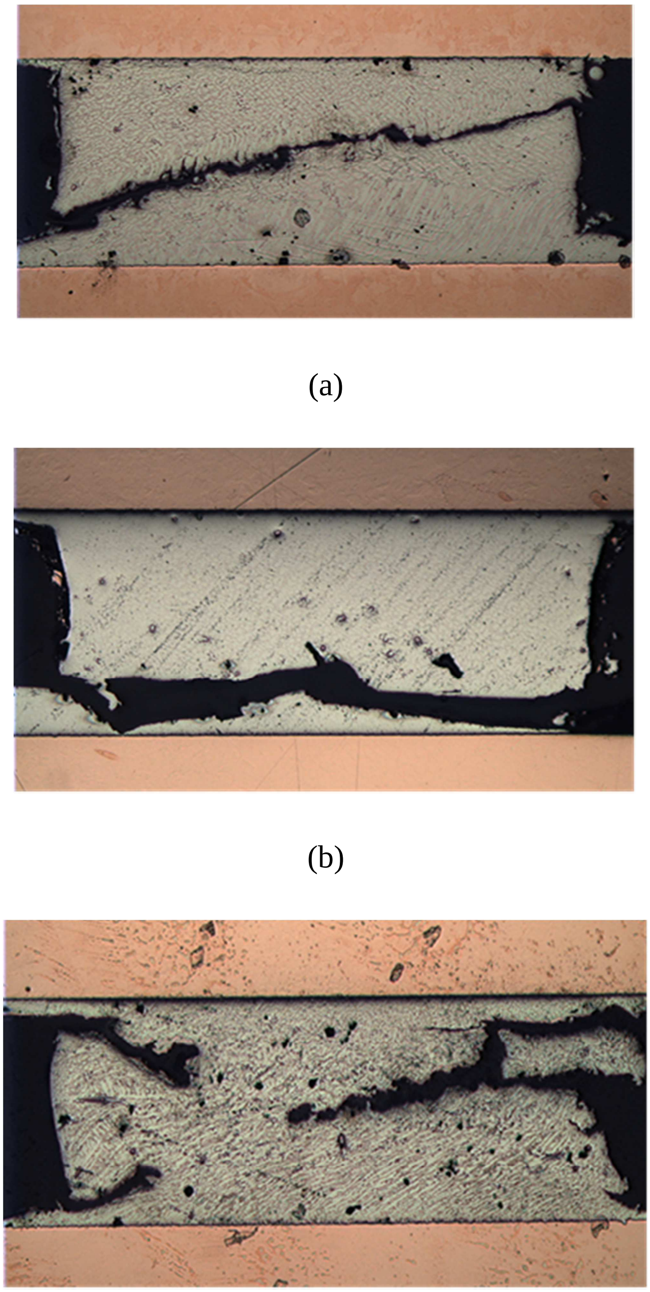

(a)

(b)

(c)

**Figure 5-14 : (a) Crack in the central joint of a M5 sample; (b) crack in the third joint of a M8 sample (c) multiple cracks in an M5 sample and crack along the interface.**

In the simulation, stress and strains are obtained. Figure 5-15 shows the effective stress as a function of time at the corner of one of the outermost solder joints in an M5 convex sample.

It shows that the stress changes with time, which is shown in figure 5-15, and the stress is highest just before the onset of dwell times at 300s, 1200s and etc.

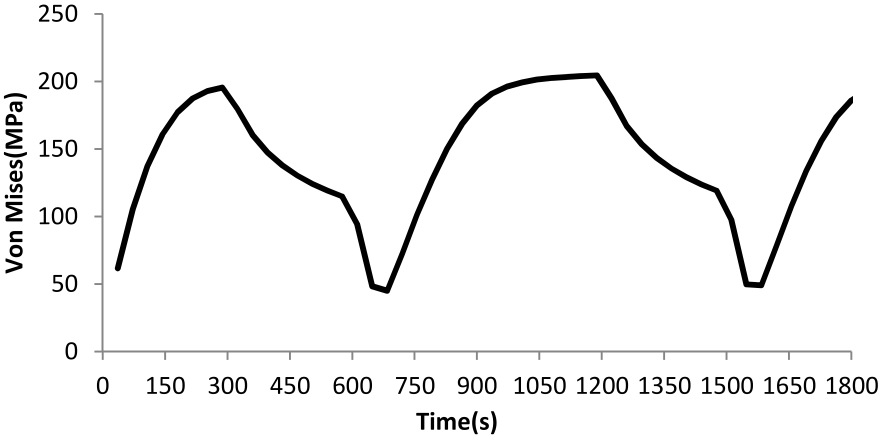

**Figure 5-15 Von Mises stress at the corner of an edge solder joint of a 5-joint model**

Figure 5-16 shows the Von Mises and shear stress distribution in the M5 sample at t=2088 s. The maximum stress is located at the solder-copper interface of the outermost solder joints. Because of the stress relaxation, the stress level in solder joints exhibits much less inhomogeneity than in copper. The shear stress is concentrated in solder joints but it is not uniformly distributed. As the figure shows, the copper parts bend slightly under the loading and deformation in the solder joint is therefore not pure shear and stress states are expected to vary from one joint to another. At the outermost solder joints, deformation occurs in the direction perpendicular to the loading as well because of the bending of copper.

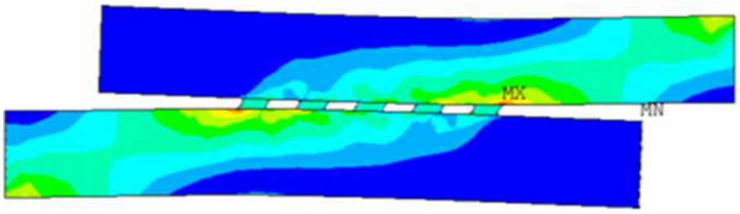

(a)

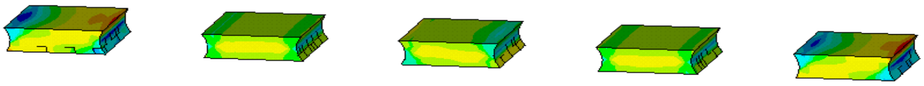

(b)

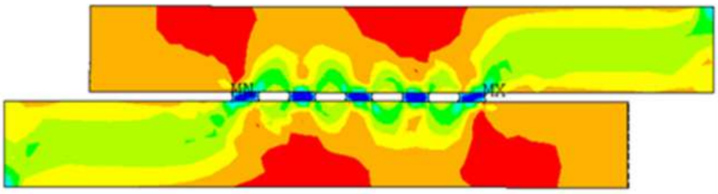

(c)

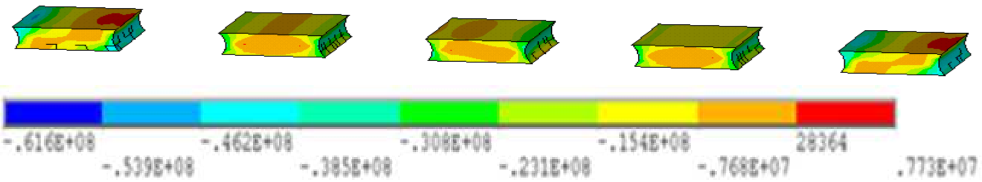

(d)

**Figure 5-16 (a-b) Von Mises Stress of specimen and solder and (c-d) Shear Stress XY $\sigma_{xy}$ of specimen and solder in a modelled 5 joint sample at the start of the first dwell at 30 µm displacement (in Pa). Displacement in image (a-b) has been magnified 20 times to make the deformation more prominent.**

This stress/strain states in these solder joints are similar to what happens in BGA solder joints under thermal-mechanical loading when the package experiences expansion/contraction and warpage as temperature changes. For reliability evaluation of solder alloys this similarity is desirable because it makes the isothermal cyclic testing more realistic. Another interesting phenomenon that can be observed is a diagonal shear band, in the edge solder joints in particular.

The distribution of the accumulated creep strain $\varepsilon_{ac}$ (ANSYS® output variable NLCREP) is a measure of the damage in solder joint and it can be linked to the solder joint lifetime through an empirical Coffin-Manson type lifetime model [155]. The distribution of the accumulated creep strain for the concave shape solder joints is shown in figure 5-17 and they give a failure matrix for the solder joint. The path of highest accumulated creep strain is similar to the crack path from experimental results as shown on the micrograph images (figure 5-14).

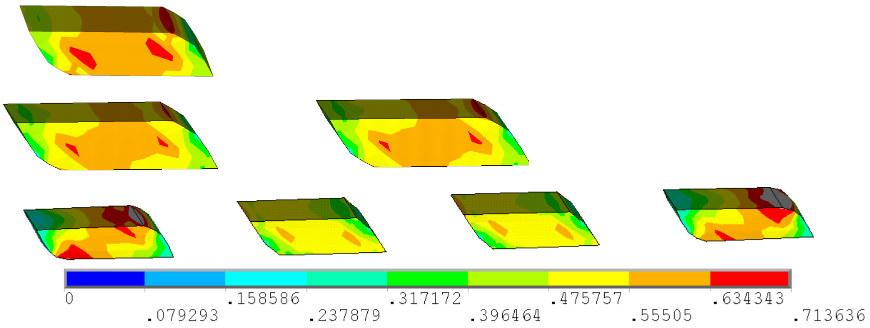

**Figure 5-17 Accumulated creep strain at end of the third cycle**

A typical accumulated equivalent creep strain value as a function of time is shown in figure 5-18 for the first three cycles of loading.

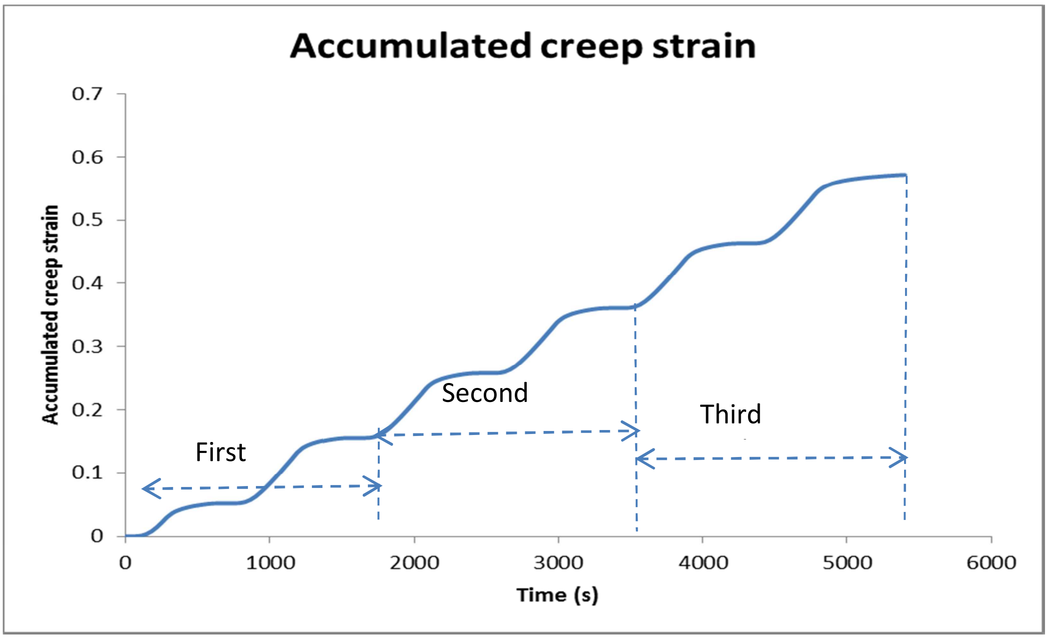

**Figure 5-18 Accumulated creep strain over three cycles for five sample solder joint**

The increase of $\varepsilon_{ac}$ per cycle is $\Delta\varepsilon_{ac}$. Its values have been obtained in the simulation as the damage indicator because it's often linked to fatigue lifetime in reliability analysis in solder joints. The value of $\Delta\varepsilon_{ac}$ changes from one cycle to the next but from the third cycle it becomes almost a constant. The higher the $\Delta\varepsilon_{ac}$ the shorter the life time.

Specimens with different number of joints have been investigated. The results suggest that solder joints with concave shape will have less damage and hence longer lifetime than those with convex or rectangular shape.

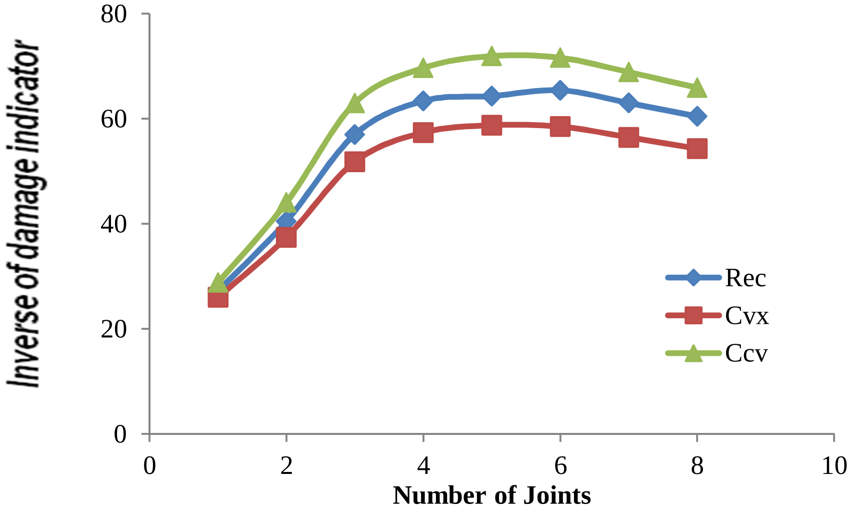

**Figure 5-19 1/$\varepsilon_{acc}$ vs. number of joints in the sample for the rectangular (Rec), convex (Cvx) and concave (Ccv) solder joint shapes.**

In figure 5-19, the values of the inverse of the damage, i.e. $1/\Delta\varepsilon_{ac}$, for each individual solder joints are plotted. The results show that outermost solder joints suffer more damage than internal ones and will therefore fail first.

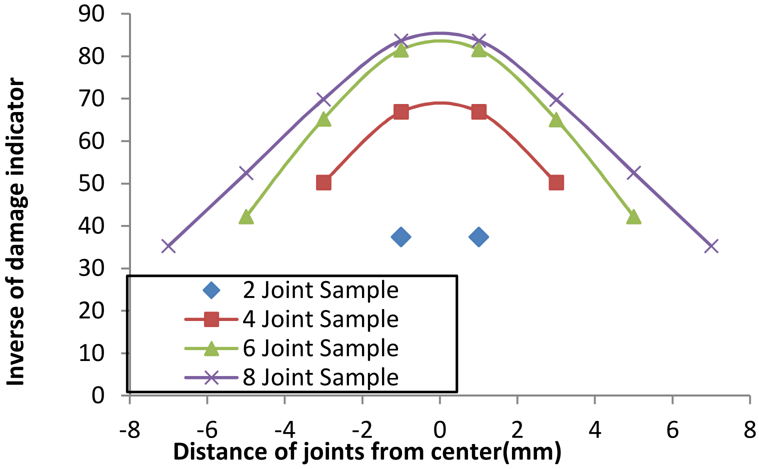

(a)

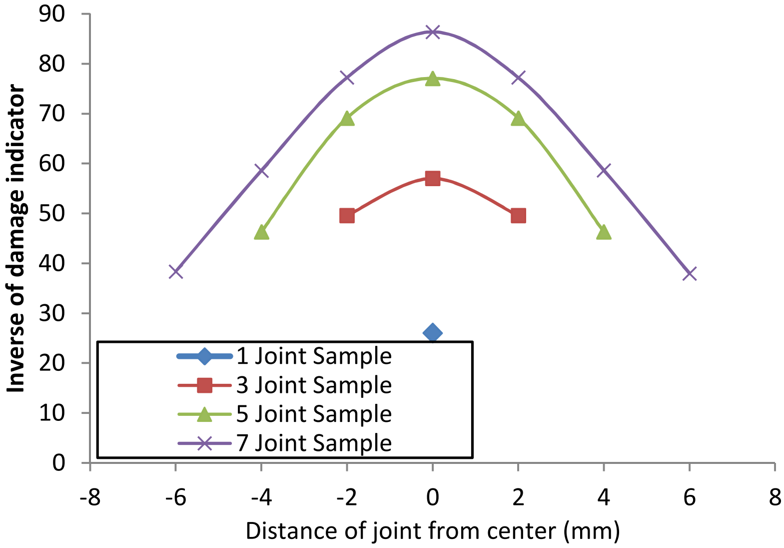

(b)

**Figure 5-20 The (inverse) damage for samples with (a) even and (b) odd number of solder joints. Higher value corresponds to longer lifetime**

Figure 5-20 also shows that in general, samples with different number of joints have different average damage. This is confirmed by figure 5-21 where the average damage is shown for samples with 1 to 8 joints. The result indicates that under the loading conditions that were set out in this work, the single joint sample will be the most damaged of all the multi-joint models and that the least damaged will be the M5 sample, while M4 and M6 have similar results.

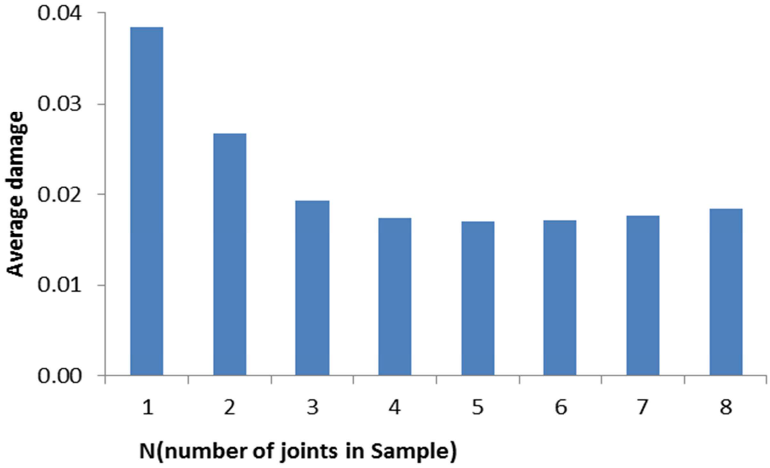

**Figure 5-21 Average damage in samples with N number of joints.**

The experimental results for the number of cycles required to reach 10%, 20% and 50% of load drop from the maximum load, are plotted in figure 5.22 against the number of joints per sample. The relationship between the number of joints and the cycles to reach a pre-defined failure is not that clear but it show that the sample with the longest lifetime is the M5, which is consistent with the simulation result.

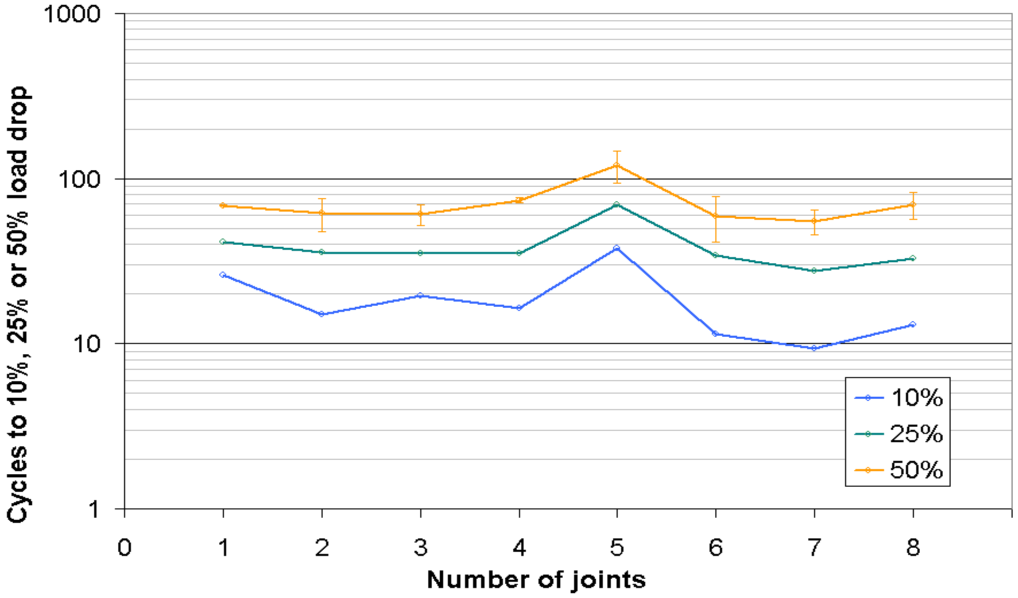

**Figure 5-22 Cycles to 10%, 20% and 50% force drop vs. number of joints in sample. Error bars on the 50% load drop data represent the repeatability observed from testing on average 3 samples for each number of joints.**

Using the time-lapse photography technique, 4 main different types of failure/crack propagation mechanisms were identified in experiments that have been carried out at NPL. Type 1 consists of a crack that runs diagonally across the sample as in figure 5-14(a). Type 2 consists of a crack that runs parallel to the interface, as in figure 5-14(b). Type 3 consists in a crack along or very close to the interface (figure 5-14(c)). This is similar to what Lai et al have found in their study [156]. Finally, type 4 is a surface damage that causes the solder to appear darker but without any visible crack.

The initiation of the crack was also not univocal; sometimes cracks initiated in one place, sometimes in several places, with multiple cracks growing and combining as the sample becomes more damaged (see figure 5-14(c)).

From these experiments, it was observed that generally, voids in the solder bulk aided the propagation of cracks confirming the findings of Yunus et al. [157]. Cracks propagated in all joints almost simultaneously, with minimal changes in crack propagation rate between different joints. However, a tendency for the outer joints to fail first compared to the inner joints was also observed, which is consistent with the simulation results. Although the prediction of the experiment and finite element analysis are similar there were areas of discrepancies. To this end X–ray images were taken of the solder joints and they show a large number of voids within the solder joints and these voids inevitably affect failure processes. Modelling these effects may be carried out either by explicitly include voids in FEA models, which is extremely time consuming, or by using constitutive models that incorporates the voids distribution and density while the solder joints are still treated as single phase material.

## 5.4 Conclusions

The computer simulation work has shown that solder joints experience both shear and normal stress of appreciable magnitude under the prescribed loading conditions. The stress states in the multi-joint test samples are similar to those in BGA solder joints under temperature cycling loading and solder joints are exposed to different stress states, both direct and shear. The samples that have 5 solder joints are predicted to have the longest lifetime. The most significant difference between the modelling results and the experimental results is that in experiments, samples with one or eight solder joints are not the ones that have the shortest lifetime. This needs more investigation. In future work, lifetime models will be derived based on experiments on the solder joint specimens so that the number of cycles to failure can be predicted for the solder joints.

The results demonstrated that the simulation predicts the regions of likely failure and this is verified by experiment. The influence of voids, which affects the strength of the solder, also has a significant effect on the overall behaviour of the specimen.

Creep is modelled using Garofalo's steady state creep model. The model parameters are from the literature and this may incur inaccuracy in the modelling because test conditions and alloy composition may be different to certain degree. This issue can be addressed using the methodology that will be discussed in Chapter 6.

# Chapter 6 Inverse Modelling of Lead-free Solder Joint

## 6.1 Introduction

Considerable research has been undertaken to find lead-free solders that can serve as drop in replacements for SnPb solder. The Sn-Ag-Cu (SAC) ternary composition is the combination of choice for many microelectronics applications and has been studied extensively by researchers in industry and research institutions. Though there is now a large body of theoretical and experimental work on it the exact composition used in electronics manufacturing varies according to areas of application and supplier. In this work, the properties of 96.5Sn3Ag0.5Cu (SAC305) alloy [158, 159], which is one of the commonest lead-free solder is studied. There have been many studies on the determination of the material properties of lead free solder [160-163] and the results have been used in computer modelling of solder joints. However, the results of these material properties seem widely different partly due in part to the experimental conditions, quality of the joints, specimen geometry variations, loading conditions, and a variety of other controlled and uncontrolled variables (see Appendix C). Therefore it should be understood that using those material properties is an approximation and it may not be suitable for the particular situation that is simulated. For example, the material properties reported in many studies [164-166] where the tests were performed using bulk solder, the results are generally not applicable to very small solder specimens as is the case in this work. This is due in part to the microstructure in solder joints. According to [167] a BGA created from SAC can have a single crystal or between 8 and 12 grains this indicates therefore that the interactions of the large number of grains in the bulk sample as compared to the test sample affect the material properties and may explain why they will be different. For solder joints of similar size, microstructures may also be different because of the variables in the fabrication process: for example, because the formation of intermetallics compounds is strongly dependent on cooling rate. It can be concluded that in order to obtain solder material properties that can be used to describe all solder joints the material model has to include constants that describe the effects of geometry, microstructure, and possibly many other factors. Before a material model can be developed using the laws of physics at the microscopic scale, a universal solder material model is bound to be in such a complicated form that an unrealistically large number of experiments have to be carried out to obtain it. In order to solve this problem and provide solder data models for reliability analysis, a change in the direction in this area of work is needed. Instead of aiming at universal material models, “bespoke” ones that are quick to obtain and simple to apply can be constructed for solder joints with particular types of geometry, microstructure, and loading conditions for a particular purpose. This approach would enable industries which have limited resources in research to develop the capability of modelling solder joints for reliability analysis.  In this work, inverse FEA is used to obtain solder material models for reliability prediction of the solder joint isothermal mechanical tests described in the previous chapter.

Engineering problems can often be described by partial or ordinary differential equations (PDE or ODE) with unknown field variables. In most applications, the independent variables are solved and this type of analysis is called “forward”. In this type of analysis, the problem domain is known beforehand and the solution to this direct problem is to solve the PDE or ODE subjected to the initial or boundary conditions. Many numerical methods have been developed over the years to solve these problems such as the finite difference method, the finite element method, boundary element method and mesh-free method. With the exception of the mesh-free method, all the above methods are well established methods in the solution of direct problems. These methods rely on knowing the material properties, the geometric configuration of the structure, the loading profile, the initial and boundary conditions. The result set thus includes amongst other solution parameters the stresses and strains in the structure. A schematic demonstrating the difference between forward and inverse problems is shown in figure 6-1.

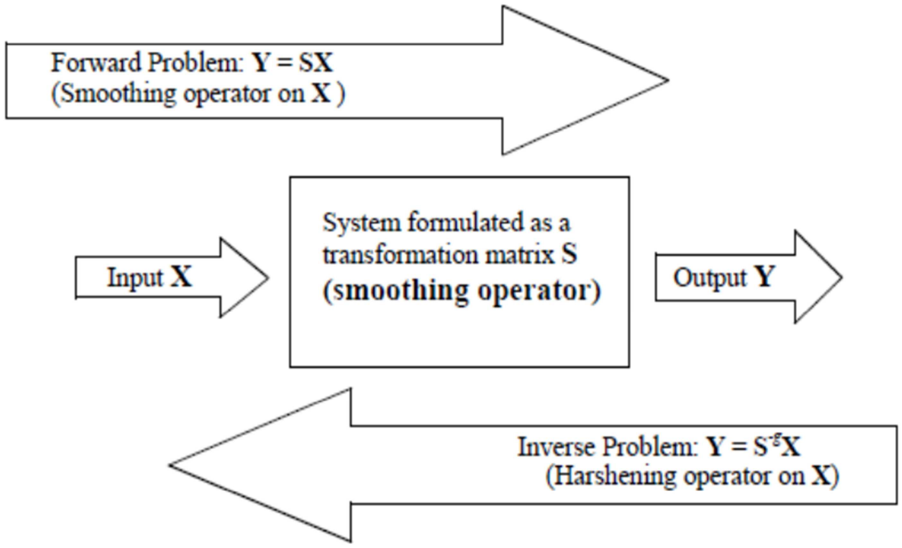

**Figure 6-1 Illustration of forward and inverse problem [168]**

A “forward” solid mechanics problem’s main goal is to determine the response of a structure whilst all other parameters are known. In inverse problems, the response of the structure, through experiments, is known (such as the displacement, velocity, force, acceleration, etc.) but the loading profile, material properties, boundary conditions, or a combination of these may not be known. These types of problems, unlike the direct problems, are extremely difficult to solve for many applications. The nature of inverse analysis is such that the problem can be ill-posed, under-posed or over posed [168] and in some situations there is no solution. To illustrate the concept of inverse modelling as compared to forward modelling techniques a simple example is given below

## 6.2 Inverse Analysis – an Example

If one considers a system of a straight bar of area *A*, Young’s modulus *E* and length *l* subjected to forces $f_1$ and $f_2$ as show in figure 6-2. If the displacement of the bar at nodes 1 and 2 are $u_1$ and $u_2$ respectively, the governing equation is written as:

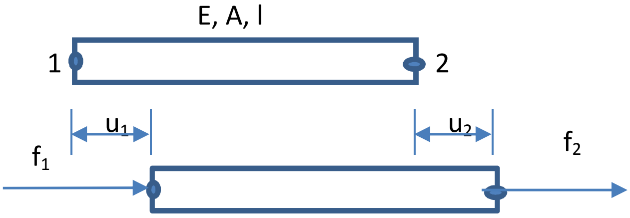

**Figure 6-2 Displacement of a straight bar**

$$\begin{bmatrix} \frac{EA}{l} & -\frac{EA}{l} \\ -\frac{EA}{l} & \frac{EA}{l} \end{bmatrix} \begin{Bmatrix} u_1 \\ u_2 \end{Bmatrix} = \begin{Bmatrix} f_1 \\ f_2 \end{Bmatrix}$$

**(6-1)**

$$\begin{bmatrix} k & -k \\ -k & k \end{bmatrix} \begin{Bmatrix} u_1 \\ u_2 \end{Bmatrix} = \begin{Bmatrix} f_1 \\ f_2 \end{Bmatrix}$$

$$where\ k = \frac{EA}{l}$$

The above can be written in matrix form as

$$[K]\{U\} = \{F\} \qquad \textbf{(6-2)}$$

where [K] is the stiffness matrix, {U} the displacement vector and {F} the force vector.

For the direct problem *E*, *A*, *l* and $f_i$ are known, the only unknowns are the displacement {U}. To avoid singularity, if we apply a boundary condition $u_1$=0 a unique solution for the displacement is calculated to be

$$\text{Since } u_1 = 0$$
$$-ku_1 + ku_2 = f_2 \qquad \textbf{(6-3)}$$
$$u_2 = \frac{f_2}{k}$$

If we consider the case now that through experiments the displacement $u_2$ is known but the Young's modulus E is to be determined, then from (Equation 6-2) above we get

$$\begin{aligned}&ku_2 = f_2\\&but\ k = \frac{EA}{l}\\&E = \frac{lf_2}{Au_2}\end{aligned} \qquad \textbf{(6-4)}$$

Therefore the solution for the Young's modulus using the experimental results and the input parameters is therefore determined. The simplicity of the above formulation makes the solution straight forward without resorting to the use of special techniques/methods to arrive at a solution.

To understand the case of ill-posed problems, consider a simple continuous system equation that governs the static state of the simple bar problem examined in section above

$$\frac{du(x)}{dx} = \frac{f_2}{EA} \qquad \textbf{(6-5)}$$

The boundary condition for this problem is given by equation (6-3) as shown in figure (6-2). The conventional direct problem is to solve the axial displacement u via the following integral operation

$$u(x) = \int \frac{f_2}{EA} dx + c_0 \qquad \textbf{(6-6)}$$

where $c_0$ is the integral constant to be determined by the boundary condition equation (6-3)

Now, to estimate $f_2$ using displacement u(x) measured at x that is an internal point in the bar. In a practical situation of measurement, there will be an error or noise that can be expressed in the form of

$$\begin{aligned}u^m &= u^a + u^{noise} = u^a + u^a e \sin(\varpi_{noise} x)\\u^m &= u^a[1 + e\sin(\varpi_{noise} x)]\end{aligned} \qquad \textbf{(6-7)}$$

where the superscript *m* stands for the measurement data, *a* stands for the result being analytical or exact, *e* is the noise level that is usually relatively smaller than 1, and $\omega_{noise}$ is the frequency of the noise distribution along x. In the inverse analysis, $u^a$ is not known; only $u^m$ is known. To view the error more clearly in graphs, simplify the problem by assuming

$$l=1.0,\ \ EA = 1.0,\ \omega_{noise} = 10\pi,\ e = 0.01 \tag{6-8}$$

which implies a 1% measurement error relative to $u(x)$, which is, in fact, a very good measurement. However, the frequency of the measurement data is high, which is also very common in the measurement errors.

Using the parameters given in equation (6-8), the exact solution of $u$ becomes

$$u^a = x \tag{6-9}$$

The simulated measurement is

$$u^m = u^a + u^{noise} = x[1+e\sin(10\pi x)] \tag{6-10}$$

which is plotted in figure 6-3 together with the exact displacement. It is shown that the measured displacement is indeed very accurate.

Use of this erroneous result in equation (6-5) for the inverse predication of force can result in a magnification of errors. This magnification of error causes the instability in the inverse analysis procedure. To demonstrate this, substitute equation (6-7) into equation (6-5) to obtain

$$\frac{du^m}{dx} = \frac{du^a}{dx}[1+e\sin(\varpi x)] + u^a\varpi_{noise}e\cos(\varpi_{noise}x) = \frac{f_2^e}{EA} \tag{6-11}$$

where the superscript e stands for the estimated value. Therefore, $f_2^e$ can be inversely determined by

$$f_2^e = \underbrace{EA\frac{du^a}{dx}}_{f^a}[1+e\sin(\varpi x)] + EAu^a\mathrm{e}\quad \underbrace{\varpi_{noise}}_{\text{factor of magnification}}\quad \cos(\varpi_{noise}x) \tag{6-12}$$

It can be clearly seen that the error in the inverse solution is magnified drastically by $\omega_{noise}$ times. For parameters given by equation (6-8) using equation (6-12) yields

$$f_2^e = f_2^a[1+0.01*\sin(10\pi x)] + \underbrace{10\pi}_{\text{factor of magnification}} 0.01*\mathrm{x}\cos(10\pi x) \qquad \textbf{(6-13)}$$

The results of the estimated force for the unit true force are plotted in figure 6-4. The magnification of errors is clearly evidenced. This magnification is obviously caused by the differential operation in the system equation.

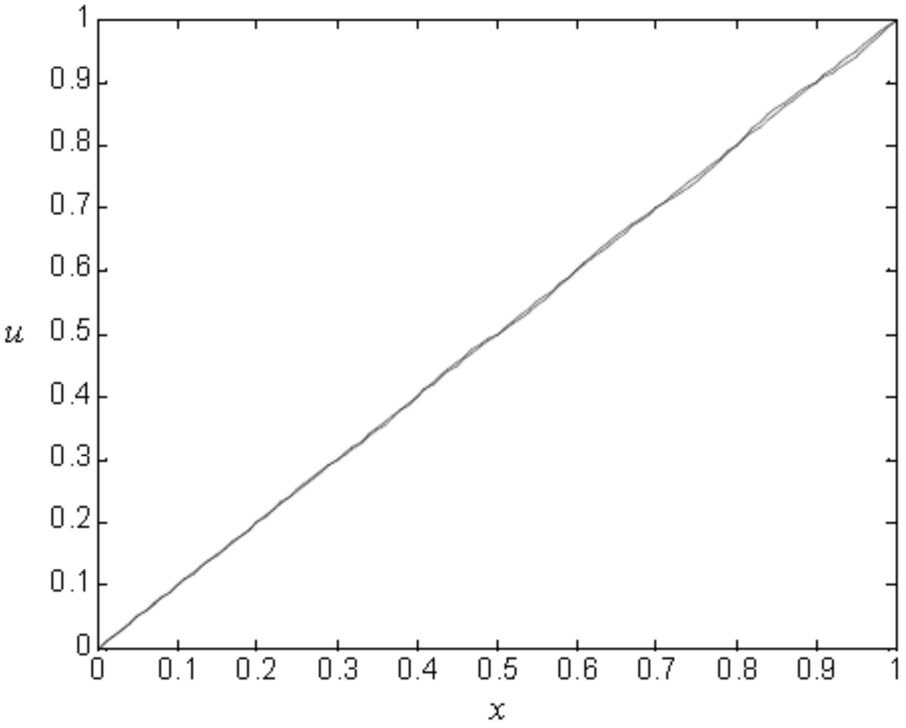

**Figure 6-3 The displacement in a clamped uniform bar subject to a force at the free end. Comparison of the exact result (dashed line) and the simulated-measurement (solid line) with 1% oscillatory error.**

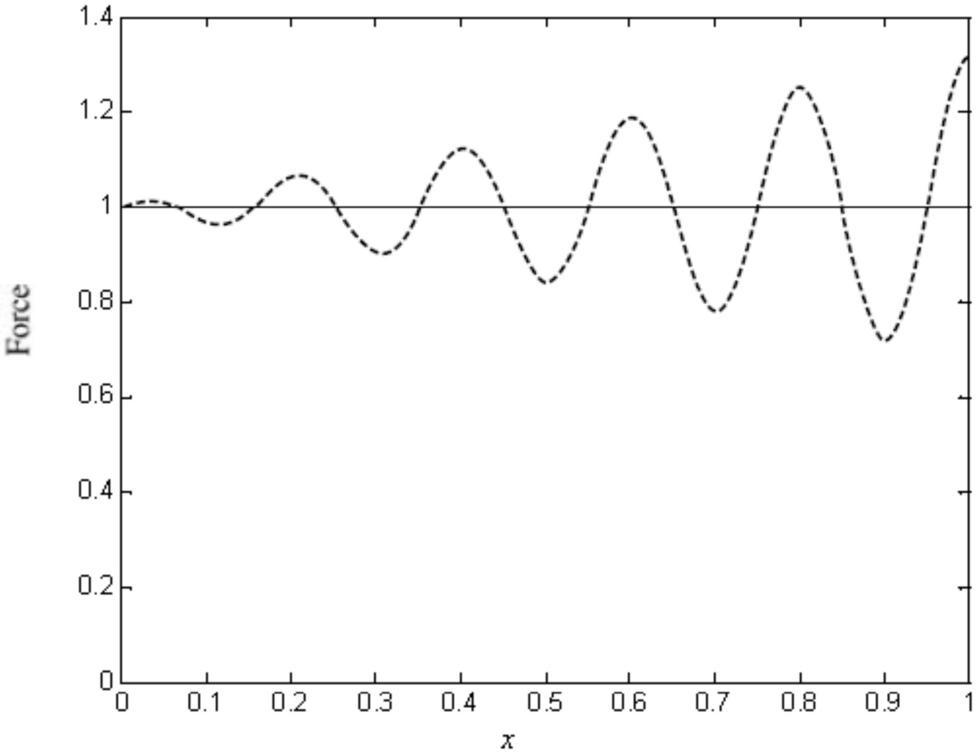

**Figure 6-4 Inverse solution of the force (dashed line) applied on the clamped uniform bar using the simulated measurement of displacement with 1% oscillatory error compared with the true force (solid line).**

## 6.3 Inverse FEA for the Determination of Solder Creep Parameters

The aim of this work is to use inverse analysis to find solder properties, or more specifically, the creep strain rate model parameters so that the strain-stress hysteresis loop that is predicted using (forward) FEA matches that in the experiment that is described in Chapter 5. The methodology can be summarised as the following steps. (1) Carry out a test on solder joint samples and obtain the force-displacement data for the required period of time, (2) Process the data to reduce the noise level, (3) Create an FEA model of the tests using the Garofalo or Anand's visco-plastic/creep laws for the strain rate in solder, and (4) use inverse FEA to identify the parameters in the strain rate model that optimise the likeliness of the simulated force-displacement curve to experimental data.

## 6.4 Curve Smoothing

The first step in performing parameter estimation is to perform smoothing of the experimental dataset to remove errors inherent in the result. These errors that are inherent in the dataset are due to but not limited to random errors, systematic errors, epistemic error, etc. there is therefore a need for performing a smoothing operation to eliminate or reduce to a minimum its effect on the dataset. The noise in the experimental results are generated due to the correction been made by the equipment during the course of the experiment. A loading profile is programmed into the equipment and using feedback control the equipment is constantly comparing its true position with that of the loading profile at any time and correcting its position. This constant correction is the source of the noise as seen in figure 6-5.

To address the issues of experimental noise in the results, curve smoothing techniques are applied to reduce noise artefacts. Curve smoothing techniques are used to smooth the experimental dataset in order to create an approximate function that captures the most important trend in the data, while leaving out noise and other phenomena. After smoothing of the data, an approximate function is fitted to the smooth data allowing for comparison of the finite element result with that of the experiment, further analysis is thus performed using this curve. There are several smoothing algorithms in the literature used by different researchers; of these the most popular are the moving average, filters and the Savitzky-Golay methods [169], comparative plots using these methods are shown in figure 6-5 and a zoomed out section is shown in figure 6-6. The approximated curve generated for comparison with the finite element analysis is shown in figure 6-7.

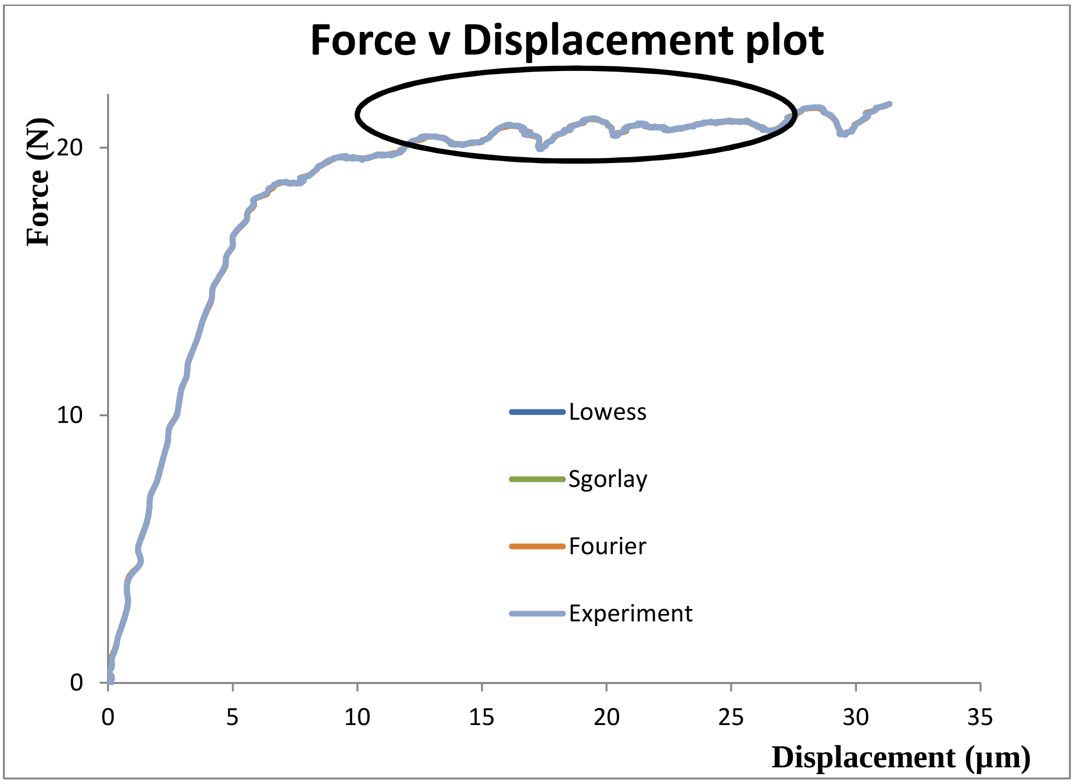

Figure 6-5 Plot of different smoothing techniques applied to the experimental data

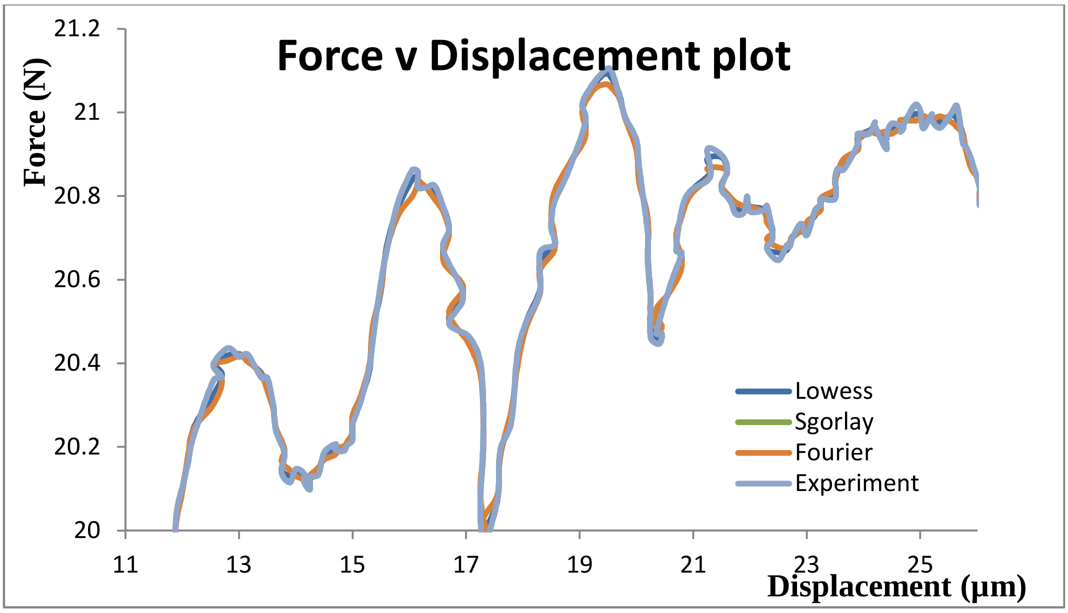

Figure 6-6 Zoom of highlighted section

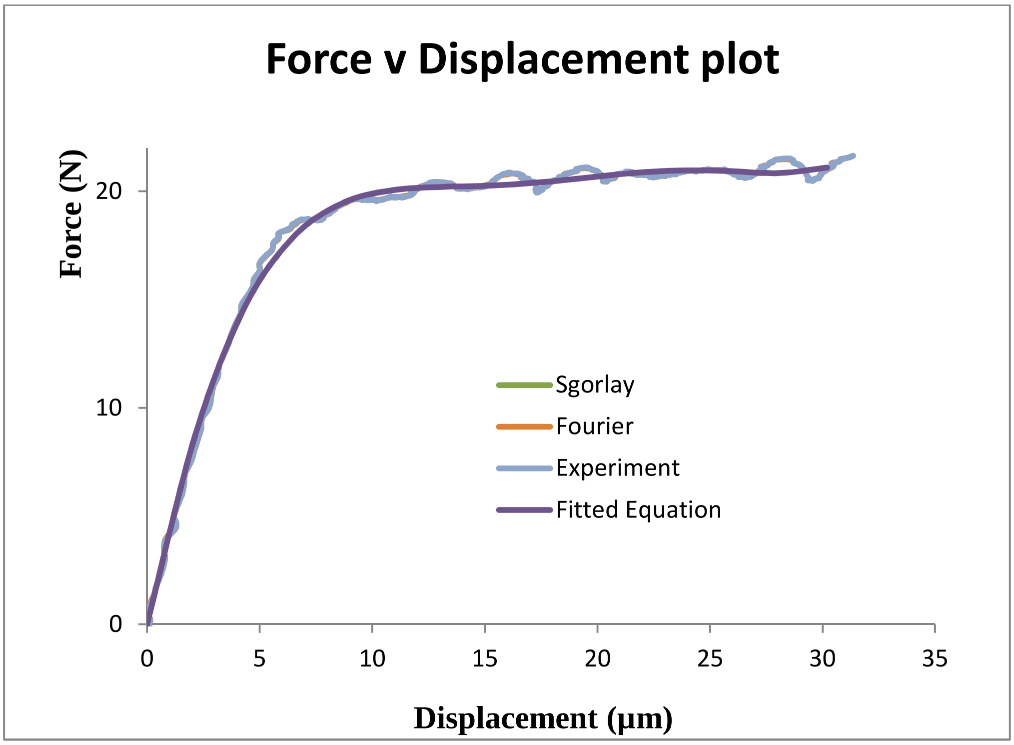

**Figure 6-7 A comparison between experimental data and the approximate model**

The differences between the various smoothing techniques used were minimal. A curve smoothing method using Fourier transform (Appendix A) was also applied but the result obtained were not superior to that of the traditional curve smoothing techniques such as filtering, moving average, Savitzky-Golay, etc.  Though the Fourier method produced a smoother graph than the other methods, it underestimates the output. This analysis is thus performed using the Savitzky-Golay smoothing technique. The approximated equation generated from the smoothed data is used to generate matching data points for comparison with the data obtained by means of finite element simulation.

## 6.5 Visco-plastic/Creep Models for Solder Alloys

The phenomenon of Visco-plasticity/Creep is discussed in depth in section 2.4. The two creep strain rate models that have been analysed in depth by many researchers performing creep modelling are the Garofalo and Anand’s creep models, which account for combined visco-plasticity and creep strains in solids. The Garofalo’s creep model is easy to implement as it only requires four parameters that have a wide representation and scatter in the literature. The Anand’s model has nine parameters and these parameters have high variability in the literature making their determination application dependent. Simulations using both models will be performed using both models but particular emphasis will be on using the Anand’s model.

### 6.5.1 Estimating Parameters of the Anand’s viscoplastic model

To model solder joint specimens using FEA, the Anand’s viscoplastic strain rate model can be used to describe their viscoplastic/creep behaviour [170]. This model is commonly used for large, isotropic, viscoplastic deformations for solders [171-173]. There are two basic features of the Anand’s model: firstly it does not require the definition of an explicit yield condition and no loading/unloading criteria. Secondly, a single scalar, *s*, is used as an internal variable to represent the isotropic resistance to plastic flow. When steady-state plastic flow occurs, the stress reaches the saturation value. For viscoplastic deformation behaviour, this steady-state plastic flow happens when the plastic flow has become fully developed and its rate equals the applied strain rate at the given temperature and strain rate. The Anand’s model is broken down into a flow equation, and three evolution equations:

The flow equation is given by:

$$\dot{\varepsilon}_p = \dot{\varepsilon} = A\left[\sinh\left(\frac{\xi\sigma}{s}\right)\right]^{1/m}\exp\left(\frac{-Q}{RT}\right) \tag{6-14}$$

The evolution equations are given by:

$$\dot{s} = \left\{h_0\left(\left|1-\frac{s}{s^*}\right|\right)^a \cdot \operatorname{sign}\left(1-\frac{s}{s^*}\right)\right\}\dot{\varepsilon}_p \quad a>1 \tag{6-15}$$

*where*

$$s^* = \hat{s}\left[\frac{\dot{\varepsilon}_p}{A}\exp\left(\frac{Q}{RT}\right)\right]^n$$

For isothermal and constant strain rate test, s* is always greater than s. Therefore, the term $\mathrm{sign}\left(1-\frac{s}{s^*}\right)$ is always positive. In order to define the model, the nine parameters (Table 6-1) need to be obtained from experimental data.

**Table 6-1 Parameter identification of the Anand's creep model**

| Parameter | SAC305 | Definition |
|---|---|---|
| $s_0$(MPa) | 1 | Initial value of deformation resistance |
| $Q/R$(K) | 2 | Activation energy/Universal gas constant |
| $A$(1/Sec) | 3 | Pre-exponential factor |
| $\xi$ | 4 | Stress multiplier |
| $m$ | 5 | Strain rate sensitivity of stress |
| $h_0$(MPa) | 6 | Hardening constant |
| $\hat{s}$(MPa) | 7 | Coefficient for deformation resistance saturation value |
| $n$ | 8 | Strain rate sensitivity of saturation value |
| $a$ | 9 | Strain rate sensitivity of hardening |

Use can be made of the saturation stress measured in experiments. The relationship between the saturation stress and model parameters can be obtained as follows:

$$\sigma^* = \frac{s^*}{\xi}\sinh^{-1}\left[\left(\frac{\dot{\varepsilon}_p}{A}\exp\left(\frac{Q}{RT}\right)\right)^m\right] \tag{6-16}$$

$$\sigma^* = cs^* = \frac{\hat{s}}{\xi}\left(\frac{\dot{\varepsilon}_p}{A}\exp\left(\frac{Q}{RT}\right)\right)^n \sinh^{-1}\left[\left(\frac{\dot{\varepsilon}_p}{A}\exp\left(\frac{Q}{RT}\right)\right)^m\right] \tag{6-17}$$

$$\sigma = c\cdot s;\ c<1$$

where c is a material parameter and is defined as

$$c = \frac{1}{\xi}\sinh^{-1}\left\{\left[\frac{\dot{\varepsilon}_p}{A}\exp\left(\frac{Q}{RT}\right)^m\right]\right\}$$

$$\dot{\varepsilon}_p = \dot{\varepsilon} = A\left[\sinh\left(\frac{\xi\sigma^*}{s^*}\right)\right]^{1/m}\exp\left(\frac{-Q}{RT}\right) \tag{6-18}$$

where $\dot{\varepsilon}$ is the applied strain rate in constant strain rate test.

Therefore from

$$\dot{\sigma} = c\dot{s} = ch_0\left(1-\frac{s}{s^*}\right)^a \dot{\varepsilon}_p \tag{6-19}$$

Integrating

$$d\sigma = ch_0\left(1-\frac{s}{s^*}\right)^a d\varepsilon_p$$

$$d\sigma = ch_0\left(1-\frac{\sigma}{\sigma^*}\right)^a d\varepsilon_p$$

$$d\sigma = ch_0\left(\frac{\sigma^*-\sigma}{\sigma^*}\right)^a d\varepsilon_p$$

$$\int_{\sigma_0}^{\sigma}\left(\frac{\sigma^*-\sigma}{\sigma^*}\right)^{-a} d\sigma = \int_0^{\varepsilon_p} ch_0 d\varepsilon_p$$

$$\left[\frac{1}{1-a}\left(\frac{\sigma^*-\sigma}{\sigma^*}\right)^{-a+1}\left(-\sigma^*\right)\right]_{\sigma_0}^{\sigma} = ch_0\left[\varepsilon_p\right]_0^{\varepsilon_p}$$

$$-\frac{\left(\sigma^*\right)^a}{1-a}\left[\left(\sigma^*-\sigma\right)^{1-a}-\left(\sigma^*-\sigma_0\right)^{1-a}\right] = ch_0\varepsilon_p \tag{6-20}$$

Rearranging and replacing $\sigma_0 = cs_0$

$$\sigma = \sigma^* - \left[\left(\sigma^*-cs_0\right)^{1-a} + \left(a-1\right)\left(\sigma^*\right)^{-a} ch_0\varepsilon_p\right]^{\frac{1}{1-a}} \tag{6-21}$$

The relationship between stress (σ) and the deformation resistance variable (s) is:

$$\sigma = cs$$

$$c = \frac{1}{\xi}\sinh^{-1}\left\{\left[\frac{\dot{\varepsilon}_p}{A}\exp\left(\frac{Q}{RT}\right)^m\right]\right\} \tag{6-22}$$

## 6.6 Parameter Estimation Methods

Various methods have been used by researchers to solve parameter estimation problems. Least-square, Levenberg-Marquardt algorithm, Conjugate gradient are examples of them. In these techniques, the inverse problems are formulated into parameter identification problems in which a set of parameters corresponding to the characteristics of the structure and material properties can be found by minimizing the error function. In this work a simple least squares method is adopted to determine the objective function whilst the parameters of the Anand's creep model are obtained by minimising the error between the experimental results and FEA simulations using genetic algorithm and conjugate gradient method.

In a test using cyclic loading profile, experimental data may be recorded over many cycles but in nearly all of the references [171-173], only a portion of this time series of experimental data curve are used in the parameter estimation process and this therefore assumes that the material behaviour during loading and unloading are the same. Numerous simulations performed so far by this author have demonstrated that this is not exactly the case. Even though a set of material data could match the experimental data during the loading stage, it does not necessarily imply that it would be the optimum dataset for the unloading stage as well. Since the purpose of this work is to obtain the data model that can produce damage indicators (such as a plastic work per load cycle) that match those found in experiments, experimental data from a whole load cycle need to be used in the inverse analysis process.

## 6.7 Traditional Parameter Estimation Method for Viscoplastic Model

Highlighted below is the conventional procedure that has been used by a number of researchers [174, 175, 176] to determine the material parameters of the Anand's model for solder alloys. The values of the nine parameters listed in Table 6-1 for solder alloys are determined by the following procedure:

a) Determination of the saturation stresses $\sigma^*$ under strain rates $\dot{\varepsilon}$ and temperatures $T$ from steady-state creep relation.
b) Nonlinear fitting of $Q/R$, $A$, $\hat{s}/\xi$, $m$ and $n$ in Equation(6-17)

c) Determination of $\hat{s}$ and ξ. The parameter ξ was selected such that the constant $c$ in Equation(6-15) is less than unity, and $\hat{S}$ was then determined from the combined term $\hat{s}$ /ξ.

d) Estimate the values of $a$, $h_o$ and $S_o$

In step d) the fitting procedure examines the influence of plastic strain hardening. From evolution equations and the relationship between the stress and deformation resistance is given by:

$$\frac{d\sigma}{d\dot{\varepsilon}_p} = ch_0\left(1-\frac{\sigma}{\sigma^*}\right)^a \qquad \textbf{(6-23)}$$

From Equation(6-15)

$$\dot{s} = \left\{h_0\left(\left|1-\frac{s}{s^*}\right|\right)^a \cdot \mathrm{s}i\,\mathrm{gn}\left(1-\frac{s}{s^*}\right)\right\}\dot{\varepsilon}_p \qquad \textbf{(6-24)}$$

$$\sigma = cs$$

An alternative approach is to integrate the above equation to obtain:

$$\sigma = \sigma^* - \left\{\left(\sigma^* - cs_0\right)^{(1-a)} + (a-1)ch_0\left(\sigma^*\right)^{-a}\varepsilon_p\right\}^{1/(1-a)} \qquad \textbf{(6-25)}$$

The material parameters $a$, $h_o$ , and $s$ were fitted from the σ~ε curves (especially the transient state) with various temperatures and strain rates. In the fitting, the saturation stresses given in step (a) were also used.

To determine the parameters of the Anand's model, a large body of experimental work are needed at different strain rates, temperature and loading profiles. Usually the constants in the flow function were obtained from the saturation creep stress, and then other evolution parameters will be fitted in the other steps. The response of the solder joint is then plotted on a stress-strain curve. To determine the parameters of the creep model used, the stress strain curve has to be segmented to determine the elastic and inelastic properties of the solder joint using the flow function. This segmentation is problematic in itself as the point of segmentation is dependent on the experience and skill of the researcher. These multi-step methods require the manual partition of the deformation curve into elastic part, evaluating part and saturated part. This partition may introduce errors, especially at low temperature and high strain rate where the specimen will not reach saturation stress before failure. There is also an added difficulty with the above method in that the experiments are very sensitive and any spurious dataset will affect the entire analysis. Due to the need for a large experimental dataset there is a high probability that some of the experimental data may be inconsistent. It is generally very difficult to identify spurious data. The large scatter in material properties of lead-free solder is testament to this inherent difficulty in the method.

## 6.8 Inverse Analysis Methodology

The objective of the inverse analysis in this work is to determine the Anand’s model material parameters that minimises the difference between Finite Element simulation and experimental results for a predefined test. In performing the material parameters estimation as demonstrated by Husain et al [124] a large body of experimental work is needed. This as explained in section 6.7 is partly responsible for the large variation in material dataset as reported in the literature. To address this need for a large experimental dataset, we are proposing determination of the material parameters by using limited experimental data and performing optimisation so that the best modelling prediction accuracy for a particular quantity can be achieved with a limited amount of data.

In this work, some of the creep law parameters are assumed to be unknown and the aim of the FE is to predict these parameters and therefore it is an inverse FE analysis. Since the form of the creep law is known, this inverse analysis is a "parameter estimation"' problem rather than a "function estimation" problem for which functions with unknown form need to be found. Generally, most inverse analysis methods will eventually become a parameter and/or function optimisation problem. The widely used method of fitting a strain rate equation based on the minimum strain-rate measurement can be regarded as an inverse analysis but FE is not used in that case. The inverse methodology is discussed below and summarized in figure 6-8.

At the start of the procedure a set parameters for a material that represents closely the material in the experiment are selected from available literature. These parameters span the design space in the optimization problem in the inverse analysis. The boundaries of the design space are defined by choosing suitable upper and lower limits for the parameters.

The deviation between computed observables and experimental ones is expressed by the mean square value (Equation 6-26):

$$\psi = \sum_{i=1}^{np} \left( F_{FE}(d_i) - F_{\exp}(d_i) \right)^2 / np \qquad \textbf{(6-26)}$$

where $F_{FE}$ and $F_{\exp}$ are the computed and simulated force respectively. This “error function” is the objective function that needs to be optimized in the inverse FEA analysis.

The inverse FEA procedure in the present work comprises the following steps:

- Obtain experimental load–displacement curves
- Smooth the experimental data and obtaining approximate formula to represent the data
- Identify the strain rate model parameters that have strongest impact on the FE simulation results, and using these parameters as variables that need to be estimated
- Use design of experiment (DOE) method to generate “designs” in the design space spanned by the selected Anand’s parameters
- Run FE analysis using the strain rate model with parameters that are defined in the DOE analysis for each “design”, and obtain load-displacement curves for all the “designs”.
- The values of the objective function $\psi$ are calculated for each design.
- Second order polynomial of the design variables is fitted to the $\psi$ values to obtain an approximate equation of the objective function $\psi$ in the design space.
- Use optimisation methods to determine the optimum model parameters that minimize $\psi$.

- Run finite element simulation using the optimum parameters and compare FE results with experimental results.

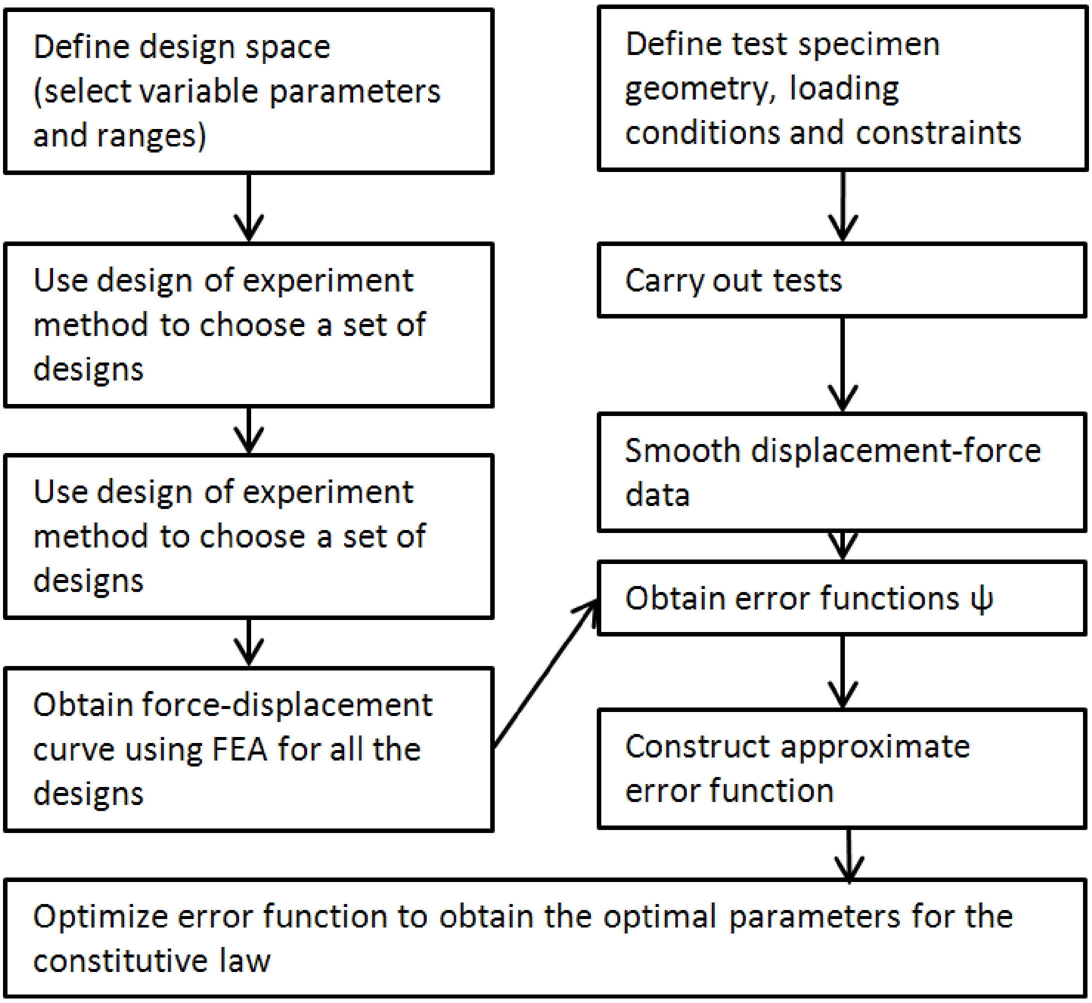

**Figure 6-8 Methodology for improving the constitutive law**

## 6.9 Results

The results presented below are for the use of two visco-plastic/creep strain rate models to simulate the results from cyclic isothermal experiments on SAC solder joints.

### 6.9.1 The Garofalo’s strain rate model

The Garofalo’s strain rate equation is given in Equation 4-19. This equation represents the secondary creep strain rate as a function of stress and temperature.

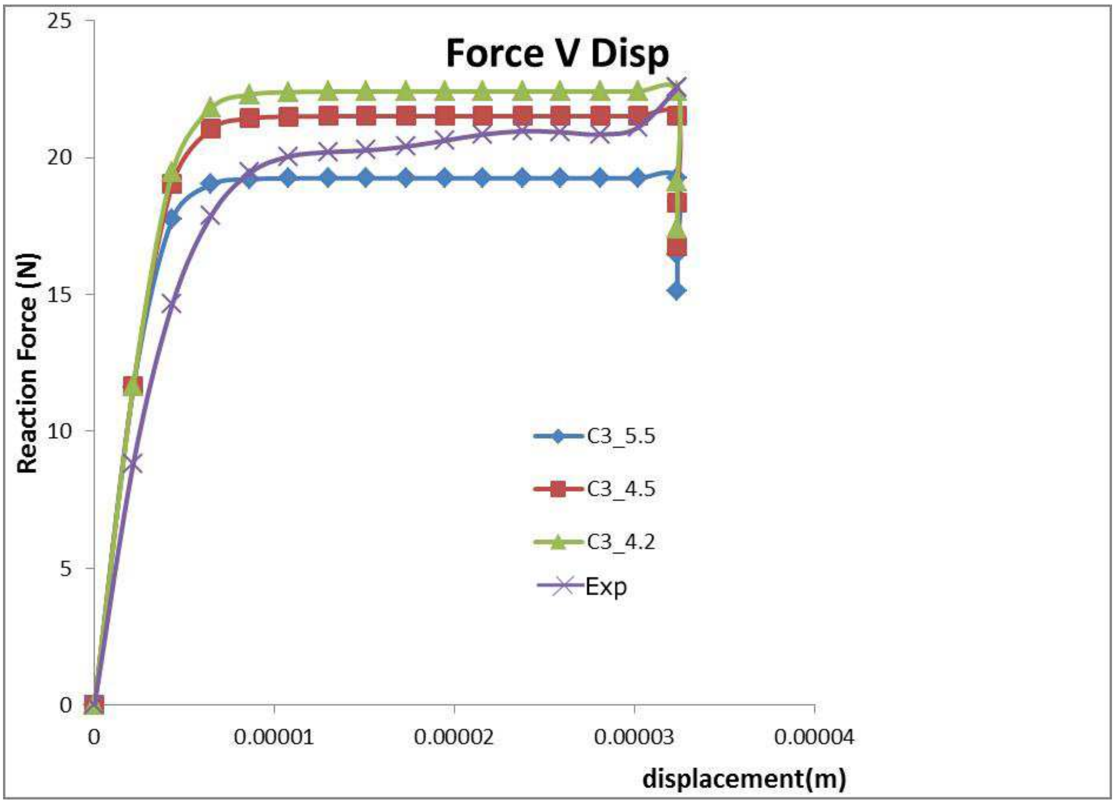

**Figure 6-9 Comparison of force-displacement curve for different values of parameter C3**

The Garofalo model has no hardening (strain or time) component nor is the formulation time dependent. As shown in figure 6-9 however, the experimental data indicate that hardening is an important phenomenon in solder and any model that omits it could not provide a good fit between experiment and FEA simulation results. Because of this the modelled material behaves almost with pure plasticity with the tangential (or plastic) modulus of zero in the plastic region. This obviously does not correspond with the experimental data and there is therefore a need for a more representative model that will take into account the drawbacks from the Garofalo's equation.

### 6.9.2 Inverse modelling results using Anand's model

Before the inverse analysis was carried out, the effects of all the material properties on the predicted Force vs displacement curves were investigated. For example in figure 6.10, results for three Young's modulus values are compared and the predicted curves are not sensitive to the changes of E.

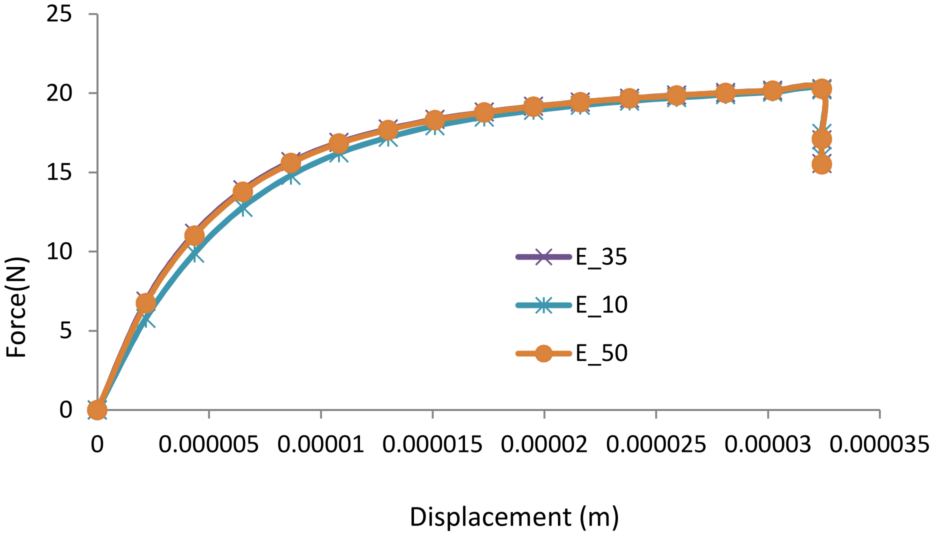

**Figure 6-10 Effect of changing the Young's Modulus E. E_35, E_10and E_50 are for E=35, 10 and 50 GPa respectively.**

Of all the parameters in the Anand's model, some have stronger impact on the error function $\psi$ than others. In this work, the parameters that have been chosen as design parameters are *m* and $\xi$. The designs that have been obtained using DoE method (composite with D-optimal) and the error function values for these designs are listed in Table 6-2. In the DOE analysis, the 9 design points were selected using the Composite and D-optimal methods [177].

**Table 6-2 parameter optimisation and error**

| m | ξ | ψ |
|---|---|---|
| 0.05 | 1 | 125.3 |
| 0.05 | 1.5 | 875.3 |
| 0.05 | 2 | 1602 |
| 0.275 | 1 | 2706.7 |
| 0.275 | 1.5 | 213.5 |
| 0.275 | 2 | 77.4 |
| 0.5 | 1 | 11586.6 |
| 0.5 | 1.5 | 3129 |
| 0.5 | 2 | 740.3 |
| 0.331 | 1.9 | 60.3 |
| 0.33 | 2 | 34.2 |

Based on the results in the Table 6-2, a second order polynomial error function can be obtained using the least square method:

$$\psi = 572.55 + 1381.7m - 1239.4\xi - 1940m\xi + 1250.1m^2 + 639.98\,\xi^2$$

The method 1 optimisation is based on gradient based methods, the options for the constrained method is the modified method of feasible direction whilst the unconstrained method is based on the Broydon-Fletcher-Goldfarb-Shanno method. The gradient calculation is based on the forward difference. Method 2 is based on the genetic algorithm method using the default parameters set in the software [178]. The results indicated a slight variation of the results obtained for the two parameters chosen. Table 6-3 shows the optimized parameters and figure 6-12 compares the test results with the simulation results. In the figure 6-11, Anand's_optimise and Anand's_optim2 are based on the optimised Anand's parameters shown in Table 6-3 and Garafalo is based on the Garafalo strain rate model described earlier.

**Table 6-3 Optimised parameters**

| | Method 1 | Method 2 |
|---|---|---|
| $\xi$ | .331 | .3306 |
| m | 1.9 | 2 |
| $\psi$ | 34.2 | 60.3 |

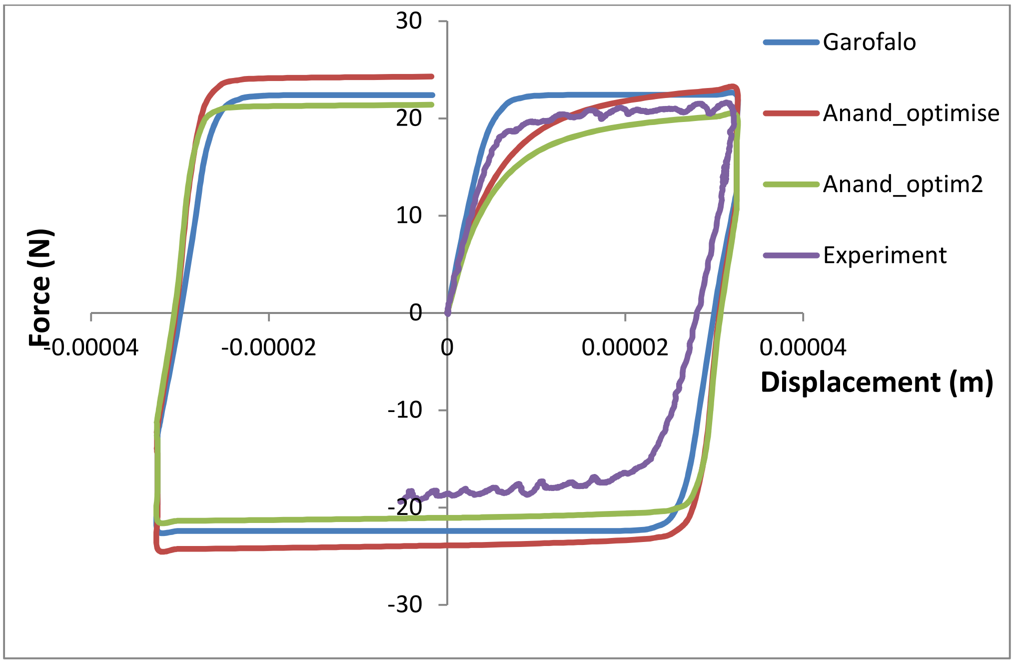

**Figure 6-11 Comparison of experiment and simulation results.**

The optimised Anand's model has also been used to model a sample with 4 solder joints and the results are compared with experiments in figure 6-12. It shows that much greater discrepancy exists between the results compared to the single joint results. This is expected and shows how constitutive models are dependent on sample geometry and loading conditions. If the Anand's model has to be used for samples with any number of solder joints then the inverse analysis has to make use of the experimental data from all the samples. However, that would increase the accuracy of the simulation for a single joint.

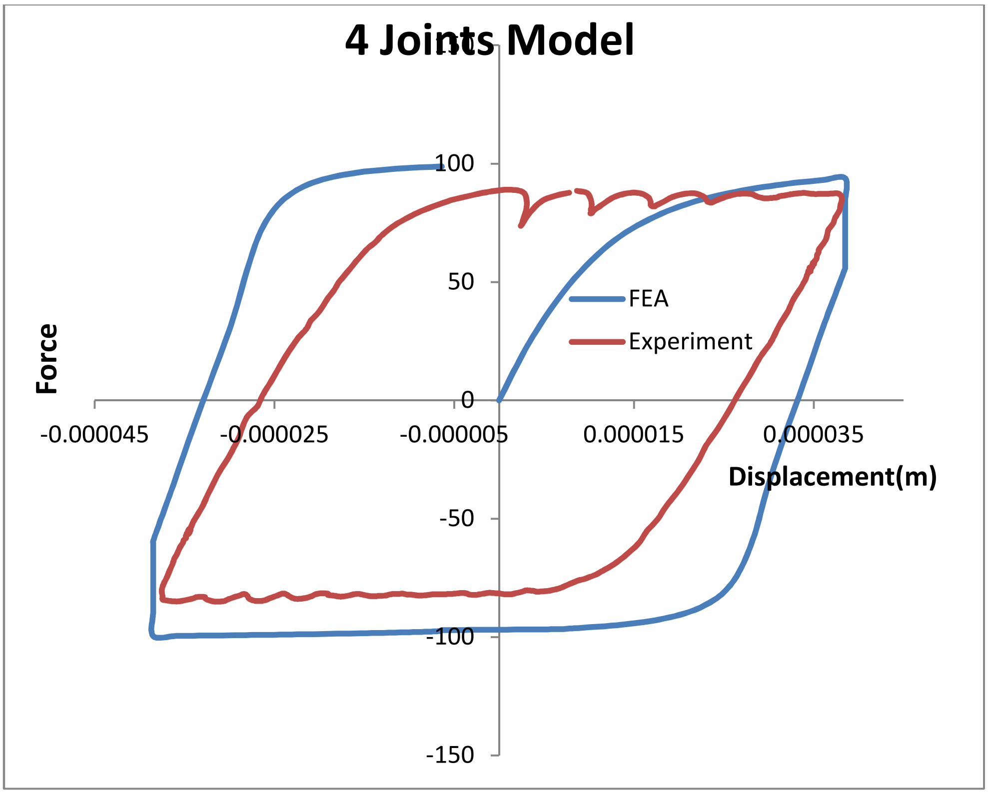

**Figure 6-12 Comparison of four joint results.**

The force-time plots of the experimental and simulation results are shown in figure 6-13. Two samples were used and the results demonstrate that the behaviour of the solder joints under cyclic loading varied markedly from one sample to the other. Furthermore, the experimental results still have some marked difference from the simulation results. Instead of the gradual decrease in force during the dwell, the results from experiments indicated that the force drops rapidly and then plateaus a few minutes into the dwell and remains at that level until the loading /unloading phase resumes. The solder therefore is at a higher stress after the dwell in the experiments as compared to that of the simulations. The relaxation time of the solder joint is therefore quite short when compared to the simulation result. This observation has highlighted a limitation of the Anand's model and need further investigation in the future.

Figure 6-13 also demonstrates clearly why as stated in section 6.5 fitting a segment of the hysteresis loop results in parameters that are not fully representative of the complete cycle.

Comparing the loading section of the experiments and simulation, one notice that sample two matches the simulation better but in the remainder of the loop sample 1 match the simulation better. Therefore, matching a segment of the hysteresis will inevitably introduce errors into the analysis and hence different material parameters in Anand's model.

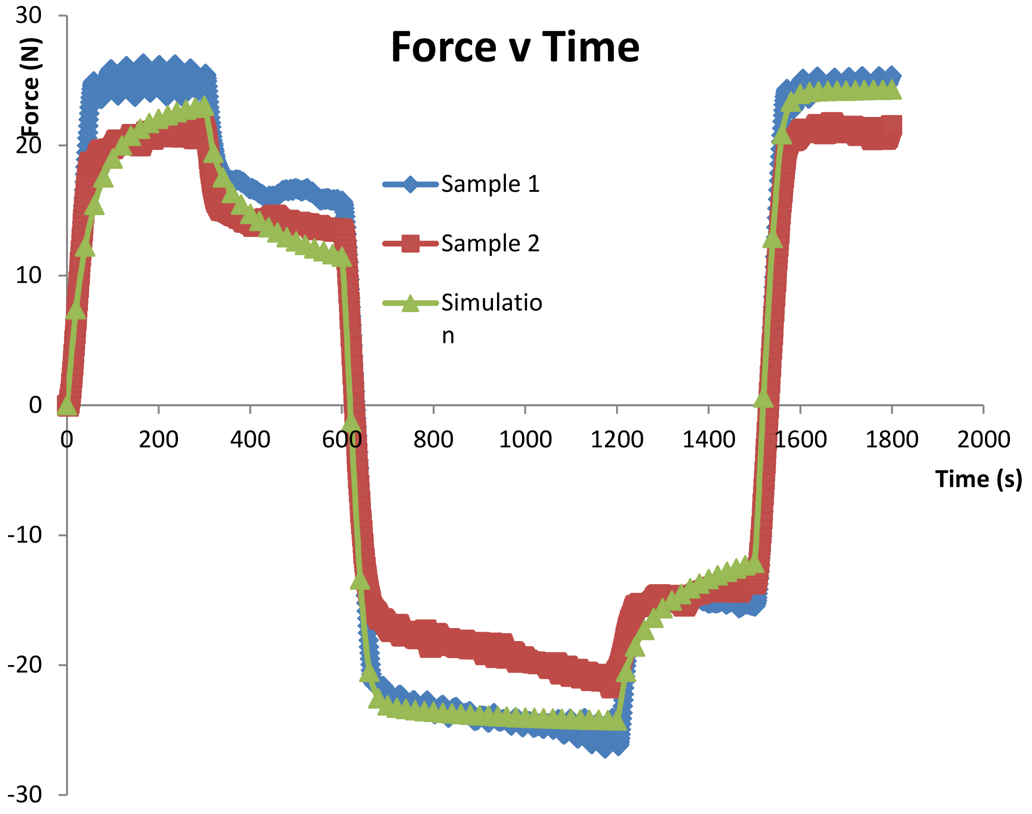

**Figure 6-13 Comparison of force v time plot for the two samples and the simulation result**

There is a large variation in the quality of solder joints produced because of the limitations of the manufacturing techniques used. The incidence of voids in the solder is a major reason for the variations in the results seen for the solder specimens. In the inverse method as described in this work, voids are explicitly taken into account but the model parameters are implicitly assumed to be applicable only for the solder samples that have the same voids distribution and density as that in the experiments from which the parameters are obtained.

## 6.10 Conclusions

The unified Anand’s creep model has been demonstrated to be better than the Garofalo’s model in predicting the inelastic behaviour of lead free solder in cyclic loading conditions. The determination of the parameters of Anand’s model without resorting to segmentation of the stress-strain curve is a major improvement in using different determination criteria to analyse the material properties of lead-free solder.

The inverse procedure described above provides a major improvement to the general methods of parameter determination for lead free solder. Determining the parameters without resorting to segmentation of the stress-strain curve reduces a major source of error and hence the wide scatter in published material properties data. This method also reduces the need for a very large body of experimental work to determine strain rate model parameters.

The strength of the proposed method is that constitutive strain rate equations can be optimised for a test. The strain rate equation is, however, not expected to be accurate for other tests where sample geometry or other conditions are different.

# Chapter 7 Conclusions

Although solder joints material properties and performance under tests and application conditions have been studied for many years, and many types of general test equipment are available for carrying out experiments on solder specimens, some major challenges are still facing engineers and academia. One major issue that has been dealt with in this thesis is the development of a dedicated compact vibration test machine driven by piezoelectric cells. By using 3D CAD software and Finite Element analysis, the design and its several variations have been characterised and the equipment was shown to meet the requirements. The equipment is capable of testing specimens of realistic sizes of solder joint in microelectronics applications. The equipment was made and validations test were performed to determine the equipment parameters. The design of the solder specimen was also analysed in order to determine the optimum shape, and the deformation of the sample was obtained to help interpretation of test results and failure mode. The developed equipment can be used by manufacturers to carry out rapid assessment of solder sample performance under vibration conditions and for research and development engineers and scientists to gather material properties data.

BGA is a widely used interconnect technology in the microelectronics manufacturing industry. The behaviour of BGA sized lead-free solder specimen under isothermal test conditions using the NPL IPTM (Interconnect Properties Test Machine) has been analysed. In the industry, solder joints are often tested under cyclic thermal-mechanical conditions but using isothermal testing does have convincing advantages as discussed in Chapter 5. A multi-joint specimen has been used in this work. It has been modelled and the response of the solder joints are analysed to determine the regions of failure and determine whether they match those from experiment. These models allowed the modelling of various number of solder joint specimen in the sample and the differences in response to static and transient loading conditions. Despite the loading of the samples being in shear, the response of the specimen includes bending as well. The bending stress varies depending on whether the specimen is undergoing tensile or compressive loading conditions. The regions of maximum stress concentrations are therefore at the corners of the solder joints and these are the region of likely failure of the package. This matches quite well with experiment but the failure does not always start in this region because the uniformity of the solder is hard to achieve.

The design of the test specimens led to the results that the stress state resembles that in BGA solder joint under thermal-mechanical test conditions where thermal expansion mismatch causes mixed shear and tensile stresses. This further justifies the use of the isothermal test as a tool for the evaluation of BGA solder joint performance.

One of the major problem in obtaining solder property data for computer aided engineering is the wide scatter in the parameters of constitutive models such as Anand’s combined plastic, and viscoplastic strain rate model. In the study of solder joint using Finite Element analysis, Garofalo’s creep strain rate model is often used. With only a few parameters, it is simple to use but it does not capture the true behaviour of the solder undergoing creep deformation as it doesn’t account for any hardening that the solder could be experiencing. This limitation of the Garofalo’s model is addressed to some extent by the Anand’s model with its nine parameters and among them is a hardening parameter that evolves with time.

In order to perform solder joint analysis using the Anand’s model, a large test dataset are needed to determine the material parameters. This is a time consuming process with many challenges and the resulting model does not suit all solder joint modelling because it is difficult to separate the effects of geometry, microstructure, and variations in alloy composition. It is inevitable that different experiments result in significantly different results. The method that has been proposed in this work uses a limited experimental dataset and uses inverse FEA modelling techniques to improve Anand’s model for a particular test specimen under a set of test conditions so that the model is optimised for the prediction of the test results. The model is best used for solder joints that are similar to the ones used in the experiment in all aspects. This method is relatively quick and should be useful in many applications. There is a non-linear relationship between the model parameters in the Anand’s model and care must be taken in choosing the parameters that will not negate the expected response. Although all the parameters in the constitutive strain rate model can be treated as variables in the inverse analysis, two material parameters were chosen for simplicity. After minimising the error function, the new FEA results matched closely with the experiment results. BGA type solder joints under isothermal cyclic test conditions and Anand’s or Garofalo’s strain rate models are used as the specimens and the constitutive models in this work but the methodology is general. It is even possible to use function rather than parameter estimation in the inverse FEA analysis to find the constitutive strain rate model.

This is a list of suggestions for projects that could follow on from the work presented in this thesis:

- Use geometric optimization for specimen design to make the stress and strain more homogeneous in vibration test.
- Perform further work on the overall effect of piezoelectric transducers to determine the consistency of the generated loading profile on the solder specimen.
- Investigate the discrepancies in the hysteresis loops from experiments and simulations.
- Perform lifetime calculation for the multi-joint models and validate them.
- Use all parameters of the Anand’s model in the inverse analysis and include the effect of temperature.
- Use inverse analysis method to determine the function of solder viscoplastic constitutive law

# References

1. Directive 2002/95/EC of the European Parliament and of the Council of January 2003 on the restriction of the use of certain hazardous substances in electrical and electronic equipment. 2003. p. 19-23.

2. Directive 2002/96/EC of the European Parliament and of the Council of 27 January 2003 on waste electrical and electronic equipment (WEEE). 2003. p. 24-28.

3. http://www.astm.org/Standards/B32.htm

4. Harper, C.A., “Electronic Packaging and Interconnection Handbook”, McGraw Hill, New York, 2nd edition, 1997

5. Bazu, M. and Bajenescu, T., "Failure Analysis. A Practical Guide for Manufacturers of Electronic Components and Systems", J. Wiley & Sons, ISBN-10: 0-470-74824-9, 2011.

6. Kong, R., Tulkoff, C. and Hillman, C., "The Reliability Challenges of QFN Packages", SMTA Symposium, Shanghai, China, Aug. 2010, pp. 217-219.

7. Tummala, R. R., *Fundamentals of Microsystems Packaging*, McGraw-Hill, 2001

8. Yu, H. and Shangguan, D., "Solidification and reliability of lead-free solder interconnection", Soldering & Surface Mount Technology, Vol. 25 Iss: 1, pp.31 – 38, 2013

9. Amalu, E.H. and Ekere N.N., Damage of lead-free solder joints in flip chip assemblies Subjected to high- temperature thermal cycling. Computational Materials Science, vol. 65. pp. 470-484. ISSN 0927-0256, 2012.

10. Tummala, R. R., “Packaging: Past, Present and Future,” Proc. of the IEEE 6th International Conference on Electronic Packaging Technology, 2005

11. Cirimele R., “BGA Reballing Reliability: A Study of Multiple Reball Processes Looks at Copper Dissolution and Functionality, Circuits Assembly”, June 2009, pp.27-29.

12. Dauksher W., Lau J., “A finite-element-based solder-joint fatigue-life prediction methodology for Sn-Ag-Cu ball-grid-array packages”, IEEE Trans. Device Mater. Reliab. 9(2), 231–235 (2009)

13. Lau J.H. and Pau Y.H, “Solder joint reliability of BGA, CSP, Flip Chip and Fine Pitch SMT assemblies”, Mcgraw Hill, New York, 1997, pp. 4.

14. Kamara, E., Lu, H., Bailey, C., Hunt, C., Di Maio, D. and Thomas, O., “Computer simulation and design of a solder joint vibration test machine”, 11th International Conference on Thermal, Mechanical and Multi-Physics Simulation, and Experiments in Microelectronics and Microsystems, EuroSimE 2010.

15. Ridout, S., Modelling and experiments on an isothermal fatigue test for solder joints. Eurosime pages 478-482, IEEE 2005

16. Kamara, E., Lu. H, Thomas. O, Di Maio, D., Hunt, C., Fulton, I., “Modelling and Experimental Measurement of Multiple Joint Lead Free Solder Interconnects Subjected to Low Cycle Mechanical Fatigue”, Proceeding of the 18th 2011 European Microelectronics Packaging Conference (IMAPS EMPC 2011), Brighton, UK 12-25 September 2011, pp.214-220

17. Bai, N., Chen, X., Gao, H., “Simulation of uniaxial tensile properties for lead-free solder with modified Anand model”, Materials and Design 30 (2009) 122-128.

18. Wang, Q., Zhang,Y., Liang, L., Liu, Y., Irving, S., “Anand Parameter Test for Pb-Free Material SnAgCu and Life Prediction for a CSP”, Electronic Packaging Technology, 2007. ICEPT 2007. 8th International Conference.

19. Mysore, K., Subbarayan, G., Gupta, V., Zhang, R., “Constitutive and Aging Behavior of Sn3.0Ag0.5Cu Solder Alloy”, IEEE Transactions on Electronics Packaging Manufacturing, v32, n4, p221-232, Oct.2009.

20. Bhate, D., Chan, D., Subbarayan, G., Chiu, T.C., Gupta, V., Edwards, D., “Constitutive behavior of Sn3.8Ag0.7Cu and Sn1.0Ag0.5Cu alloys at creep and low strain rate regimes”, IEEE Transactions on Components and Packaging Technologies, v31 ,n3, p622-633, 2008.

21. Kamara, E., Lu. H, Thomas. O, Di Maio, D., Hunt, C., Fulton, I., “Inverse Analysis of Solder Joint Creep Properties”, Proceeding of the 13th International Conference on Electronic Packaging Technology & High Density Packaging (ICEPT-HDP 2012) pp275-279

22. Kariya, Y., Gagg, C., Plumbridge, W.J., "Tin pest in lead-free solders", Soldering & Surface Mount Technology, Vol. 13 Iss: 1, pp.39 – 40, 2001

23. Sinnadurai F.N., “Handbook of Microelectronics Packaging & Interconnection Handbook”, Mcgraw Hill, Electrochemical Publications, Scotland, 1985, pp. 1-3

24. Soldertec, European Lead-free Roadmap, Ver.1, pp. 1-26, 2002.

25. Kariya, Y. and M. Otsuka, “Effect of Bismuth on the Isothermal Fatigue Properties of Sn-3.5Ag Solder Alloy”, Journal of Electronic Materials, 1998. 27(7): p. 866-870

26. Kanchanomai, C., Miyashita, Y., Mutoh, Y., “Low Cycle Fatigue Behavior of Sn-Ag Sn-Ag-Cu and Sn-Ag-Cu-Bi Lead-free Solders,” Journal of Electronic Materials, Vol. 31, pp. 456-465, 2002.

27. McCormack, M., Chen, H. S., Jin, S., “New Lead-Free Sn-Ag-Zn-Cu Solder Alloys with Improved Mechanical Properties,” Applied Physics Letters, Vol. 65 (10) pp. 1233-1235, 1994.

28. Fields, R. J., Low, S. R., “Physical and Mechanical Properties of Intermetallic Compounds Commonly Found in Solder Joints,” available online at: http://www.metallurgy.nist.gov/mechanical_properties/solder_paper.html.

29. Zhao, J., Y. Miyashita, and Y. Mutoh, “Fatigue crack growth behavior of 96.5Sn-3.5Ag lead-free solder”, International Journal of Fatigue, 2001. 23: p. 723-731.

30. Ganesan, S., Pecht, M., Lead-free Electronics, Wiley-Interscience Publication, pp. 51-52, 2006.

31. Vandevelde, B., Christiaens F., Beyne, E., Roggen, J., Peeters J., Allaert, K., Vandepitte, D., and Bergmans J., “Thermomechanical Models for Leadless Solder Interconnections in Flip-chip Assemblies”, IEEE Transactions on Componnents, Packaging, and Manufacturing Technology -A, Vol. 21, No. 1, pp. 177–185, Mar. 1998.

32. Pitarresi, J. M., Sethuraman, S., Nandagopal, B., and Primavera, A., "Reliability Modeling of Chip Scale Packages," Proceedings of the 26th International Electronics Manufacturing Technology Symposium, pp. 60-69, 2000.

33. Ng, H. S., Tee, T. Y., Goh, K. Y., Luan, J. E., Reinikainen, T., Hussa, E., and Kujala, A., "Absolute and Relative Fatigue Life Prediction Methodology for Virtual Qualification and Design Enhancement of Lead-Free BGA," Proceedings of the 55th Electronic Components and Technology Conference, pp. 1282-1291, 2005.

34. Chen, X., Lin, Y., Liu, X., and Lu, G. Q., "FEM Analysis with Cyclic Visco-Plasticity for Solder Bumped Flip-Chip Packaging," Proceedings of the Fifth International Conference on Electronic Packaging Technology, ICEPT, pp. 282-287, 2003.

35. Classe, F. C., and Sitaraman, S. K., "Asymmetric Accelerated Thermal Cycles: An Alternative Approach to Accelerated Reliability Assessment of Microelectronic Packages," Proceedings of the Fifth Conference on Electronics Packaging Technology, pp. 81-89, 2003.

36. Pang, J. H. L., and Low, T. H., "Modeling Thermal Cycling and Thermal Shock Tests for FCOB," Proceedings of the Eighth Intersociety Conference on Thermal and Thermomechanical Phenomena in Electronic Systems, pp. 987-992, 2002.

37. Rodgers, B., Punch, J., Jarvis, J., “Finite Element Modelling of a BGA Package subjected to Thermal And Power Cycling”, Proceedings of the ITherm

Conference on Thermal, Mechanics and Thermomechanical Phenomena in Electronic Systems, 2002

38. Schubert, A., Dudek, R., Auerswald, E., Gollhardt, A., Michel, B. and Reicbl. H., “Fatigue Life Models for SnAgCu and SnPb Solder Joints Evaluated by Experiments and Simulation”, Electronic Components and Technology Conference. IEEE, 2003.

39. Wang, G. Z., Cheng, Z. N., Becker, K. and Wilde, J., “Applying Anand Model to Represent the Viscoplastic Deformation Behavior of Solder Alloys”, Journal of Electronic Packaging September 2001, Vol. 123

40. Wei, Y., Chow, C. L., Vianco, P. and Fang E., “Isothermal Fatigue Damage Model for Lead-free Solder”, International Journal of Damage Mechanics 2006 15: 109

41. Zhang Q.K., Zhu Q.S., Zou H.F., Zhang Z.F., “Fatigue fracture mechanisms of Cu/lead-free solders interfaces Materials Science and Engineering” JOM 527 (2010) 1367–1376

42. Siviour, C. R., Walley, S. M., Proud, W. G. and Field J. E., “Mechanical properties of SnPb and lead-free solders at high rates of strain”, J. Phys. D: Appl. Phys. 38 (2005) 4131–4139.

43. Fei, Q., Tong, A., Na, C., “Dynamic Behavior Tests of Lead-free Solders at High Strain Rates by the SHPB Technique”, 2008 International Conference on Electronic Packaging Technology & High Density Packaging (ICEPT-HDP 2008).

44. Zamiri, A., Bieler, T.R. and Pourboghrat, F., “Anisotropic Crystal Plasticity Finite Element Modeling of the Effect of Crystal Orientation and Solder Joint Geometry on Deformation after Temperature Change”, Journal of Electronic Materials, Vol. 38, No. 2, 2009.

45. Geng, P., “Dynamic Test and Modeling Methodology for BGA Solder Joint Shock Reliability Evaluation”, Proceedings of the 55th Electronic Components and Technology Conference, pp. 654-659, 2005.

46. Lim, M., Tee, T.Y., Ng, H.S., Deodato, C., Tiziani, R., Diot, J., Chiu, A., and Zhong, Z.W., “Design Analysis of Multi-chip QFN Solder Joint Reliability”, SEMICON Advanced Packaging Technology Symposium, Singapore, 2004, pp. 157-162.

47. Arra, M., Xie, D., and Shangguan, D., “Performance of lead-free solder joints under dynamic mechanical loading”, Proceedings of 52th Electronic Components & Technology Conference, San Diego, California, USA, May 2002, IEEE, (2002), pp. 1256 – 1262.

48. Lall, P., Shah, M., Drake, L., Moore, T., Suhling, J., “Thermo-mechanical reliability management models for area-array packages on cu-core and no-core assemblies”, SMTA Journal Volume 21 Issue 3, 2008.

49. Pitarresi, J., Geng, P., Beltman W., and Ling, Y., 2002,”Dynamic Modeling and Measurement of Personal Computer Motherboards,” 2002 IEEE Electronic Components and Technology Conference, pgs. 597-603

50. Wu, C.M.L. and Huang, M.L., “Creep Behavior of Eutectic Sn-Cu Lead-Free Solder Alloy”, Journal of Electronic Materials, 2002. 31(5): p. 442-448.

51. Wang, G. Z., Cheng, Z. N., Becker, K. and Wilde, J., “Applying Anand Model to Represent the Viscoplastic Deformation Behavior of Solder Alloys”, Journal of Electronic Packaging SEPTEMBER 2001, Vol. 123

52. Kim, I. and Lee, S., “Reliability and Failure Analysis of Lead-Free Solder Joints for PBGA Package Under a Cyclic Bending Load”, IEEE Transactions on Components and Packaging Technologies, vol. 31, no. 2, JUNE 2008

53. Tee, T.Y., Ng, H.S., Siegel, H., Bond, R., and Zhong, Z.W., “Design Analysis of Touch Chip for Enhanced Package and Board Level Reliability,” 6th EPTC Conference Proc., Singapore, 2004, pp. 743-747.

54. Bansal, A., Yoon, S., Mahadev, V., “Flexural Strength of BGA Solder Joints with ENIG Substrate Finish using 4-Point Bend Test”, Proceedings of the SMTA Pan Pacific Microelectronics Symposium, pp. 1-8, 2005.

55. IPC-9702 Monotonic bending characterisation of board-level interconnect , jun 2004. 2002

56. Chong, D., Ng, K., Tan, J., Low, P., Pang, J., Che, F., Xiong, B., and Xu, L., "Drop impact reliability testing for lead-free and leaded soldered IC packages", Proceedings of the 55th Electronic Components & Technology Conference, Lake Buena Vista, Florida, USA, June 2005, IEEE, (2005), pp. 622-629.

57. Lall, P., N. Islam, J. Suhling, and R. Darveaux, “Model for BGA and CSP Reliability in Automotive Underhood Applications”, Proceedings of the Electronic Components Technology Conference, New Orleans, LA, pp. 189–196, May 27–30, 2003.

58. Lall, P., Choudhary, P., Gupte, S., Suhling, J., “Health Monitoring for Damage Initiation & Progression during Mechanical Shock in Electronic Assemblies”, Proceedings of the 56th Electronic Components and Technology Conference, pp. 96-105, 2006.

59. Mishiro, K., Ishikawa, S., Abe, Mitsunori., Kumai, T., Higashiguchi, Y., Tsubone, K., “Effect of the drop impact on BGA/CSP package reliability”, Transactions on Microelectronics Reliability, Vol. 42, pp. 77-82, 2002.

60. Osterman, M. and A. Dasgupta, "Life expectancies of Pb-free SAC solder interconnects in electronic hardware", Journal of Materials Science: Materials in Electronics, 2007. 18: p. 229-236.

61. Di Maio, D. and Hunt, C., "High Frequency Vibration Tests of SnPb and LeadFree Solder Joints", NPL MAT 2, August 2007.

62. Stam, F. A., Davitt, E., "Effects of thermomechanical cycling on lead and lead-free (SnPb and SnAgCu) surface mount solder joints". Microelectronics Reliability, 2001. 41: p. 1815-1822.

63. Mattila, T.T., Marjamäki, P., and Kivilahti, J.K., “Reliability of CSP Interconnections Under Mechanical Shock Loading Conditions”, IEEE transactions on components and packaging technologies, vol. 29, no. 4, december 2006

64. Tsai, K.T., Liu, F-L,. Wong, E.H., Rajoo, R. (2006) "High strain rate testing of solder interconnections", Soldering & Surface Mount Technology, Vol. 18 Iss: 2, pp.12 - 17

65. Hin, T.Y., Behl, K.S., Seetharamu, K.N., “Development of a Dynamic Test Board for FCBGA Solder Joint Reliability Assessment in Shock & Vibration”, 2003 Electronics Packaging Technology Conference, 0-7803-8205-6.

66. Perkins, A. and Sitaraman, S.K. "Vibration-induced Solder Joint Failure of a Ceramic Column Grid Array (CCGA) package". in 54th Electronic Components and Technology Conference. 2004. Las Vegas, NV, USA: IEEE.

67. Mei-Ling Wu, “Vibration Failure Assessment Methodology for the Fatigue Life of Ball Grid Array BGA Solder Joints”, IEEE Microsystems, Packaging, Assembly & Circuits Technology 3rd International Conference, IMPACT 2008, pages 201-204.

68. Grieu, M., Massiot, G., Maire, O., Chaillot, A., Munier, C., Bienvenu, Y., Renard, J., “Durability Modelling of a BGA Component Under Random Vibration,” Proceedings of the EuroSimE, 2008

69. Selvakumar, A., Sakri, M.I., Abuthakeer, S., Mohanram P.V., “Experimental Analysis of Fundamental Frequencies for a PCB with Various Mounting Materials,” National Journal of Technology, 2011, Vol. 7, No.3, pp.127

70. Eckert, T., Müller. W.H., Nissen, N.F., Reichl, H., “Solder Joint Fatigue Life Model for Combined Vibration and Temperature Environments”, 2009 Electronic Components and Technology Conference

71. Tu, L., Chen, Y.C. and. Lai, J.K.L., “Effect of intermetallic compounds on vibration fatigue of μBGA solder joint,” IEEE Trans. Advanced Packaging., 24, pp. 197-205, 2001.

72. Lagattolla, W., “HALT/HASS - THE NEXT GENERATION OF ENVIRONMENTAL TESTING”, www.tracelabs.com, Trace Laboratories - Central in Palatine, IL

73. Vianco, P. T., Rejent, J.A., Kilgo, A.C., “Time-independent Mechanical and Physical Properties of the Ternary 95.5Sn-3.9Ag-0.6Cu Solder, Journal of Electronic Materials, Vol. 32 (3), pp. 142-151, 2003.

74. Xiao, Q., Bailey, H. J, Armstrong, W. D., “Aging Effects on Microstructure and Tensile Property of Sn3.9Ag0.6Cu Solder Alloy,” Journal of Electronic Packaging, Vol. 126 (2), pp. 208-212, 2004.

75. Pang, J. H. L., Low, T. H., Xiong, B. S., Xu, L., Neo, C. C., “Thermal Cycling Aging Effects on Sn–Ag–Cu solder Joint Microstructure, IMC and Strength,” Thin Solid Films, Vol. 462-463, pp. 370-375, 2004.

76. Hwang, J. S., Implementing Lead-free Electronics, McGraw-Hill, pp. 1-9, 2004.Bansal et al. [2005]

77. Fouassier, O., Heintz, J.-M., Chazelas, J., Geffroy, P.-M., Silvaina, J.-F., “Microstructural Evolution and Mechanical Properties of SnAgCu Alloys,” Journal of Applied Physics, Vol. 100, pp. 1-8, 2006.

78. Pang, J. H. L., Xiong, B. S., Neo, C. C., Zhang, X. R., and Low, T. H., "Bulk Solder and Solder Properties for Lead Free 95.5Sn-3.8Ag-0.7Cu Solder Alloy," Proceeding of the 53rd Electronic Components and Technology Conference, pp. 673-679, 2003.

79. Wiese, S., Schubert, A., Walter, H., Dudek, R., Feustel, F., Meusel, E., Michel, B., "Constitutive Behavior of Lead-free Solders vs. Lead-containing Solders - Experiments on Bulk Specimens and Flip-Chip Joints," Proceeding of the 51st Electronic Components and Technology Conference, pp. 890-902, 2001.

80. Li, D., Liu, C., Conway, P., "Micromechanical Characterization of Sn-Ag-Cu Solder FCOB Interconnects at Ambient and Elevated Temperatures," Proceeding of the 54th Electronic Components and Technology Conference, pp. 128-133, 2004.

81. Lin, J. K., De Silva, A., Frear, D., Guo, Y., Hayes, S., Jang, J. W., Li, L., Mitchell, D., Yeung, B., Zhang, C., "Characterization of Lead-Free Solders and Under Bump Metallurgies for Flip-Chip Packages," IEEE Transactions on Electronics Packaging Manufacturing, Vol. 25 (4), pp. 300-307, 2002.

82. Harrison, M. R., Vincent J. H., Steen, H. A. H., "Lead-free Reflow Soldering for Electronic Assembly," Soldering & Surface Mount Technology, Vol. 13 (3), pp.21-38, 2001.

83. Hwang, J., Environment-Friendly Electronics: Lead Free Technology, Electrochemical Publications, pp. 134-137, 2001.

84. Kanchanomai, C., Miyashita, Y., Mutoh, Y., "Low Cycle Fatigue Behavior of Sn-Ag, Sn-Ag-Cu and Sn-Ag-Cu-Bi Lead-free Solders," Journal of Electronic Materials, Vol. 31, pp. 456-465, 2002.

85. Zhu, F., Wang, Z., Guan, R., Zhang, H., "Mechanical Properties of Lead-Free Solder Alloys," 2005 International Conference on Asian Green Electronics, pp.107-112, 2005.

86. Rhee, H., Subramanian, K. N., Lee, A., Lee, J. G., "Mechanical Characterization of Sn-3.5Ag Solder Joints at Various Temperatures," Soldering and Surface Mount Technology, Vol. 15 (3), pp. 21-26, 2003.

87. Chromik, R. R., Vinci, R. P., Allen, S. L., Notis, M. R., "Measuring the Mechanical Properties of Pb-Free Solder and Sn-Based Intermetallics by Nanoindentation," JOM, Vol. 55 (6), pp. 66-69, 2003.

88. Xu, L., Pang, J. H. L., "Nanoindentation on SnAgCu Lead-free Solder and Analysis," Proceeding of the 55th Electronics Packaging Technology Conference, pp. 357-362, 2005.

89. McCabe, R. J., Fine, M. E., "A Thermal and Thermally Activated Plastic Flow in Low Melting Temperature Solders at Small Stresses," Scripta Materialia, Vol. 39(2), pp. 189-195, 1998.

90. McDowell, D. L., Miller, M. P., and. Brooks, D. C. "A unified creep-plasticity theory for solder alloys," in Fatigue of Electronic Materials, ASTM STP 1153, S. A. Schroeder and M. R. Mitchell, Eds. Philadelphia, PA: American Society for Testing and Materials, 1994, pp. 42–59.

91. Hertzberg, R. W., Deformation and Fracture Mechanics of Engineering Materials, John Wiley & Sons Inc, 4th edition, 1996.

92. Gilman, J. J., Micromechanics of Flow in Solids, McGraw-Hill, New York, 1969.

93. Cadek, J., Creep in Metallic Materials, Elsevier Science Publisher, 1988.

94. Hertzberg, R. W., Deformation and Fracture Mechanics of Engineering Materials, John Wiley & Sons Inc, 4th edition, 1996.

95. Ashby, M. F., "A First Report on Deformation-mechanism Maps," ActaMetallurgica, Vol. 20, pp. 887-897, 1972.

96. Evans, R. W., Wilshire, B., Creep of Metals and Alloys, The Institute of Metals,1985.

97. Kassner, M., and Perez-Prado, M. T., Fundamentals of Creep in Metals and Alloys Elsevier Science, 2004.

98. Cole, M. S., Caulfield, T., and Gonya, S. G. “Constant strain rate tensile properties of various lead based solder alloys at 0, 50, and 100 C,” in Proc. 4th Electron. Mater. Process. Congr., Montreal, QC, Canada, 1991, pp. 241–249.

99. Solomon, D. H., “The creep and strain rate sensitivity of a high Pb content solder with comparison to 60Sn/40Pb solder,” J. Electron. Mater., vol.19, no. 9, pp. 929–936, 1990.

100. Pang, H. L. J., Wang, Y. P., Shi, X. Q., and Wang, Z. P. “Sensitivity study of temperature and strain rate dependent properties on solder joint fatigue life,” in Proc. IEEE/CPMT Electronics Packaging Technology Conf., 1998, pp. 184–189.

101. Heiduschke, K. “Solder joint lifetime assessment of electronic devices,” Int. J. Numer. Meth. Eng., vol. 41, no. 2, pp. 211–231, 1998.

102. Knecht S., and L. Fox, “Integrated matrix creep: Application to Accelerated Testing and Lifetime Prediction, in Solder Joint Reliability: Theory and Applications”, J. H. Lau, Ed. New York: Van Nostrand Reinhold, Chapter 16, pp. 508–544, 1991.

103. Chauhan, P., Osterman, M., Lee, S.W.R., Pecht, M., “Critical Review of the Engelmaier Model for Solder Joint Creep Fatigue Reliability”, IEEE Transactions on Components and Packaging Technologies, Vol. 32, No. 3, 693-700 (2009)

104. Syed, A. "Accumulated Creep Strain and Energy Density Based Thermal Fatigue Life Prediction Models for SnAgCu Solder Joint" Proceedings Paper ECTC 2004, pp. 737- 746. ISBN 0-7803-8365-6

105. Engelmaier, W. "Pb-free solder creep-fatigue reliability models updated and extended". Global SMT and Packaging, Vol. 9, No.9. September, 2009. ISSN 1474-0893Marjamäki(2006)

106. Engelmaier, W. "Solder joint reliability prediction for chip components, MELFs, TSOPs, SOTs, ets", Global SMT and Packaging, Vol. 9. No.6, June 2009. ISSN 1474-0893

107. Gromala, P., Reichelt, J., Rzepka, S., “Accurate Thermal Cycle Lifetime Estimation for BGA Memory Components with Lead-free Solder Joints”, 10th. Int. Conf on Thermal, Mechanical and Multiphysics Simulation and Experiments in Micro-Electronics and Micro-Systems, EuroSimE 2009

108. Darveaux, R. “Solder joint fatigue life model_, Design and Reliability of Solders and Solder Interconnections”, The Minerals, Metals & Materials Society, (1997), pp. 213-218..

109. Popelar, S. F., Roesch M., Flip Chip Reliability Modelling Based on Solder Fatigue as Applied to Flip Chip on Laminate Assemblies, Paper presented on the IMAPS Workshop on Flip Chip, Braselton, Georgia, March 4-5,2000.

110. Lau, J.H, Tse, P., Richard, E., Dauksher, W., Shangguan, D and Pang, H.L “Reliability of Sn3wt%Ag0.5wt%Cu0.019%Ce(SACC) Solder Joints”, proceeding of the 59th Elec.Comf., May 26-29,2009, San Diego,California,pp415-422.

111. Gladwell, G. M. L., “Inverse vibration problems for finite-element models”, 1997 IOP Publishing Ltd.

112. Yang, C., Gao, S., “An Inverse Analysis to Estimate Thermal Conductivity Components of an Orthotropic Medium”, Third International Conference on Natural Computation (ICNC 2007)

113. Wang, J. and Zabaras, N., “A Bayesian inference approach to the inverse heat conduction problem”, International Journal of Heat and Mass Transfer, Vol.47, 2004, pp3927–3941

114. Wang, J. and Zabaras, N., “Hierarchical Bayesian models for inverse problems in heat conduction”, Inverse Problems, Vol.21, Issue 1, 2005, pp183-206

115. Massoni, E., Boyer, B., Forestier, R., “Inverse analysis of thermomechanical upsetting tests using gradient method with semi-analytical derivatives”, Int. J. Therm. Sci. 41 (2002) 557–563

116. Li, R., Fang, L., Deng, Y., Liu, S., “Multi-parameter Inverse Analysis Research Based on Comsol Multiphysics and Matlab”, 2010 International Conference On Computer Design And Appliations (ICCDA 2010)

117. Moulton, M.J., Creswell, L.L., Actis R.L., Myers, K.W., Vannier, M. W., Szabt, B.A., and Pasque, M., “ An Inverse Approach to Determining Myocardial Material Properties”, J. Biomechanics, Vol. 28, No. 8, pp. 935-948, 1995.

118. Kauer, M.,“Inverse Finite element Characterization of soft tissue with Aspiration experiments”, thesis submitted to Swiss Federal Institute of Technology

119. Kelley, C.T., *Iterative Methods for Optimization*. SIAM Press, Philadelphia, 1999.

120. Seshaiyer, P., Humphrey, J.D., “A Sub-Domain Inverse Finite Element Characterization of Hyperelastic Membranes Including Soft Tissues”, Journal of Biomechanical Engineering, June 2003, ASME, Vol. 125.

121. Seshaiyer, P., Hubner, J.P., Kumar, A.V., Ifju, P.G., “Load and Boundary Condition Calibration Using Full-field Strain Measurement”, Experimental Mechanics (2006) 46: 569–578.

122. Chenot, J., Massoni, E. and Fourment, L., “Inverse problems in finite element simulation of metal forming processes”, Engineering Computations, Vol. 13 No. 2/3/4, 1996, pp. 190-225.

123. Keanini, R. G. and Desai, N. N., “Inverse finite element reduced mesh method for predicting multi-dimensional phase change boundaries and nonlinear solid phase heat transfer”, Int.I. Hear Mass Transfer. Vol. 39, No. 5, pp. 1039-1049, 1996.

124. Husain, A., Sehgal, D.K., Pandey, R.K. “An inverse finite element procedure for the determination of constitutive tensile behavior of materials using miniature specimen”, Computational Materials Science 31 (2004) 84–92.

125. Onate, E., Rojek, J., Taylor, R. L. and Zienkiewicz, O. C., “Finite calculus formulation for incompressible solids using linear triangles and tetrahedra”. International Journal for Numerical Methods in Engineering. Vol.59. pp. 1473–1500. 2004.

126. Hinton, E., Rock, A. and Zienkiewicz, O., "A Note on Mass Lumping and Related Processes in the Finite Element Method". International Journal of Earthquake Engineering and Structural Dynamics. Vol. 4. pp. 245-249. 1976.

127. Zienkiewicz, O. C., The Finite Element Method. McGraw-Hill Company. London. 1977.

128. Chen, M.T., Ali, A. “An Efficient and Robust Integration Technique for Applied Random Vibration Analysis”. Computers and Structures. Vol. 66 No. 6. pp. 785–798. 1998.

129. Bathe, K. J., Finite Element Procedures. Prentice-Hall. Englewood Cliffs. 1996.

130. Cook, R. D., Concepts and Applications of Finite Element Analysis, Second Edition. John Wiley and Sons. New York. 1981.

131. Chen, M.T., Ali, A., “An Efficient and Robust Integration Technique for Applied Random Vibration Analysis”. Computers and Structures. Vol. 66 No. 6. pp. 785–798. 1998.

132. Imgrund, M. C., ANSYS® Verification Manual. Swanson Analysis Systems, Inc.. 1992.

133. Liu, X., “Experimental study and life prediction on high cycle vibration fatigue in BGA packages”, Microelectronics Reliability, 2006. 46(7): p. 1128-1138.

134. Bonet, J. and Wood, R.D., Nonlinear Continuum Mechanics for Finite Element Analysis. Cambridge University Press. 1997.

135. Mehner, J. and Senturia. S.D., “Computer-Aided Generation of Nonlinear Reduced-Order Dynamic Macromodels- II: Stress-Stiffened Case”. Journal of Microelectromechanical Systems,. S. 270–279. June 2000.

136. Antonova, E. E., Looman, D. C., “Finite elements for thermoelectric device analysis in ANSYS®”. ICT 2005 24th International Conference on Thermoelectrics. pp. 215-218. 2005.

137. Barry published in Soldering & Surface Mount Technology (2007) Vol 19 No. 2 pp 29 – 38. (2008)

138. Kim, I. and Lee. S., “Reliability and Failure Analysis of Lead-Free Solder Joints for PBGA Package Under a Cyclic Bending Load”, ieee transactions on components and packaging technologies, vol. 31, no. 2, june 2008

139. Herkommer D, Reid M, Punch J., "A comprehensive shear testing facility for joint-scale solder samples". In: Proceedings of EuroSimE. Freiburg; 2008. p. 635–42.

140. Bathias, C., "Piezoelectric fatigue testing machines and devices". International Journal of Fatigue 28 (2006) 1438–1445.

141. Saito, S., Kikuchi, K., Onishi, Y., Nishino, T., "Development of piezoelectric ceramics driven fatigue testing machine for small specimens", Journal of Nuclear Materials 307–311 (2002) 1609–1612.

142. Tee, T.Y., Ng, H.S., Yap, D., and Zhong, Z.W., “Board Level Solder Joint Reliability Modeling and Testing of Fine-pitch CSP Packages for Telecommunication Applications,” SEMICON Advanced Packaging Technology Symposium, Singapore, 2003, pp. 31-36.

143. Ridout., S., “Modelling and experiment on an isothermal fatigue test for solder joints”, EUROSIME Pages 478-482, EEE, 2005

144. ANSYS® Mechanical APDL 12.0.1, ANSYS® Inc. 2009

145. ANSI/IEEE Standard on Piezoelectricity IEEE Standard. pp. 176. 1987.

146. Reinikainen, T.O., Marjamäki, P., and Kivilahti, J.K., "Deformation Characteristics and Microstructural Evolution of SnAgCu Solder Joints," EuroSime Conference Proc., Germany, Apr. 2005

147. Darveaux, R., "Effect of Simulation Methodology on Solder Joint Crack Growth Correlation," 50th ECTC Conference Proc., 2000, pp. 1048-1058.

148. Ghaffarian, R. , Kim, N.P. ,"Reliability and Failure Analyses of Thermally Cycled Ball Grid Array Assemblies", IEEE Transactions on Components and Packaging Technologies, Vol. 23, No. 3, pp. 528-534,September 2000.

149. Schubert, A., Dudek, R., Auerswald, E., Gollhardt, A., Michel, B., and Reichl, H., "Fatigue Life Models of SnAgCu and SnPb Solder Joints Evaluated by Experiments and Simulations," 53rd ECTC 2003, pp. 197-206.

150. Motalab, M., Cai, Z., Suhling, J. C., Zhang, J., Evans, J. L., Bozack, M. J., and Lall, P., "Improved Predictions of Lead Free Solder Joint Reliability That Include Aging Effects," Proceedings of 62nd Electronic Components and Technology Conference, San Diego, CA, 2012.

151. Ridout, S., Dusek, M., Bailey, C., Hunt, C., "Modeling and experiments on an isothermal fatigue test for solder joints", EuroSimE 2005 Proceedings of the 6th International Conference on Thermal Mechanial and MultiPhysics Simulation and Experiments in MicroElectronics and MicroSystems 2005 (2005)

152. Ridout, S. Dusek, M., Bailey, C., "Modelling to predict the reliability of solder joints ", 1st Electronic System integration Technology Conference (2007) Volume: 2, Issue: 12, Publisher: IEEE, Pages: 927-933

153. Tu, P. L., Hung, K. C., and Lai, J. K. L. (2000), "Comparative study of micro-BGA reliability under bending stress", IEEE Transactions and Advanced packing, Vol 23 No 4, pp. 750-756

154. Nurmi, S., Sundelin, J., Ristilainen, E., E., Lepisto, T. (2004), “The effect of solder paste composition on the reliability of SnAgCu joints”, Elsevier: Microelectronics Reliability, Vol 44 Issue 3, pp. 484 – 494.

155. Syed, A., Kim, S. M., Lin, W., Khim, J. Y., Song, E. S., Shin, J. H., Panczak, T., “A Methodology for Drop Performance Prediction and Application for Design Optimization of Chip Scale Packages”, Proceedings of the 55th Electronic Components and Technology Conference, pp. 472-479, 2005.

156. Lai, J.K.L., K.C. Hung, Y.C. Chan, and P.L. Tu. “Comparative study of micro-BGA reliability under bending stress.” IEEE Transactions on Advanced Packaging 23, no. 4 (2000): pp750-756.

157. Yunus, M, K Srihari, J Pitarresi, and a Primavera. “Effect of voids on the reliability of BGA/CSP solder joints.” Microelectronics Reliability 43, no. 12 (December 2003): pp2077-2086.

158. Sundelin, J.J., Nurmib, S.T., Lepist, T.K., “Recrystallization Behaviour of SnAgCu Solder Joints,” Materials Science and Engineering A, Vol. 474, No. 1-2, 201–207 (2008)

159. Zhou, Y., Al-Bassyiouni, M., Dasgupta, A., “Vibration Durability Assessment of Sn3.0Ag0.5Cu and Sn37Pb Solders Under Harmonic Excitation,” Journal of Electronic Packaging, Vol. 131, No. 1, (2009)

160. Wiese, S., Meusel, E., and Wolter, K., “Microstructural Dependence of Constitutive Properties of Eutectic SnAg and SnAgCu Solders,” 53rd ECTC 2003, pp. 197-206.

161. Pang, H. L. J., Tan, K. H., Shi, X. Q., and Wang, Z. P., “Thermal cycling aging effects on microstructural and mechanical properties of a single PBGA solder joint specimen,” IEEE Trans. Compon. Packag. Technol., vol. 24, no. 1, pp. 10–15, Mar. 2001.

162. Morris, J.W., Song, H.G., and Hua, F., “Creep Properties of Sn-rich Solder Joints,” Proceedings 2003 ECTC, s02p3C, pp. 54-57.

163. Pang, J.H.L., Xiong, B.S., Neo, C.C., Zang, X.R., and Low, T.H., “Bulk Solder and Solder Joint Properties for Lead Free 95.5Sn-3.8Ag-0.7Cu Solder Alloy,” 2003 ECTC, s16p4C, pp. 673-679.

164. Darveaux, R.., “Mechanical Testing of Solder Joint Arrays versus Bulk Solder Specimens,” Proc. SMTAI, 2006.

165. Marks, R.A., Pan, D., Dutta, I., and Jadhav, S.G., “Impression Creep Testing and Constitutive Modeling of Sn-based Solder Interconnects,” Proceedings 2004 ITHERM, pp.95-102.

166. Frear, D.R., Thermomechanical Fatigue of of Solder Joints: A New Comprehensive Test Method. IEEE

167. Borgesen, P. and Henderson, D.W., White Paper: "Fragility of Pb-Free Solder Joints". 2004, Universal Instruments Corporation: Binghampton, NY.

168. Tanaka, M. and Bui, H.D., Inverse Problems in Engineering Mechanics, Springer-Verlag Press, U.K., 1992.

169. W.H. Press. Numerical Recipes in C: The Art of Scienfitic Computing. Cambridge University Press. 1993.

170. Brown, S.B., Kim, K.H., Anand, L., “An internal variable constitutive model for hot working of metals”, International Journal of Plasticity, pp. 95–130, 1989

171. Wu, R.., Mccluskey, F.P., “In Constitutive relations of indium solder joint in cold temperature electronic packaging based on Anand model”, 11th Intersociety Conference on Thermal and Thermomechanical Phenomena in Electronic Systems, Florida, USA, May, pp. 683–686 (2008)

172. Wang, G.Z., Cheng, Z.N., Becker, K., Wilde, J., “Applying Anand Model to Represent the Viscoplastic Deformation Behavior of Solder Alloys”, Journal of Electronic Packaging, September 2001, Vol. 123

173. Bai, N., Chen X., Gao H., “Simulation of uniaxial tensile properties for lead-free solders with modified Anand model”, Materials and Design 30 (2009) 122–128

174. Liang Zhang, Songbai Xue, Lili Gao, Guang Zeng, Zhong Sheng, Yan Chen and Shenglin Yu, Determination of Anand parameters for SnAgCuCe solder, Modelling Simul. Mater. Sci. Eng. 17

175. X. Chen, G. Chen, M. Sakane, “Modified Anand Constitutive Model for Lead-Free Solder Sn-3.5Ag,“ Proceedings 2004 ITHERM, pp.447-452.

176. Xu Chen, Gang Chen and Masao Sakane “Prediction of Stress-Strain relationship with an improved Anand constitutive model for lead-free solder Sn-3.5Ag”, IEEE Transactions on components and packaging technologies, vol. 28, No.1, March 2005

177. Qiang, W., Lihua, L., Xuefan, L., Xiaohong, W., Liu, Y., Irving, S. and Luk, T., “Experimental Determination and Modification of Anand Model Constants for Pb-Free Material 95.5Sn4.OAgO.5Cu”, Thermal, Mechanical and Multi-Physics Simulation Experiments in Microelectronics and Micro-Systems, 2007. EuroSime 2007

178. Chang, J., Wang, L., Dirk, J., Xie, X., “Finite Element Modeling Predicts the Effects of Voids on Therma lShock Reliability and Thermal Resistance of Power Device“, Welding Journal, March 2006, pp. 63-70

179. Bai, N., Chen, X., Gao, H., “Simulation of uniaxial tensile properties for lead-free solder with modified Anand model”, Materials and Design 30 (2009) 122-128.

180. Wang, Q., Zhang,Y., Liang, L., Liu, Y., Irving, S., “Anand Parameter Test for Pb-Free Material SnAgCu and Life Prediction for a CSP”, Electronic Packaging Technology, 2007. ICEPT 2007. 8th International Conference.

181. Mysore, K., Subbarayan, G., Gupta, V., Zhang, R., “Constitutive and Aging Behavior of Sn3.0Ag0.5Cu Solder Alloy”, IEEE Transactions on Electronics Packaging Manufacturing, v32, n4, p221-232, Oct.2009.

182. Bhate, D., Chan, D., Subbarayan, G., Chiu, T.C., Gupta, V., Edwards, D., “Constitutive behavior of Sn3.8Ag0.7Cu and Sn1.0Ag0.5Cu alloys at creep and low strain rate regimes”, IEEE Transactions on Components and Packaging Technologies, v31 ,n3, p622-633, 2008.

183. Chen, X., Chen, G., Sakane, M., “Modified Anand Constitutive Model for Lead-free Solder Sn-3.5Ag”, 2004 inter Society Conference on Thermal Phenomena.

184. Wilde, J., Becker, K., Thoben, M., Blum, W., Jupitz, T., Wang, G. and Cheng, Z. N., “Rate dependent constitutive relations based on Anand model for 92.5Pb5Sn2.5Ag solder,” IEEE Transactions on Advanced Packaging, vol. 23, n. 3, pp. 408-414, 2000.

185. Wang, G. Z., Cheng, Z. N., Becker, K. and Wilde, J., “Applying Anand model to represent the viscoplastic deformation behavior of solder alloys,” Journal of Electronic Packaging, Transactions of the ASME, vol. 123, n3, 2001, pp. 247-253.

186. Paquet M., Gaynes M., Duchesne E., Questad D., Bélanger L., Sylvestre J., “Underfill selection strategy for Pb-free, low-k and fine pitch organic flip chip applications,” Proceedings of 56th electronic components and technology conference, 2006. p. 1595–603.

187. Rodgers, B., Flood, B., Punch, J.,“Experimental Determination and Finite Element Model Validation of the Anand Viscoplasticity Model Constants for SnAgCu,” The 6th IEEE EuroSimE Conference, Berlin, 2005.

188. Lau, J. H., Lee, S. W., “Modeling and Analysis of 96.5Sn-3.5Ag Lead-Free Solder Joints of Wafer Level Chip Scale Package on Buildup Microvia Printed Circuit Board,” IEEE Trans. on Electronics Packaging Manufacturing, Vol. 25, No. 1 (2002), pp. 51-58.

189. Rodgers, B., "Experimental Determination and Finite Element Model Validation of the Anand Viscoplasticity Model Constants for SnAgCu", EuroSimE 2005, Berlin, Germany, April. 2005, pp.490-496.

# Appendix A  Smoothing Techniques

Recently a smoothing technique based on Fourier analysis of filtering was presented [164]. This technique was designed to smooth cooling curve, temperature rates and heat transfer coefficients.

The mathematical basis of this procedure is described briefly below. If we assumed a finite set of noisy data which is obtained through experiment or computation to be made up of data pairs of real numbers $(t_i, y_i)$ for i=0,1,2…….,2N, where 2N is the total number of data pairs. These data pairs are discrete values of a continuous noisy function $Y_A = Y_A(t)$ which is defined in the interval $(t_s, t_f)$ and for which $y_i = Y_A(t_i)$ is fulfilled for

$$\begin{gathered} t_i = t_0 + i\frac{t_f - t_s}{2N} \text{ where } i = 0,1,2..........2N \\ t_0 = t_s,\ y_0 = y_i \text{ and } t_{2N} = t_f,\ y_{2N} = y_f \end{gathered} \quad \textbf{(0-1)}$$

A periodic function $Y_P(t)$ is constructed from $Y_A(t)$ as shown below;

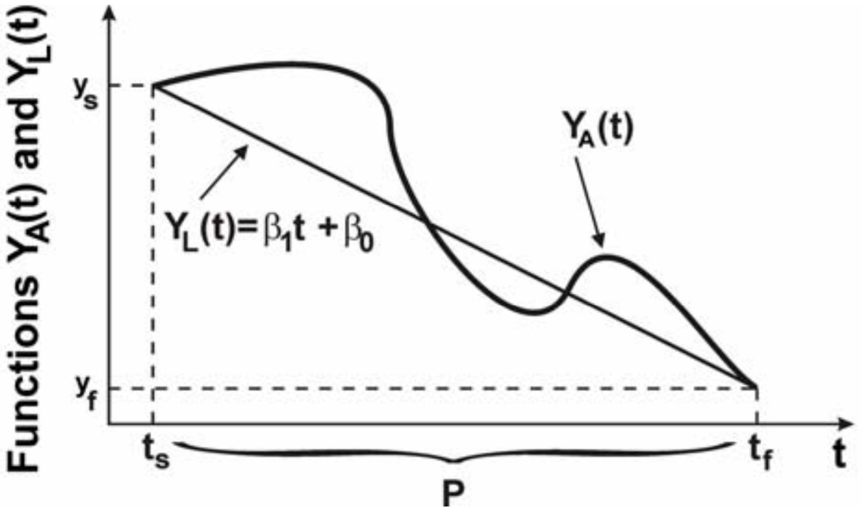

**Figure A-0-1   Fourier's technique for curve smoothing**

**Principle of smoothing based on the Fourier analysis**

$$Y_P(t) = Y_A(t) - Y_L(t)$$

*where*

$$Y_L(t) = \beta_1(t) + \beta_0$$

$$\beta_1 = \frac{y_f - y_s}{t_f - t_s} = \frac{y_{2N} - y_0}{t_{2N} - t_0}$$

$$\beta_0 = y_s - \beta_1 t_s = y_0 - \beta_1 t_0$$

Sarmiento et al [173] demonstrated that $Y_A(t)$ can be approximated by a truncated Fourier series:

$$Y_{F,M}(t) = Y_M(t) + Y_L(t)$$

$$Y_{F,M}(t) = \beta_0 + \beta_1(t) + \frac{a_0}{2} + \sum_{k=1}^{M}\left[a_k \cos\left(\frac{2\pi k}{P}t\right) + b_k \sin\left(\frac{2\pi k}{P}t\right)\right]$$

*where*

$$a_k = \frac{1}{N}\sum_{k=1}^{2N-1} Y_i \cos\left(\frac{k\pi}{N}i\right)$$

$$b_k = \frac{1}{N}\sum_{k=1}^{2N-1} Y_i \sin\left(\frac{k\pi}{N}i\right)$$

$$Y_i = y_i - (\beta_0 + \beta_1 t_i)$$

For i= 0,1,2,…….2N, k=0, 1, 2,………..M and $t_s \le t_i \le t_f$

The function $Y_{F,M}(t)$ can be used to calculate the smooth values of $y_i$ and $t_i$ on the whole interval $t_s \le t_i \le t_f$

This above procedure was used to smooth the experimental datasets from NPL. A comparative was thus performed to determine whether it outperformed the traditional methods such as moving average, Savitzy-Golay and filtering. Although this method shows a lot of promise, the traditional methods performed better than the above method. The analysis performed in chapter (6) therefore only makes use of the traditional method.

# Appendix B Theoretical Data modelling using Least square method

To perform data modelling using the least square method, the general Garofalo's creep equation is used to demonstrate the concept. Starting with a model by defining X$_i$ as the independent variables, Y$_i$ is dependent variables vector of measured values, P$_k$ is the parameter array, the model is defined as Y$_i$=Y(X$_i$, Pk). Using the Garofalo's creep equation with four material parameters;

$$\dot{\varepsilon}\left(\sigma,T,\vec{C}\right)=C_1\sinh^{C_2}\left(C_3\sigma\right)\exp\left(-\frac{C_4}{RT}\right)$$

$$\vec{C}=\left(C1,C2,C3,C4\right)^T$$

$$\lambda\left(\vec{C}\right)=\sum_i\left[\dot{\varepsilon}\left(\sigma_i,T_i,\vec{C}\right)-\dot{\varepsilon}_i\right]^2$$

$$\frac{\partial\lambda}{\partial C_k}=0,\quad k=1,4$$

$$2\sum_i\frac{\partial\dot{\varepsilon}\left(\sigma_i,T_i,\vec{C}\right)}{\partial C_j}\left[\dot{\varepsilon}\left(\sigma_i,T_i,\vec{C}\right)-\dot{\varepsilon}_i\right]\quad=0,\quad j=1,4$$

This has to be solved numerically. Iterative method can be used $\vec{C}^{k+1}=\vec{C}^k+\Delta\vec{C}^k$

The equation can be linearised by using the Taylor's expansion at $C=C_k$.

$$\dot{\varepsilon}\left(\sigma_i,T_i,\vec{C}\right)=\dot{\varepsilon}\left(\sigma_i,T_i,\vec{C}^k\right)+\sum_j\frac{\partial\dot{\varepsilon}\left(\sigma_i,T_i,\vec{C}\right)}{\partial C_j}\left(C_j-C_j^k\right)$$

$$J_{ij}=\frac{\partial\dot{\varepsilon}\left(\sigma_i,T_i,\vec{C}\right)}{\partial C_j}$$

$$\Lambda C_j=C_j-C_j^k$$

*Therefore*

$$\dot{\varepsilon}\left(\sigma_i,T_i,\vec{C}\right)=\dot{\varepsilon}\left(\sigma_i,T_i,\vec{C}^k\right)+\sum_j J_{ij}\Lambda C_j$$

From above and substituting

$$2\sum_i \frac{\partial \dot{\varepsilon}\left(\sigma_i,T_i,\vec{C}\right)}{\partial C_j}\left[\dot{\varepsilon}\left(\sigma_i,T_i,\vec{C}\right)-\dot{\varepsilon}_i\right]=2\sum_i J_{ij}\left[\sum_l J_{il}\Lambda C_l+\dot{\varepsilon}\left(\sigma_i,T_i,\vec{C}^k\right)-\dot{\varepsilon}_i\right]=0$$

$$\textit{substituting } \Lambda\dot{\varepsilon}\left(\sigma_i,T_i,\vec{C}^k\right)=\dot{\varepsilon}\left(\sigma_i,T_i,\vec{C}^k\right)-\dot{\varepsilon}_i$$

$$\sum_i\sum_l\left[J_{ij}J_{il}\Lambda C_l-J_{ij}\Lambda\dot{\varepsilon}\left(\sigma_i,T_i,\vec{C}^k\right)\right]=0 \qquad j=1,......4$$

$$\sum_i\sum_l J_{ij}J_{il}\Lambda C_l=\sum_i J_{ij}\Lambda\dot{\varepsilon}\left(\sigma_i,T_i,\vec{C}^k\right) \qquad j=1,......4$$

These set of linear equations of C are solved to find $C^{k+1}$.

For M experimental measurement at a given stress and temperature the error in the measurements are given by

$$\lambda(\vec{C})=\sum_{n=1}^{m}\sum_i\left[\dot{\varepsilon}\left(\sigma_i,T_i,\vec{C}\right)-\dot{\varepsilon}_{im}\right]^2$$

$$2\sum_m\sum_i\frac{\partial\dot{\varepsilon}\left(\sigma_i,T_i,\vec{C}\right)}{\partial C_j}\left[\dot{\varepsilon}\left(\sigma_i,T_i,\vec{C}\right)-\dot{\varepsilon}_i\right]=0 \qquad j=1,......4$$

$$2M\sum_i\frac{\partial\dot{\varepsilon}\left(\sigma_i,T_i,\vec{C}\right)}{\partial C_j}\left[\dot{\varepsilon}\left(\sigma_i,T_i,\vec{C}\right)-\frac{1}{M}\sum_m\dot{\varepsilon}_{im}\right]=0 \qquad j=1,........4$$

The experimental result is given in the form of a force-displacement curve. In inverse modelling the force is can be expressed in the form:

$$\mathrm{F}=\mathrm{F}(\vec{\mathrm{C}},\mathrm{E},\nu,\mathrm{T},\mathrm{t},\mathrm{U})$$

where F is the force,

C creep material constant
T is the temperature
t is the time
ν is the Poisson’s ratio
U is the displacements

It is assumed that all the other material properties are known, then

$$\mathrm{F}=\mathrm{F}(\vec{\mathrm{C}})$$

The inverse problem then becomes an optimisation problem with the minimisation of the norm of the residual given by

$$\lambda(\vec{\mathrm{C}})=\sum_{\mathrm{i}}[\mathrm{F_i}(\vec{\mathrm{C}}])-\mathrm{P_i}]$$

# Appendix C  Parameters for Anand’s Model in Literature

The table below highlight’s the wide scatter of available material properties for the Anand’s constitutive model.

Table C.1 Parameters of Anand's constitutive model

| | S0(MPa) | Q/R(K) | A(S-1) | ξ | m | h0(MPa) | $\hat{S}$(MPa) | n | α |
|---|---|---|---|---|---|---|---|---|---|
| SAC405[17] | 21.57 | 10561 | 325 | 10 | 0.328 | 8.0E5 | 42.1 | 0.02 | 2.57 |
| SAC305[18] | 45.9 | 7460 | 5.87E6 | 2 | 0.0942 | 9350 | 58.3 | 0.015 | 1.5 |
| SAC305[19] | 2.45 | 6069 | 717.26 | 2 | 0.13 | 1.46E10 | 2.9E7 | 0.0436 | 2.22 |
| Sn3.5Ag[19] | 0.65 | 6542 | 344.716 | 3 | 0.143 | 23241 | 26 | 0.0447 | 1.46 |
| Sn0.7Cu[19] | 4.43 | 5840 | 764.166 | 2 | 0.123 | 11656 | 26.4 | 0.043 | 2.33 |
| SAC385[182] | 16.31 | 13982 | 49601 | 13 | 0.36 | 8.0E5 | 34.71 | 0.02 | 2.18 |
| SAC305[183] | 2.15 | 9970 | 17.994 | 0.35 | 0.153 | 1525.98 | 2.536 | 0.028 | 1.69 |
| SAC105[184] | 2.3479 | 8076 | 3.773 | 0.9951 | 0.4454 | 4507.5 | 3.5833 | 0.012 | 2.1669 |
| SAC387[184] | 3.2292 | 9883 | 15.773 | 1.0673 | 0.3686 | 1076.9 | 3.1505 | 0.0352 | 1.6832 |
| SAC405[185] | 1.3 | 9000 | 500 | 1.5 | 0.303 | 1379 | | 0.07 | 1.3 |
| Sn3.5Ag[185] | 52.4 | 85459 | 177016 | 7 | 0.207 | 27782 | 52.4 | 0.0177 | 1.6 |
| Sn3.5Ag[186] | 7.17 | 29800 | 0.0034 | 2.48 | 0.03 | 2080 | 5.8 | 0.0068 | 1.41 |
| SAC387[186] | 21.57 | 1.0041E4 | 9.45E3 | 1.1452 | 0.1158 | 133.8025 | 13.337 | 0.0402 | 0.1082 |
| Sn3.5Ag[187] | 7.72 | 1.41E4 | 1.63E6 | 1.61 | 0.13 | 5.87E4 | 11.99 | 0.017 | 2.09 |
| SAC405[188] | 1.3 | 9000 | 500 | 7.1 | 0.3 | 5900 | 39.4 | 0.03 | 1.4 |
| SAC387[189] | 24.04 | 11049 | 8.75E6 | 4.12 | 0.23 | 9537 | 90.37 | 2.26E-10 | 1.2965 |
| Sn3.5Ag[189] | 39.09 | 8900 | 2.23E4 | 6 | 0.182 | 3321.15 | 173.81 | 0.018 | 1.82 |
| | | 12480 | 4223 | | 0.34 | 2.98E5 | | 0.03 | 1.98 |